Appendix to the Dissertation:

Influence of Selected Drug Molecules on Human Tear Film Lipid Layer Models

Kamila Riedlová

August 2024

Contents

1 Publication I: Latanoprost incorporates in the tear film lipid layer: An experimental and computational model study 3

2 Supporting information of Publication I 12

3 Publication II: Influence of BAKS on tear film lipid layer: In vitro and in silico models 17

4 Supporting information of Publication II 27

5 Publication III: The potential role of SP-G as surface tension regulator in tear film: From molecular simulations to experimental observations 31

6 Publication IV: H1 helix of colicin U causes phospholipid membrane permeation 48

7 Supporting information of Publication IV 59

1 Publication I: Latanoprost incorporates in the tear film lipid layer: An experimental and computational model study

International Journal of Pharmaceutics 645 (2023) 123367

Contents lists available at ScienceDirect

International Journal of Pharmaceutics

journal homepage: www.elsevier.com/locate/ijpharm

Latanoprost incorporates in the tear film lipid layer: An experimental and computational model study

Kamila Riedlová [a,b], Maria Chiara Saija [a,b], Agnieszka Olżyńska [a,*], Katarina Vazdar [a], Philippe Daull [c], Jean-Sebastien Garrigue [c], Lukasz Cwiklik [a,*]

[a] J. Heyrovský Institute of Physical Chemistry, Czech Academy of Sciences, Dolejškova 3, 18223 Prague, Czech Republic
[b] Department of Physical and Macromolecular Chemistry, Faculty of Science, Charles University, Hlavova 8, 12800 Prague, Czech Republic
[c] SANTEN SAS, Novagali Innovation Center, 1 rue Pierre Fontaine, Bâtiment Genavenir IV, CEDEX F-91458 Evry, France

ARTICLE INFO

Keywords:
Tear film
Latanoprost
Glaucoma
Tear film lipid layer
Topical delivery
Ophthalmology

ABSTRACT

Glaucoma is a leading cause of blindness worldwide, with elevated intraocular pressure being a major risk factor for its development and progression. First-line treatment for glaucoma relies on the administration of prostaglandin analogs, with latanoprost being the most widely used. However, before latanoprost reaches the cornea, it must pass through the tear film and tear film lipid layer (TFLL) on the ocular surface. Given the significant lipophilicity of latanoprost, we hypothesize that TFLL could, to a certain extent, act as a reservoir for latanoprost, releasing it on longer time scales, apart from the fraction being directly delivered to the cornea in a post-instillation mechanism. We investigated this possibility by studying latanoprost behavior in acellular in vitro TFLL models. Furthermore, we employed in silico molecular dynamics simulations to rationalize the experimental results and obtain molecular-level insight into the latanoprost-TFLL interactions. Our experiments demonstrated that latanoprost indeed accumulates in the TFLL models, and our simulations explain the basis of the accumulation mechanism. These results support the hypothesis that TFLL can serve as a reservoir for latanoprost, facilitating its prolonged release. This finding could have significant implications for optimizing glaucoma treatment, especially in the development of new drug delivery systems targeting the TFLL.

1. Introduction

Glaucoma is a slowly progressive eye disorder that leads to damage of the optic nerve and distinctive changes in the field of vision followed by the eventual onset of blindness (Digiuni et al., 2012; Lee and Higginbotham, 2005; Weinreb et al., 2014). Today, glaucoma is the third leading cause of blindness in the population, with more than 76 million people worldwide suffering from the illness. This number is predicted to increase further, coming to more than 112 million patients in 2040 (Quigley and Broman, 2006; Tham et al., 2014). The costs of treatment of glaucoma in the US in 2016 were estimated to be $2.5 billion per year, with an increased expectancy in the future (Lazcano-Gomez et al., 2016; Traverso et al., 2005; Varma et al., 2011). Even though the causes of glaucoma are still unknown, one of the major risks for its development and progression can be found in the elevated intraocular pressure (IOP) (Jonas et al., 2017; Sommer, 1989). The IOP is also the only known risk factor for glaucoma that can be influenced by medical treatment and all methods for glaucoma treatment heavily rely on the reduction of IOP (Jonas et al., 2017).

In the course of the development of glaucoma treatment, several different families of compounds have been introduced, for instance, beta-blockers, carbonic anhydrase inhibitors, and alpha-adrenergic agonists, but the first-line treatment today depends on the administration of prostaglandin analogs (Taylor, 2019; Thiruchelvi and Shivanika, 2021; Wu et al., 2021). Latanoprost (see Fig. S1) was the first prostaglandin analog drug for the treatment of glaucoma and still remains the most prominent and widely used due to minimal side effects, low concentration efficiency, and good tolerability (European Glaucoma Society, 2017; Alm, 2014; Hedman and Larsson, 2002). Latanoprost is mostly administered to glaucoma patients topically, in the form of eye drops administered on a daily basis (Diestelhorst et al., 1997; Patel and Spencer, 1996). Due to its lipophilic nature, it is presumed to easily penetrate into the cornea where it hydrolyzes to the corresponding latanoprost acid, the active compound in the anterior parts of the eye (Basu et al., 1994; Sjöquist and Stjernschantz, 2002). However, before latanoprost reaches the cornea, it has to pass through the tear film lipid

* Corresponding authors.
E-mail addresses: agnieszka.olzynska@jh-inst.cas.cz (A. Olżyńska), lukasz.cwiklik@jh-inst.cas.cz (L. Cwiklik).

https://doi.org/10.1016/j.ijpharm.2023.123367
Received 17 May 2023; Received in revised form 29 August 2023; Accepted 1 September 2023
Available online 4 September 2023
0378-5173/© 2023 Elsevier B.V. All rights reserved.

layer (TFLL) on the ocular surface into the aqueous layer covering the cornea (Cwiklik, 2016).

The TFLL comprises a polar and a nonpolar lipid layer, with the nonpolar layer being predominant. As a result, during administration, lipophilic latanoprost molecules come into contact predominantly with the nonpolar lipid component of the TFLL. Given the high lipophilicity of latanoprost, we anticipate that the TFLL will temporarily accumulate latanoprost knowing that the half-life of the TFLL is around 8–9 h, whereas the half-life of the aqueous phase is on the order of minutes (Mochizuki et al., 2009). Evidence supporting this hypothesis can be found in the observation that latanoprost concentrations peak in the iris is one hour after treatment (Bito and Baroody, 1987), in comparison to significantly shorter times for other IOP reducing drugs (Fayyaz et al., 2021).

In this study, we investigate the potential for latanoprost to accumulate in the TFLL by examining its behavior in TFLL model systems through experimental Langmuir trough techniques and validating the findings using molecular dynamics simulations. Our experiments demonstrate that latanoprost indeed accumulates in the TFLL models, and we further analyze the accumulation mechanism using molecular simulations. The findings presented in this paper strongly support the notion that the TFLL can act, to a certain degree, as a latanoprost reservoir, gradually releasing it over extended periods, thereby offering an alternative delivery pathway instead of the immediate delivery to the cornea after instillation.

2. Methodology

2.1. Materials

Behenyl oleate (BO) and cholesteryl erucate (CE), assigned as nonpolar lipids, were purchased from Larodan (Solna, Sweden). 1-Palmitoyl-2-oleyl-*sn*-glycero-3-phosphocholine (POPC), assigned as polar lipid (PL), was ordered from Avanti Polar Lipids (Alabaster, AL). Latanoprost (LTP) and EDTA were supplied by Sigma-Aldrich (St. Louis, MO). Chloroform of spectroscopic grade for the preparation of working solutions was ordered from Merck (Darmstadt, Germany). PBS (Merck, Darmstadt, Germany) buffer was prepared with Milli-Q water (Millipore, USA).

2.2. Langmuir trough experiments - isotherms

Langmuir film isotherms were measured using MicroTroughXS setup (Kibron, Helsinki, Finland) equipped with a stainless-steel trough with PTFE edges and a surface pressure sensor with the DyneProbe. The PL monolayer was deposited from a chloroform solution (1 mM) with a Hamilton syringe over a PBS (containing 0.2 mM EDTA) subphase at completely opened barriers to obtain low material packing at the interface (0 mN/m). After chloroform evaporation and formation of a lipid film (~8 min), the compression-relaxation cycle (at ~0.05 (nm^2/chain)/min) was run by the symmetrical movement of two barriers up to the surface pressure of 35 mN/m. Later, LTP in chloroform was added to the system with a Hamilton syringe from atop the PL monolayer. After 5 min, when chloroform evaporated and the film equilibrated, the compression-relaxation cycle was run again. Finally, the experiment was finished with surface pressure-surface area isotherm measured up to the film collapse. The measurements were performed at 307.5 K, corresponding to the temperature of the human cornea (Efron et al., 1989). The system's temperature was controlled by the metal plate with circulating water from the attached thermostat placed below the trough. Area per polar lipid (APPL) was used to quantify the lipid packing at the interface. It was defined as a ratio of the number of PL molecules to the surface area spanned by the film. APPL allows a direct comparison of interfacial lipid packing in pure PL and PL-LTP films (Wizert et al., 2014).

2.3. Langmuir trough experiments - kinetics

The kinetics of LTP interaction with the TFLL model was studied using a MicroTroughXS setup (Kibron, Helsinki, Finland) equipped with a small-volume multi-trough. A single well was filled with 300 μl of subphase (PBS containing 0.2 mM EDTA) and on top of it lipids in chloroform solution were deposited with a Hamilton syringe. After reaching the desired surface pressure value, chloroform was allowed to evaporate, and TFLL film was formed and equilibrated (15–20 min). Later, LTP in chloroform was added to the system with a Hamilton syringe from above the interface. Up to 9 additions of LTP, every ~10 min, were introduced to get the maximum 9 to 1 molar ratio of LTP to PL in the TFLL model. All kinetics measurements were performed at 298 K.

2.4. MD simulations - LTP in bulk water and in TFLL

In simulations involving LTP in bulk water fifty drug molecules were placed randomly in a box of 5000 water beads using Packmol v. 20.11.0 (Martínez et al., 2009). The system was energy minimized and equilibrated for ~80 ps using an isotropic coupling pressure with Berendsen barostat at 400 K (Berendsen et al., 1984). In this process, the volume of the simulation box was reduced until converging to $\sim 9 \times 9 \times 9$ nm^3. After equilibration, the production run was carried out for 1 μs using the same parameters as for equilibration, but the temperature was reduced to 310 K. Then, the formed LTP aggregate was simulated at the water–air interface (referred to as $LTP_{water\text{-}air}$). To create a water–air interface, the simulation box was elongated along one coordinate thus forming a vacuum region above the water box. The final size of the box was $\sim 9 \times 9 \times 15$ nm^3. This new system was energy minimized and equilibrated for ~100 ps. The production run was carried out for 1 μs at 310 K. In the simulations of LTP with the TFLL model, we constructed the system based on a pre-equilibrated TFLL model obtained in our previous study (Riedlová et al., 2023). It consisted of a water slab, a polar POPC monolayer placed on top of the water, and a thick layer of nonpolar lipids formed by an equimolar mixture of behenyl oleate (BO) and cholesteryl erucate (CE) placed on top of the monolayer, with a vacuum layer of ~20 nm left on top of the nonpolar lipids. The system was symmetric along the elongated coordinate; hence two interfaces covered by two replicas of TFLL were present. For presentation purposes, in the following, we present and discuss the data for this one of the two interfaces which interacted with LTP. The behavior of the second interface had no influence on the results. Further details on the TFLL lipid composition and structure can be found in our previous work (Wizert et al., 2017). The packing of polar lipids at the interface was constant and set so that the area per PL lipid APPL = 0.67 nm^2, corresponding to a high packing of the monolayer (greater than 30 mN/m, Langmuir isotherm, Fig. 1A). Such a configuration of the TFLL model was already tested several times for analogous studies (Eftimov et al., 2020; Wizert et al., 2017). Additionally, we performed control simulations of LTP in TFLL with aggregated LTP located initially in the vacuum phase. Furthermore, we tested a system with 20% fewer PL molecules (referred to as $LTP_{TFLL20water}$ and $LTP_{TFLL20air}$, respectively) to elevate the enhanced lateral pressure caused by the adsorption of LTP.

The MD simulations performed in this study were done using the GROMACS software package (version 2020.4) (Van Der Spoel et al., 2005), and the systems were modeled applying the MARTINI coarse grain force field (MARTINI v.2.2) (Marrink et al., 2007). The force field parameters for the molecule of LTP were developed in-house according to the MARTINI approach and are listed in the Supporting Information. The equations of motion were resolved with the time step of 10 fs. The production runs were conducted in the NVT statistical ensemble (except for the simulation in bulk water, in which the NPT ensemble was employed), thus keeping the volume of the box fixed. The Verlet algorithm was used for the cut-off scheme (Grubmüller et al., 1991). Periodic boundary conditions were applied along the three directions. The Coulomb and the Van der Waals interactions were truncated at 1.1 nm

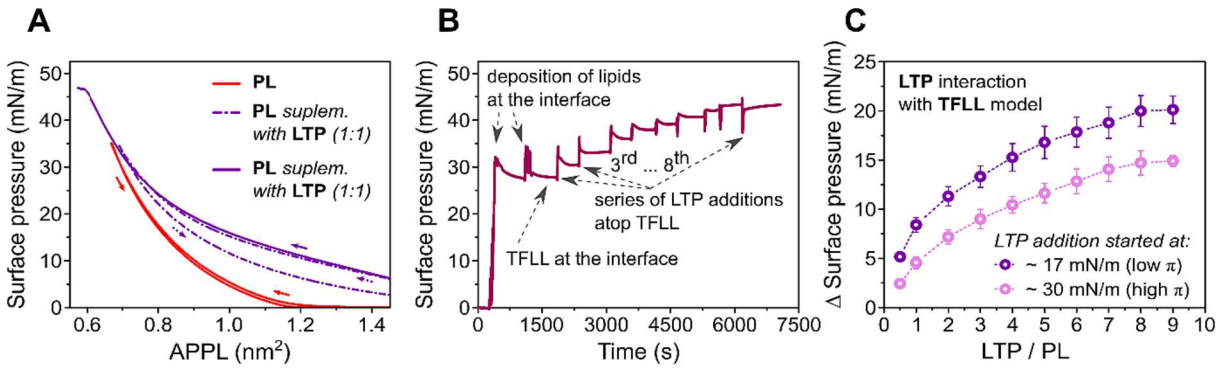

Fig. 1. (A) Compression-relaxation isotherms of PL monolayer before and after addition of latanoprost (LTP/PL 1:1). (B) Time dependence of surface pressure during the addition of LTP to the TFLL model (PL + BO + CE). (C) Dependence of the change of surface pressure on the LTP to PL molar ratio in the TFLL model.

distance. The v-rescale thermostat (Bussi et al., 2007) was used to keep the temperature constant at 310 K. All systems were simulated in duplicate with no qualitative differences detected between them. The composition of all simulated systems is shown in the Supporting Information (Table S1). The trajectories were analyzed using the standard GROMACS tools. For visualization and data processing, in-house Python scripts were applied. Trajectories were visualized with the VMD software (Humphrey et al., 1996). The presented data figures were prepared using the Matplotlib library (Hunter, 2007) and the Origin software, with the Inkscape package employed for minor graphical editions to improve data presentation.

3. Results and discussion

3.1. LTP accumulates in the in-vitro TFLL model

To assess the interactions between LTP and the lipid film spread at the water–air interface in a wide range of lateral packing, Langmuir isotherms were measured. This method allows us to monitor the changes of lateral pressure in a lipid film at the interface as a response to decreasing molecular area during continuous compression. In the first step, we focused on a purely polar lipid (PL) film. It should be noted that recent years have seen an extensive exploration of tear film lipidomics (Butovich, 2011; Chen et al., 2010). Despite this, some uncertainties about polar lipids persist, as indicated, for instance, in Millar and Schuett's review (Millar and Schuett, 2015). However, an ongoing debate in the scientific community suggests that the polar lipid OAHFA ((O-acyl)-ω-hydroxy fatty acid, which originates from the Meibomian glands) is principally accountable for film stability, with phospholipids having a more auxiliary role (Georgiev et al., 2017). In previous works, we evaluated both OAHFA (Paananen et al., 2020) and POPC (Olżyńska et al., 2020; Riedlová et al., 2023) as tear film polar lipid models. Our findings led us to conclude that the polar layer produced by POPC lipids aptly simulates the polar layer of TFLL, specifically concerning the biophysical properties. Further, in a separate investigation, we aligned POPC-based models with films created by Meibomian gland secretion and found substantial similarity between the two in terms of their interaction with pharmaceutical molecules and excipients (Eftimov et al., 2020). Consequently, in this research, while acknowledging the significance of OAHFA (Viitaja et al., 2021), we opted for POPC, which is more readily available, as a model for the polar layer of TFLL.

The lipids were deposited on the aqueous subphase, and a single compression-expansion cycle was run up to 35 mN/m, APPL = ~0.66 nm^2 (Fig. 1A, solid-red). The maximum pressure value was selected to ensure that the PL monolayer does not undergo collapse, which takes place above 45 mN/m in the Langmuir trough utilized in this study. The compression was followed by film relaxation down to lateral surface pressure ~0 mN/m, APPL = ~0.15 nm^2. The obtained compression-relaxation isotherm is typical for this PL (Olżyńska et al., 2020). After the initial cycle, LTP in a chloroform solution was added to the system by depositing small droplets with a Hamilton syringe from above the film. The final molar ratio of instilled LTP to PL was 1 to 1. As chloroform evaporated, homogenization of the film was observed visually, indicating that LTP spread at the PL-covered interface. The spreading was accompanied by increased surface pressure from 0 mN/m to ~6 mN/m (see Fig. 1A), indicating that LTP incorporated into the PL monolayer. The PL-LTP film was then compressed again to 35 mN/m. It is noticeable that the resulting isotherm (Fig. 1A, dashed-violet) is shifted towards higher surface pressure values across a broad range of APPL when compared with the isotherm obtained for pure PL monolayer (Fig. 1A, solid-red). Notably, the difference diminishes at higher pressure (~35 mN/m) where PL and PL + LTP isotherms virtually overlap. The observed behavior can be rationalized, assuming that the LTP molecules are forced out of the PL monolayer as the interfacial packing density rises. When the film was then relaxed, the resulting isotherm did not follow that of pure PL but was shifted to somewhat higher pressure. It indicates that the pushed-out LTP easily re-incorporates into the lipid monolayer during decompression; hence, it was not entirely squeezed out from the interface. The re-incorporation was confirmed by the position of the second compression isotherm run to the film collapse short after relaxation (Fig. 1, solid-violet), which overlaps with the first one (Fig. 1, dashed-violet). A plausible hypothesis at this point is that the portion of pushed-out LTP forms aggregates that stay attached to the surface film, either above or below it.

To mimic the post-instillation behavior of LTP in human TFLL, we investigated the effect of LTP supplementation to the TFLL model (PL + nonpolar lipids). To this end, we measured the kinetics of lateral pressure changes in the TFLL model after the addition of LTP. Note that the eye drop delivery is accompanied by continuous changes of lipid lateral packing caused by blinking. Therefore, we performed the measurements starting at two different surface pressures, i.e., ~17 and ~30 mN/m. The former value corresponds to moderate pressures at the PL + LTP isotherm, while the latter is close to the maximum. We prepared the mixed PL + BO/CE film, with 1:4 polar to nonpolar molar lipid ratio, 1:1 molar ratio of BO to CE. Following film stabilization, LTP in chloroform solution was added to the system stepwise by depositing small droplets with a Hamilton syringe atop the film. The representative kinetics of the TFLL model supplementation with LTP is shown in Fig. 1B. Following the addition of each drop, a sudden rise in surface pressure was noted due to the initial contact of the droplet with the film. However, the surface pressure stabilized and reached equilibrium before adding the next portion of LTP. The results obtained during the whole series of LTP supplementation demonstrate that upon the addition of LTP to the TFLL, the surface pressure successively increases with increasing LTP/PL molar ratio, thus indicating that LTP molecules accumulate in the TFLL.

In Fig. 1C, the increase of surface pressure after subsequent additions of LTP to the film is summarized for the two initial surface pressure values. It can be seen that saturation of surface pressure occurs while the

molar ratio of LTP to polar lipid ratio reaches 9 to 1. The extent of LTP accumulation is surprisingly high. The same trend was observed when starting from both medium and high surface pressures, thus proving that the polar lipid packing at the interface is not directly preventing LTP from its interactions and accumulation in the TFLL model. It suggests that LTP is not exclusively incorporated in the polar lipid layer but also localizes within the relatively thick nonpolar lipids region, which can accommodate the surplus LTP molecules.

In summary, these results indicate that LTP accumulates efficiently in the TFLL and support our hypothesis that TFLL can serve as a suitable reservoir for sustained drug release to the aqueous subphase. We should clarify that our experimental tear film and TFLL model is not designed to directly replicate the actual instillation of ophthalmic drops. The application of eye drops entails a range of processes, including the direct physical interaction of a drop with the tear film and the corneal surface and the swift removal of excess eye drops through tear duct channels and the sides of the eye. Additionally, the act of blinking after instillation mixes the drop material with the tear film, making the entire process dynamic. Subsequent eye blinks facilitate further mixing and prevent the system from reaching equilibrium. Also, our use of latanoprost in an organic solvent disrupts the lipid film before it re-forms, which does not directly mirror the post-instillation behavior of the film. Despite these facts, our system effectively captures the long-term interactions of the drug with the TFLL model while also identifying the role each lipid class plays. The primary discovery is the substantial incorporation of LTP into the model lipid layer.

3.2. LTP aggregates in bulk water and at the water–air interface

MD simulations were utilized to gain a molecular understanding of the behavior of LTP in the studied systems and rationalize the experimental findings. As a preparatory step, we examined how LTP molecules behave in pure water. To this end, fifty LTP molecules were randomly placed in a simulation box representing an aqueous environment with ~20,000 water molecules, and the MD trajectory of this system was simulated for 1 μs. The concentration of LTP in the simulated system box was ~25 mmol. For comparison, the 0.005% w/v LTP solutions typically used in ophthalmic products correspond to ~0.1 mmol concentration. The relatively high concentration was employed in MD to facilitate system equilibration on the microsecond timescale accessible for the simulations.

During simulation (see the snapshots in Fig. 2A-D), LTP molecules, which were initially randomly dispersed in water, readily interacted with each other, spontaneously forming small clusters (~1 ns timescale, Fig. 2A). These small clusters continued to grow and merge, resulting in the formation of bigger assemblies (Fig. 2B), until a single, large aggregate was formed on ~1 μs timescale. (Fig. 2C). The final large aggregate containing all LTP molecules remained stable for the rest of the simulation time (1 μs), as shown in Fig. 2D. Overall, this process represents a molecular-level nucleation of the water-insoluble LTP. Since the molecules in the formed nanocluster remained dynamic giving it liquid-like characteristics, the cluster can be viewed as a nanodrop of LTP in water.

We quantified the process of nanodrop formation by analyzing the contacts between the LTP molecules and water as a function of the simulation time, as shown in Fig. 3A. In the initial stages of the simulation (<1 ns), the drug molecules distributed randomly within the aqueous environment established significant contacts with water molecules. However, as the LTP molecules aggregated and formed clusters, the extent of their interactions with water molecules rapidly decreased within approximately 20 ns. This process effectively minimized and prevented unfavorable LTP-water interactions. The radius of gyration of the formed nanodrop was 1.6 nm. The drop size is, however, determined by the number of LTP present in the simulation box. If LTP is present in abundance, it can be expected that LTP-water phase separation would occur, as also known from experimentally established low solubility of LTP in water. We analyzed the structure of the LTP nanodrop by employing radial distribution functions (Fig. 3B). Somewhat surprisingly, the analysis shows that the core of the small LTP drop is formed by relatively polar CyP (dihydroxycyclopentyl) and CHOH (hydroxymethine) moieties, while Ph (phenyl) and i-Pr (isopropyl) are closer to the water interface (see Fig. 3D for group definition). It should be noted, however, that due to its small size, the drop does not have a fully formed interface with the surrounding water and hence the orientational preferences of molecules may not reflect their overall hydrophilic/hydrophobic character. Furthermore, as known from earlier experimental studies, LTP in water forms complex aggregates without a fully established structure (Ochiai and Danjo, 2011; Ochiai et al., 2012).

In the next stage, we simulated the behavior of LTP at a neat water–air interface. Such a system serves as good control and provides a valuable comparison with our model of TFLL. The water box containing the LTP aggregate (as in Fig. 2D) was elongated along one coordinate to form the water–air interface in MD. As a result, a simulation box with a slab of water in the center, with the LTP aggregate inside, and limited by two water-vacuum interfaces was formed (one-half of the system is shown in Fig. 2E). This system was then simulated for 1 μs. During simulation, the LTP drop migrated relatively quickly (<20 ns) from the bulk of water to one of the water–air interfaces and stayed there for the rest of the trajectory. The contact analysis (Fig. 3C) quantifies this process, showing that the number of LTP-water contacts diminished during the initial 20 ns and then remained stable. Importantly, at the interface, the drug remained in the form of a single aggregate (Fig. 2E) without forming a film-like structure; the molecules were organized randomly without any preferential orientation. This observation corroborates the experimentally reported lack of LTP surface activity. Interestingly, the tendency to form aggregates at the polar-nonpolar

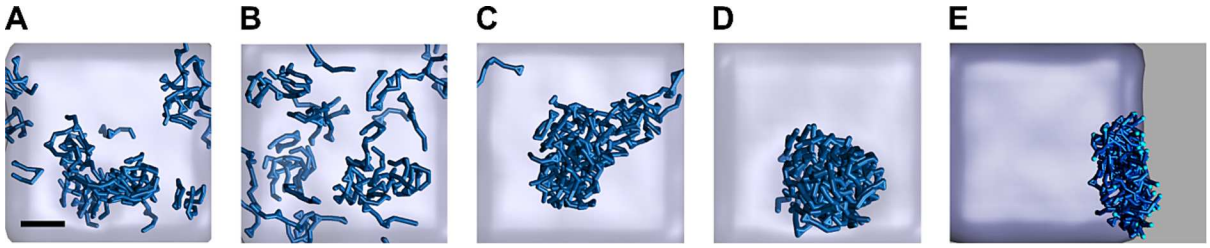

Fig. 2. (A-D) Formation of an LTP cluster in water and (E) at the water–air interface. The LTP molecules are represented in blue using a stick representation, and the water phase is shown in ice blue using a surface representation. The vacuum region in (E) is displayed in gray. Snapshots (A-D) demonstrate the formation of the LTP cluster from randomly distributed molecules over 1 μs of the MD trajectory performed in a cubic water box (~9 × 9 × 9 nm^3) with periodic boundary conditions. The snapshot (E), for presentation purposes, is cut to show only one of the two interfaces and depicts a final configuration with the LTP cluster from a 1 μs-long MD trajectory performed in an elongated periodic box (~9 × 9 × 15 nm^3) accounting for the vacuum phase. The drop formation process is driven by the lipophilicity of the drug, which favors LTP-LTP over LTP-water interactions. The LTP aggregate remains stable throughout the simulation (see Fig. 3A). Scale bar is 2 nm. (For interpretation of the references to colour in this figure legend, the reader is referred to the web version of this article.)

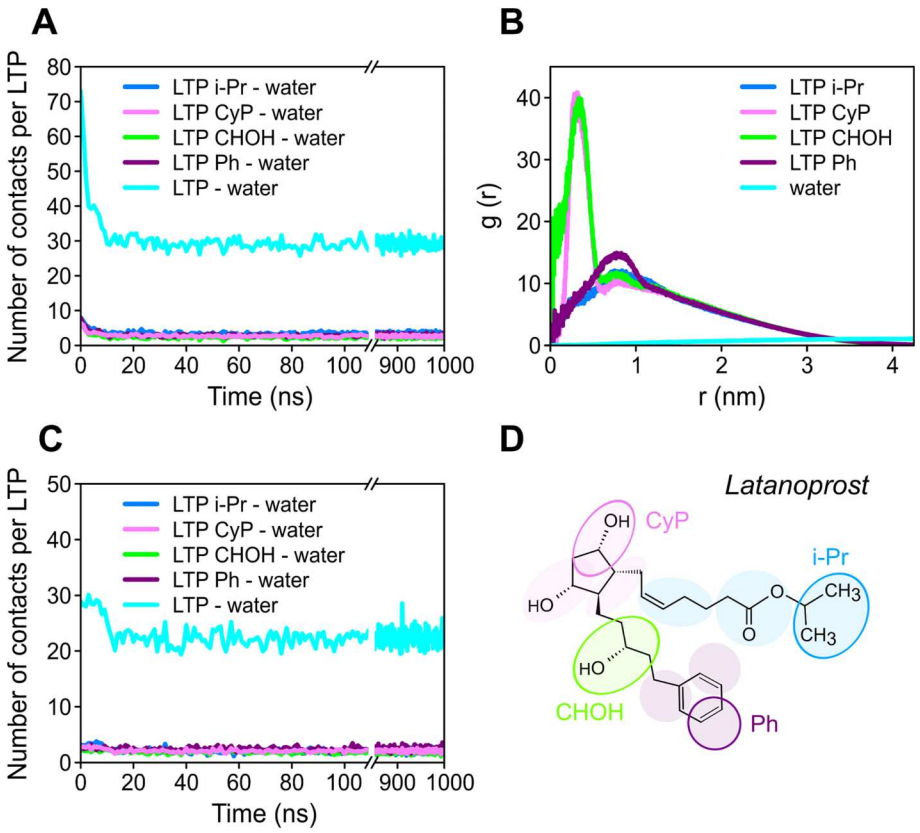

Fig. 3. (A) Formation of LTP cluster from random distribution in bulk water - contacts per LTP molecule vs time. (B) Characterization of the LTP cluster in water - radial distribution function. (C) LTP cluster at water-vacuum interface - contacts per LTP molecule vs time. (D) Specific LTP chemical groups discussed in the text are highlighted and named accordingly (the details regarding the LTP force field are given in the Supporting Information).

boundary observed here at the molecular scale also corroborates the macroscopically-observed tendency of LTP to adsorb at the walls of eye drop containers (Ochiai and Danjo, 2011).

Even though the LTP behavior in the aqueous phase and at the water–air interface described here does not mimic LTP in real drug delivery systems, these models are useful in demonstrating that the hydrophobic interactions between LTP molecules intrinsically drive the drug aggregation process. Furthermore, these simulations allow us the identification of chemical moieties in the drug molecule responsible for drug-drug and drug-water interactions.

3.3. MD simulations reveal molecular details of LTP-TFLL interactions

In order to gain a molecular insight of the LTP behavior in the presence of TFLL, we used an *in-silico* model of the human TFLL previously developed in our group (Wizert et al., 2014). The model consists of an aqueous subphase covered with a relatively thick (~8 nm) layer of lipids. The lipid layer is further organized and consists of a polar monolayer of POPC covered by a multilayer of an equimolar mixture of nonpolar BO and CE molecules (see Methodology for detail composition). This computational model was proven useful in studying the structure of TFLL and its interactions with drug molecules (Riedlová et al., 2023). In particular, thanks to its nanoscopic resolution, it allows investigation of the interactions of drug molecules at the molecular level with individual components of TFLL.

We examined the interactions between LTP and TFLL by positioning a nanoaggregate of LTP in the aqueous subphase and permitting it to spontaneously engage with the lipid film during 5 μs of MD simulation. To this end, we used the equilibrated cluster of fifty LTP molecules formed in the previously described simulations of LTP in the water phase (Fig. 2D). The packing of polar lipids at the interface was chosen in such a way that an average area per PL molecule amounted to 0.67 nm^2, thus corresponding to the relatively packed film conditions considered in our experiments (see Fig. 1B, C). The lateral size of the simulated patch of TFLL was ~20 × 20 nm^2. Representative simulation snapshots obtained along the MD trajectory are depicted in Fig. 4., and quantification of the simulated process is given via the contact analysis in Fig. 5A.

During simulation, the LTP aggregate diffused toward the lipid film (Fig. 4A) and engaged in direct interactions with lipids at ~60 ns (Fig. 4B). As visible in snapshots (Fig. 4C) and in the contacts analysis (Fig. 5A blue line), this stage was followed by ~20 ns-long intensive restructuring of LTP nanodrop, during which LTP was significantly dehydrated while interacting predominantly with PLs (Fig. 5A red line). During this phase, there were also instances of LTP forming direct contacts with nonpolar lipids (Fig. 5A olive and orange); however, these interactions were relatively minor compared to the LTP-PL interactions. This stage was followed by a long period (~300 ns) in which a buildup of LTP-PL contacts continued, finally reaching an equilibrium, depicted in the snapshot shown in Fig. 4D. The system remained stable for the following simulation time. The whole process led to incorporating LTP into the PL monolayer. In other words, the nanoaggregate of LTP was effectively dissolved in TFLL, mainly in its polar part.

We analyzed in detail LTP interactions with TFLL components after equilibration by means of the contacts between individual moieties in the drug molecules and lipids (Fig. 5B-C). The analysis proves that LTP interacts significantly with the heads of polar lipids and to a smaller extent with their tails. However, somewhat surprisingly, LTP is still predominantly involved in contacts with water. This behavior can be rationalized by the orientation of LTP molecules at the water–lipid interface. Namely, the molecules incorporate between PL headgroups in a bent conformation, not fully aligned with the molecules of lipids. Regarding interaction with lipids, the CyP (dihydroxycyclopentyl)

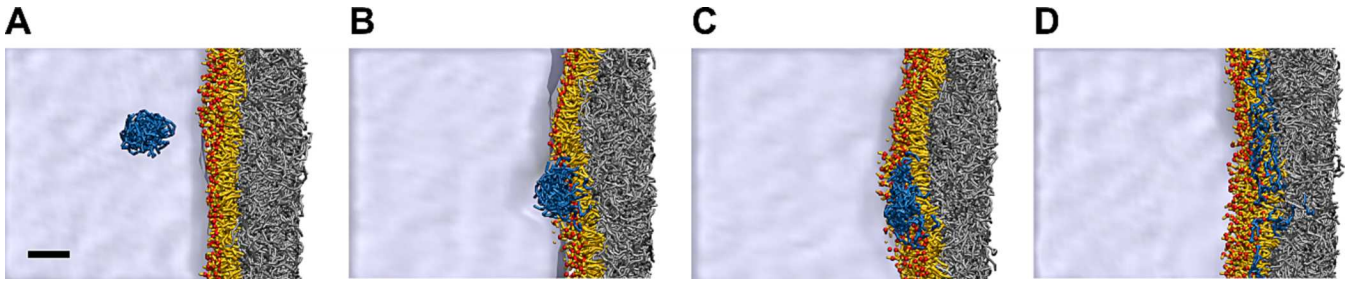

Fig. 4. Representative snapshots of the LTP molecule's diffusion in TFLL taken over a 2 μs MD trajectory in the simulation box of ~20 × 20 × 104 nm^3. LTP aggregate is shown as blue sticks; the PL monolayer is represented as red VdW (polar heads) and yellow sticks (nonpolar tails). BO and CE are in gray licorice representation. Water is shown as a gray continuous phase. (A) LTP pre-formed aggregate is added to the TFLL from the water phase. (B) and (C) LTP molecules start to incorporate into the polar monolayer of PL by interactions with the PL's head. (D) Spreading of LTP into the TFLL. Rendering of the snapshots is done with VMD software (Humphrey et al., 1996). The scale bar equals 4 nm. (For interpretation of the references to colour in this figure legend, the reader is referred to the web version of this article.)

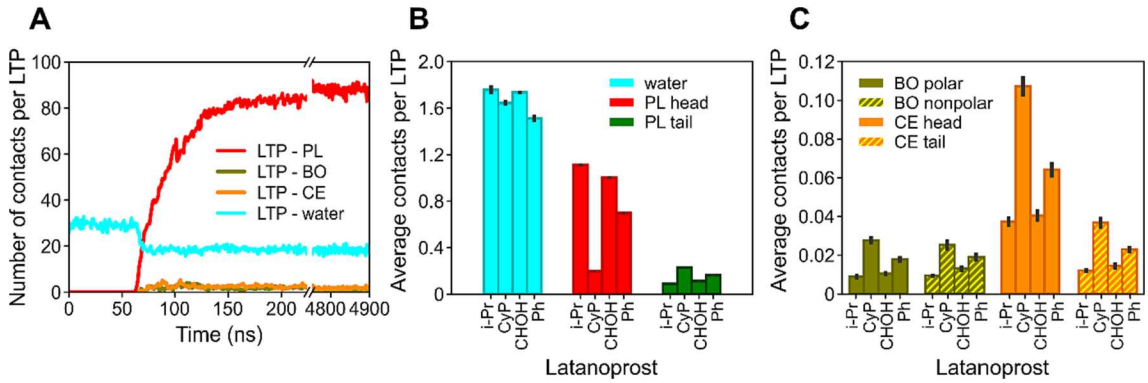

Fig. 5. (A) Number of contacts per LTP molecule along the MD simulation time (LTP from water phase). The contacts are calculated between all MARTINI beads of LTP molecules and beads of lipid species of the TFLL. After ~150 ns of simulation time, the contacts converge to constant values. (B) Average contacts after system equilibration calculated between selected groups of the LTP molecule (i-Pr, CyP, CHOH, and Ph) and PL (the phosphate group and the terminal of the *sn*-2 chain are shown) and water, within a cut-off of 0.7 nm. (C) Average contacts between selected chemical groups of the LTP molecule (i-Pr, CyP, CHOH, and Ph) and the two nonpolar lipid species, BO (ester group - polar, terminal of behenyl chain - nonpolar) and CE (cholesteryl moiety - head, terminal of the chain - tail), within a cut-off of 0.7 nm. In (B) and (C), to facilitate comparison between the groups consisting of different numbers of MARTINI beads, only one bead in each group was used for contact identification; hence these values do not sum up to the contact numbers in (A). The error bars represent the standard deviation from the block analysis.

moiety of LTP is an exception, having reduced contacts with PL heads. This is caused by the fact that the CyP group is involved in numerous contacts with nonpolar lipids, as visible in Fig. 5C. It is important to highlight that the CyP group is situated in the middle of the LTP chain, as depicted in Fig. 3D, further demonstrating the intricate conformation of LTP molecules in the TFLL model. In relation to nonpolar lipids, most interactions with the drug involve the cholesteryl moiety of CE (Fig. 5C). This can be attributed to its positioning within the TFLL model, as observed in our prior research (Wizert et al., 2014).

Incorporation of LTP in the TFLL caused to some extent an increase in interfacial packing and minor undulations of the polar lipid layer. However, this effect was small because of the low molar ratio of LTP to polar lipids (~7%). Nevertheless, the increased packing corroborates the elevated lateral pressure experimentally observed in LTP-containing lipid films. For comparison, we performed an additional simulation in which we reduced the lateral pressure of the system with LTP by removing some of the PLs. This resulted in a diminished undulation of the polar layer. We examined this system to gain more insights into the LTP's location within the TFLL model (see Supplementary Information, Fig. S2). Nonetheless, no qualitative differences were detected. Additionally, we simulated and analyzed a control system in which MD simulation was started with an LTP aggregate localized in the vacuum phase above the TFLL layer (see Supplementary Information, Figs. S2 and S3). In this case, LTP initially interacted with nonpolar lipids. It dissolved in the nonpolar layer and individual drug molecules diffused to the polar layer attaining conformation similar to that observed in standard simulations. The process was relatively long, with no full equilibration obtained over 12 μs. Such behavior indicates that LTP-nonpolar lipids interactions are not unfavorable.

4. Conclusions

This study aimed to investigate the interactions between latanoprost, the anti-glaucoma drug, and the tear film lipid layer by employing biomimetic acellular in vitro models of TFLL in tandem with in silico molecular modeling. Our experimental results showed that LTP interacts with lipids of TFLL, typically leading to increased molecular packing at the interface. Importantly, the concentration of LTP that the TFLL can accumulate is relatively high, up to a 9:1 molar ratio of LTP to PL.

In the molecular dynamics simulations, we showed that LTP in the aqueous phase forms micelle-like aggregates with a specific orientation of LTP molecules toward water. While at the pure water–air interface, the drug molecules also form an aggregate. MD simulations including the TFLL model showed that LTP rapidly (<100 ns of MD simulation time) dissolves in the lipid film, primarily localizing in the well-hydrated polar heads region and remaining in the TFLL. Subsequent release of LTP from the TFLL was not observed in duration of MD simulations. Interestingly, this contrasts with the pure water–air interface where LTP formed an aggregate. In the TFLL, minor interactions between LTP and nonpolar lipids were also observed. Moreover, simulations starting from a vacuum suggest that LTP can remain in the nonpolar layer for a prolonged period. Consequently, one might anticipate that the excess LTP

would be situated in the nonpolar layer with an increased LTP-to-lipid ratio. This supports our experimental observation that the TFLL model can accommodate a significant quantity of LTP.

It is essential to note that in clinical practice, LTP is not instilled as a pure aqueous solution but is typically delivered with other components, for instance, benzalkonium chloride or other surfactants, which form soluble aqueous micelles of LTP, as in Xalatan® or Monoprost®. Furthermore, after post-instillation disturbances of the tear film related to blinking, the drug interacts not only with the tear lipids but also with the aqueous tear phase, cornea, and conjunctiva. Still, one can expect that at least some fraction of the drug molecules interacts with TFLL. Our findings indicate that a substantial portion of this fraction has the capability to accumulate within the lipid layer of tears and may have therapeutic effects over an extended period, comparable with the turnover time of lipids in the tear film, which reaches up to several hours.

Given the large number of dynamic processes taking place within the tear film following the administration of eye drops, along with their non-equilibrium nature, it becomes challenging to accurately quantify the release of LTP from lipids using conventional measures such as free energy differences and partition coefficients since establishment of equilibrium for their calculation is implausible. To address this concern effectively, an in vitro method that takes into account the dynamics of the system directly would be required, which falls well outside the scope of this paper.

Our research on the model systems employed in this study provides insight into the inherent nanoscale arrangement of LTP and its interactions with tear lipids. A fundamental understanding of the behavior of drugs on a molecular level impacts the further development and optimization of drug formulations. Specifically, our findings indicate that delivery systems based on nonpolar lipids, such as oil-in-water emulsions, could prove valuable as they can potentially enhance the concentration of latanoprost in the lipid portion of the tear film.

CRediT authorship contribution statement

Kamila Riedlová: Investigation, Formal analysis, Visualization. **Maria Chiara Saija:** Investigation, Visualization, Writing – review & editing. **Agnieszka Olżyńska:** Investigation, Validation, Visualization, Data curation, Writing – original draft, Writing – review & editing. **Katarina Vazdar:** Investigation, Writing – review & editing. **Philippe Daull:** Conceptualization, Writing – review & editing. **Jean-Sebastien Garrigue:** Conceptualization, Writing – review & editing. **Lukasz Cwiklik:** Conceptualization, Project administration, Methodology, Validation, Formal analysis, Resources, Data curation, Supervision, Funding acquisition, Writing – original draft, Writing – review & editing.

Declaration of Competing Interest

The authors declare the following financial interests/personal relationships which may be considered as potential competing interests: Lukasz Cwiklik reports financial support was provided by SANTEN.

Philippe Daull reports a relationship with Santen that includes: employment.

Data availability

Data will be made available on request.

Acknowledgments

This work was supported by the Czech Science Foundation (grant no. 21-19854S).

Declaration of generative AI and AI-assisted technologies in the writing process

Language corrections and readability adjustments were partially performed using ChatGPT and Grammarly tools. After using these services, the authors reviewed and edited the content as needed and take full responsibility for the content of the publication.

Appendix A. Supplementary material

Supplementary data to this article can be found online at https://doi.org/10.1016/j.ijpharm.2023.123367.

References

Alm, A., 2014. Latanoprost in the treatment of glaucoma. Clin. Ophthalmol. 8, 1967–1985. https://doi.org/10.2147/OPTH.S59162.

Basu, S., Sjöquist, B., Stjernschantz, J., Resul, B., 1994. Corneal permeability to and ocular metabolism of phenyl substituted prostaglandin esters in vitro. PLEFA 50, 161–168. https://doi.org/10.1016/0952-3278(94)90139-2.

Berendsen, H.J., Postma, J.v., Van Gunsteren, W.F., DiNola, A., Haak, J.R., 1984. Molecular dynamics with coupling to an external bath. J. Chem. Phys. 81, 3684–3690. https://doi.org/10.1063/1.448118.

Bito, L., Baroody, R., 1987. The ocular pharmacokinetics of eicosanoids and their derivatives. 1. Comparison of ocular eicosanoid penetration and distribution following the topical application of PGF2α, PGF2α-1-methyl ester, and PGF2α-1-isopropyl ester. Exp. Eye Res. 44, 217–226. https://doi.org/10.1016/S0014-4835(87)80006-4.

Bussi, G., Donadio, D., Parrinello, M., 2007. Canonical sampling through velocity rescaling. J. Chem. Phys. 126, 014101 https://doi.org/10.1063/1.2408420.

Butovich, I.A., 2011. Lipidomics of human meibomian gland secretions: chemistry, biophysics, and physiological role of meibomian lipids. Prog. Lipid Res. 50, 278–301. https://doi.org/10.1016/j.plipres.2011.03.003.

Chen, J., Green-Church, K.B., Nichols, K.K., 2010. Shotgun lipidomic analysis of human meibomian gland secretions with electrospray ionization tandem mass spectrometry. IOVS 51, 6220–6231. https://doi.org/10.1167/iovs.10-5687.

Cwiklik, L., 2016. Tear film lipid layer: A molecular level view. Biochim. Biophys. Acta (BBA)-Biomembranes 1858, 2421–2430. https://doi.org/10.1016/j.bbamem.2016.02.020.

Diestelhorst, M., Krieglstein, G.K., Lusky, M., Nagasubramanian, S., 1997. Clinical dose-regimen studies with latanoprost, a new ocular hypotensive PGF2α analogue. Surv. Ophthalmol. 41, S77–S81. https://doi.org/10.1016/S0039-6257(97)80011-2.

Digiuni, M., Fogagnolo, P., Rossetti, L., 2012. A review of the use of latanoprost for glaucoma since its launch. Expert. Opin. Pharmacother. 13, 723–745. https://doi.org/10.1517/14656566.2012.662219.

Efron, N., Young, G., Brennan, N.A., 1989. Ocular surface temperature. 8, 901–906.

Eftimov, P., Olżyńska, A., Melcrová, A., Georgiev, G.A., Daull, P., Garrigue, J.-S., Cwiklik, L., 2020. Improving stability of tear film lipid layer via concerted action of two drug molecules: A biophysical view. Int. J. Mol. Sci. 21, 9490. https://doi.org/10.3390/ijms21249490.

European Glaucoma Society, 2017. Chapter 3: Treatment principles and options. Br. J. Ophthalmol. 101, 130–195. https://doi.org/10.1136/bjophthalmol-2016-egsguideline.003.

Fayyaz, A., Vellonen, K.-S., Ranta, V.-P., Toropainen, E., Reinisalo, M., Valtari, A., Puranen, J., Ricci, G.D.A., Heikkinen, E.M., Gardner, I., 2021. Ocular pharmacokinetics of atenolol, timolol and betaxolol cocktail: Tissue exposures in the rabbit eye. Eur. J. Pharm. Biopharm. 166, 155–162. https://doi.org/10.1016/j.ejpb.2021.06.003.

Georgiev, G.A., Eftimov, P., Yokoi, N., 2017. Structure-function relationship of tear film lipid layer: A contemporary perspective. Exp. Eye Res. 163, 17–28. https://doi.org/10.1016/j.exer.2017.03.013.

Grubmüller, H., Heller, H., Windemuth, A., Schulten, K., 1991. Generalized Verlet algorithm for efficient molecular dynamics simulations with long-range interactions. Mol. Simulat. 6, 121–142. https://doi.org/10.1080/08927029108022142.

Hedman, K., Larsson, L.-I., 2002. The effect of latanoprost compared with timolol in African-American, Asian, Caucasian, and Mexican open-angle glaucoma or ocular hypertensive patients. Surv. Ophthalmol. 47, S77–S89. https://doi.org/10.1016/S0039-6257(02)00310-7.

Humphrey, W., Dalke, A., Schulten, K., 1996. VMD: visual molecular dynamics. J. Mol. Graphics 14, 33–38. https://doi.org/10.1016/0263-7855(96)00018-5.

Hunter, J.D., 2007. Matplotlib: A 2D graphics environment. Comput. Sci. Eng. 9, 90–95. https://doi.org/10.1109/MCSE.2007.55.

Jonas, J.B., Aung, T., Bourne, R.R., Bron, A.M., Ritch, R., Panda-Jonas, S., 2017. Glaucoma. Lancet 390, 2183–2193. https://doi.org/10.1016/s0140-6736(17)31469-1.

Lazcano-Gomez, G., de los Angeles Ramos-Cadena, M., Torres-Tamayo, M., de Oteyza, A. H., Turati-Acosta, M., Jimenez-Román, J., 2016. Cost of glaucoma treatment in a developing country over a 5-year period. Medicine 95. https://doi.org/10.1097/MD.0000000000005341.

Lee, D.A., Higginbotham, E.J., 2005. Glaucoma and its treatment: a review. AJHP 62, 691–699. https://doi.org/10.1093/ajhp/62.7.691.

Marrink, S.J., Risselada, H.J., Yefimov, S., Tieleman, D.P., De Vries, A.H., 2007. The MARTINI force field: coarse grained model for biomolecular simulations. J. Phys. Chem. B 111, 7812–7824. https://doi.org/10.1021/jp071097f.

Martínez, L., Andrade, R., Birgin, E.G., Martínez, J.M., 2009. PACKMOL: A package for building initial configurations for molecular dynamics simulations. J. Comput. Chem. 30, 2157–2164. https://doi.org/10.1002/jcc.21224.

Millar, T.J., Schuett, B.S., 2015. The real reason for having a meibomian lipid layer covering the outer surface of the tear film–A review. Exp. Eye Res. 137, 125–138. https://doi.org/10.1016/j.exer.2015.05.002.

Mochizuki, H., Yamada, M., Hatou, S., Tsubota, K., 2009. Turnover rate of tear-film lipid layer determined by fluorophotometry. Br. J. Ophthalmol. 93, 1535–1538. https://doi.org/10.1136/bjo.2008.156828.

Ochiai, A., Danjo, K., 2011. The stabilization mechanism of latanoprost. Int. J. Pharm. 410, 23–30. https://doi.org/10.1016/j.ijpharm.2011.03.006.

Ochiai, A., Ohkuma, M., Danjo, K., 2012. Investigation of surfactants suitable for stabilizing of latanoprost. Int. J. Pharm. 436, 732–737. https://doi.org/10.1016/j.ijpharm.2012.07.027.

Olżyńska, A., Wizert, A., Štefl, M., Iskander, D.R., Cwiklik, L., 2020. Mixed polar-nonpolar lipid films as minimalistic models of tear film lipid layer: A langmuir trough and fluorescence microscopy study. Biochim. Biophys. Acta (BBA)-Biomembranes 1862, 183300. https://doi.org/10.1016/j.bbamem.2020.183300.

Paananen, R.O., Viitaja, T., Olżyńska, A., Ekholm, F.S., Moilanen, J., Cwiklik, L., 2020. Interactions of polar lipids with cholesteryl ester multilayers elucidate tear film lipid layer structure. Ocul. Surf. 18, 545–553. https://doi.org/10.1016/j.jtos.2020.06.001.

Patel, S.S., Spencer, C.M., 1996. Latanoprost: a review of its pharmacological properties, clinical efficacy and tolerability in the management of primary open-angle glaucoma and ocular hypertension. Drug. Aging 9, 363–378. https://doi.org/10.2165/00002512-199609050-00007.

Quigley, H.A., Broman, A.T., 2006. The number of people with glaucoma worldwide in 2010 and 2020. Br. J. Ophthalmol. 90, 262–267. https://doi.org/10.1136/bjo.2005.081224.

Riedlová, K., Saija, M.C., Olżyńska, A., Jurkiewicz, P., Daull, P., Garrigue, J.-S., Cwiklik, L., 2023. Influence of BAKs on tear film lipid layer: In vitro and in silico models. Eur. J. Pharm. Biopharm. 186, 65–73. https://doi.org/10.1016/j.ejpb.2023.03.007.

Sjöquist, B., Stjernschantz, J., 2002. Ocular and systemic pharmacokinetics of latanoprost in humans. Surv. Ophthalmol. 47, S6–S12. https://doi.org/10.1016/S0039-6257(02)00302-8.

Sommer, A., 1989. Intraocular pressure and glaucoma. Am. J. Ophthalmol. 107, 186–188. https://doi.org/10.1016/0002-9394(89)90221-3.

Taylor, H.R., 2019. Global blindness: the progress we are making and still need to make. Asia Pac. J. Ophthalmol. (Phila.) 8, 424–428. https://doi.org/10.1097/APO.0000000000000264.

Tham, Y.-C., Li, X., Wong, T.Y., Quigley, H.A., Aung, T., Cheng, C.-Y., 2014. Global prevalence of glaucoma and projections of glaucoma burden through 2040: a systematic review and meta-analysis. Ophthalmology 121, 2081–2090. https://doi.org/10.1016/j.ophtha.2014.05.013.

Thiruchelvi, R., Shivanika, C., 2021. In-Silico analysis to identify the potent inhibitor of Rho GTPase activating protein for the usage of the Glaucoma. Mater. Today.-Proc. 37, 1897–1904. https://doi.org/10.1016/j.matpr.2020.07.470.

Traverso, C., Walt, J., Kelly, S., Hommer, A., Bron, A.M., Denis, P., Nordmann, J., Renard, J., Bayer, A., Grehn, F., 2005. Direct costs of glaucoma and severity of the disease: a multinational long term study of resource utilisation in Europe. Br. J. Ophthalmol. 89, 1245–1249. https://doi.org/10.1136/bjo.2005.067355.

Van Der Spoel, D., Lindahl, E., Hess, B., Groenhof, G., Mark, A.E., Berendsen, H.J., 2005. GROMACS: fast, flexible, and free. J. Comput. Chem. 26, 1701–1718. https://doi.org/10.1002/jcc.20291.

Varma, R., Lee, P.P., Goldberg, I., Kotak, S., 2011. An assessment of the health and economic burdens of glaucoma. Am. J. Ophthalmol. 152, 515–522. https://doi.org/10.1016/j.ajo.2011.06.004.

Viitaja, T., Raitanen, J.-E., Moilanen, J., Paananen, R.O., Ekholm, F.S., 2021. The properties and role of O-Acyl-ω-Hydroxy fatty acids and type I-St and type II diesters in the tear film lipid layer revealed by a combined chemistry and biophysics approach. J. Org. Chem. 86, 4965–4976. https://doi.org/10.1021/acs.joc.0c02882.

Weinreb, R.N., Aung, T., Medeiros, F.A., 2014. The pathophysiology and treatment of glaucoma: a review. JAMA 311, 1901–1911. https://doi.org/10.1001/jama.2014.3192.

Wizert, A., Iskander, D.R., Cwiklik, L., 2014. Organization of lipids in the tear film: a molecular-level view. PLoS One 9, e92461.

Wizert, A., Iskander, D.R., Cwiklik, L., 2017. Interaction of lysozyme with a tear film lipid layer model: A molecular dynamics simulation study. Biochim. Biophys. Acta (BBA)-Biomembranes 1859, 2289–2296. https://doi.org/10.1016/j.bbamem.2017.08.015.

Wu, X., Yang, X., Liang, Q., Xue, X., Huang, J., Wang, J., Xu, Y., Tong, R., Liu, M., Zhou, Q., 2021. Drugs for the treatment of glaucoma: Targets, structure-activity relationships and clinical research. Eur. J. Med. Chem. 226, 113842 https://doi.org/10.1016/j.ejmech.2021.113842.

2 Supporting information of Publication I

SUPPORTING INFORMATION

Latanoprost incorporates in the Tear Film Lipid Layer: an experimental and computational model study

Kamila Riedlová,[1, 2] Maria Chiara Saija,[1, 2] Agnieszka Olżyńska,[1*] Katarina Vazdar,[1] Philippe Daull,[3] Jean-Sebastien Garrigue,[3] and Lukasz Cwiklik[1*]

[1]J. Heyrovský Institute of Physical Chemistry, Czech Academy of Sciences, Dolejškova 3, 18223 Prague, Czech Republic

[2]Department of Physical and Macromolecular Chemistry, Faculty of Science, Charles University, Hlavova 8, 12800, Prague, Czech Republic

[3]SANTEN SAS, Novagali Innovation Center, 1 rue Pierre Fontaine, Bâtiment Genavenir IV, CEDEX F-91458 Evry, France

[*]corresponding authors: agnieszka.olzynska@jh-inst.cas.cz; lukasz.cwiklik@jh-inst.cas.cz

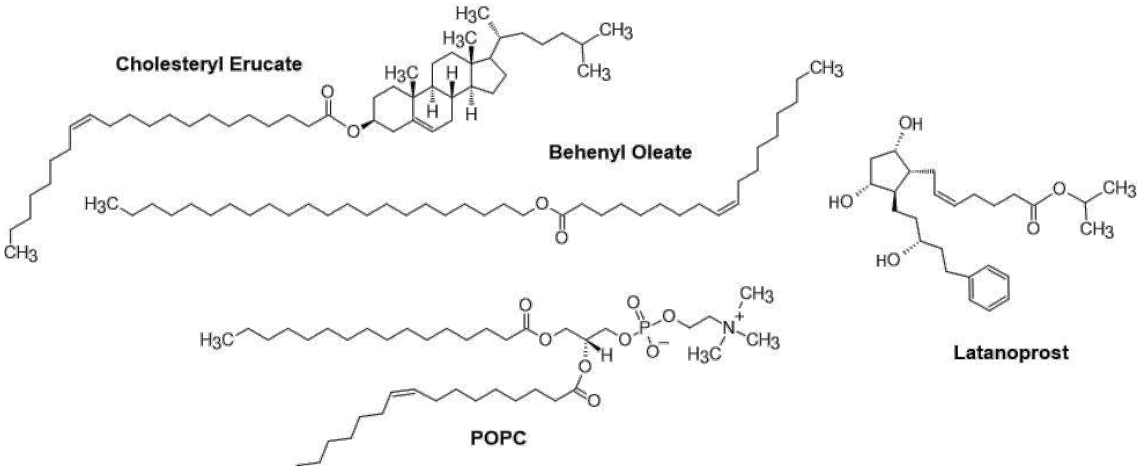

Fig. S1. Structures of the considered molecules: latanoprost (LTP), behenyl oleate (BO), cholesteryl erucate (CE), and 1-palmitoyl-2-oleyl-sn-glycero-3-phosphocholine (POPC).

Table S1. MD systems composition.

System	#LTP	#POPC	#BO	#CE	#water beads[2]	Trajectory length[3] (μs)
LTP_{bulk}	50	0	0	0	4884	1
$LTP_{water\text{-}air}$	50	0	0	0	4884	1
$LTP_{TFLL\ air}$	50	1454	2500	2500	87354	12
$LTP_{TFLL20\ air}$[1]	50	1164	2500	2500	87345	1.6
$LTP_{TFLL\ water}$[1]	50	1454	2500	2500	87354	5
$LTP_{TFLL20water}$[1]	50	1164	2500	2500	87354	1.6

[1] Molecule numbers for the two interfaces of the TFLL model are given. The total number of molecules was equally divided between the two interfaces in the simulation box. [2] Note that each water bead represents four water molecules in the MARTINI force field. [3] Lipid diffusion is somewhat retarded in lipid membranes; it is roughly estimated that the MARTINI simulation time in lipid systems is ~four times shorter than real-time.

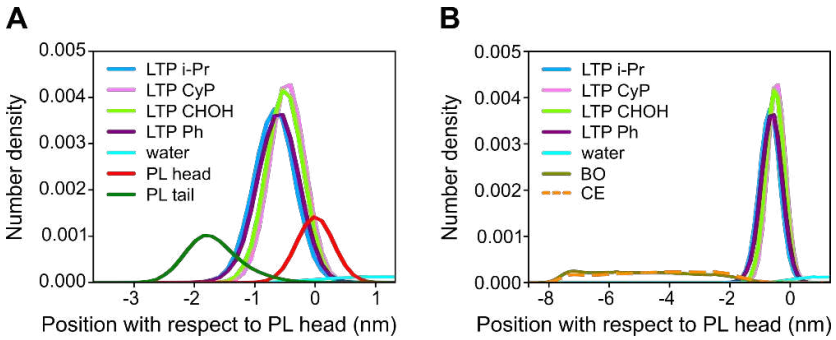

Fig. S2. Density profiles of latanoprost molecules in the TFLL with reduced lateral packing. The signal of latanoprost is presented with the profiles of polar (A) and nonpolar (B) lipids. The profiles were calculated employing the standard *gmx density* tool in GROMACS, along the direction perpendicular to the interface. The density profiles were computed on the last 600 ns of an equilibrated trajectory with a reduced lateral packing (system $LTP_{TFLL20water}$ from Table S1). The profiles show that LTP localizes preferentially in the polar PL monolayer with minor interactions with nonpolar lipids. Qualitatively, the result fully corresponds to the contact analysis obtained for the system with the increased lateral packing (Fig. 6 in the main manuscript).

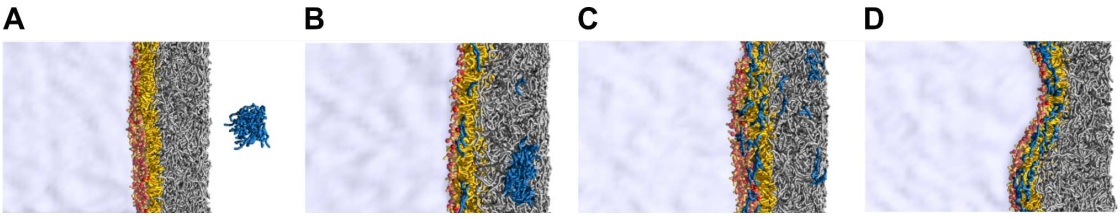

Fig. S3. Representative snapshots of the LTP cluster added to TFLL from the air taken over a 2 μs trajectory. The size of the simulation box was fixed to 20×20×104 nm^3. LTP aggregate is shown with blue sticks; the PL monolayer is represented as red spheres (polar heads) and yellow sticks (nonpolar tails). BO and CE are in gray licorice representation. Water is shown as a continuous gray phase. (A) LTP pre-formed aggregate was added to the TFLL from the air. (B) and (C) LTP molecules started incorporating into the nonpolar TFLL layer and eventually reached the PL monolayer. (D) Retention of LTP in PL monolayer.

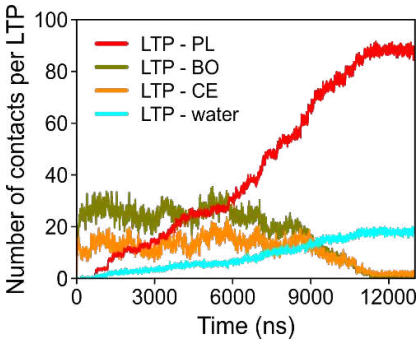

Fig. S4. Number of contacts per an LTP molecule as a function of simulation time (LTP added from the air phase). The contacts were calculated between the LTP molecules and the individual lipid species of the TFLL. The contacts converged to a constant value after ~12000 ns of simulation time.

3 Publication II: Influence of BAKS on tear film lipid layer: In vitro and in silico models

European Journal of Pharmaceutics and Biopharmaceutics 186 (2023) 65–73

Contents lists available at ScienceDirect

European Journal of Pharmaceutics and Biopharmaceutics

journal homepage: www.elsevier.com/locate/ejpb

Research paper

Influence of BAKs on tear film lipid layer: In vitro and in silico models

Kamila Riedlová [a,b], Maria Chiara Saija [a,b], Agnieszka Olżyńska [a], Piotr Jurkiewicz [a], Philippe Daull [c], Jean-Sebastien Garrigue [c], Lukasz Cwiklik [a,*]

[a] J. Heyrovský Institute of Physical Chemistry, Czech Academy of Sciences, Dolejškova 3, 18223 Prague, Czech Republic
[b] Department of Physical and Macromolecular Chemistry, Faculty of Science, Charles University, Hlavova 8, 12800 Prague, Czech Republic
[c] SANTEN SAS, Novagali Innovation Center, 1 rue Pierre Fontaine, Bâtiment Genavenir IV, CEDEX F-91458 Evry, France

ARTICLE INFO

Keywords:
Topical ophthalmic formulations
Tear film
Tear film lipid layer
Benzalkonium chloride
Lipid films
Molecular dynamics

ABSTRACT

Benzalkonium chloride (BAK) compounds are commonly used in topical ophthalmic products as preservatives and stabilizers. BAK mixtures containing several compounds with different alkyl chain lengths are typically used. However, in chronic eye conditions, such as dry eye disease and glaucoma, the accumulation of adverse effects of BAKs was observed. Hence, preservative-free eye drops formulations are preferred. On the other hand, selected long-chain BAKs, particularly cetalkonium chloride, exhibit therapeutic functions, promoting epithelium wound healing and tear film stability. Nevertheless, the mechanism of BAKs influence on the tear film is not fully understood. By employing in vitro experimental and in silico simulation techniques, we elucidate the action of BAKs and demonstrate that long-chain BAKs accumulate in the lipid layer of the tear film model, stabilizing it in a concentration-dependent fashion. In contrast, short-chain BAKs interacting with the lipid layer compromise the tear film model stability. These findings are relevant for topical ophthalmic drug formulation and delivery in the context of selecting proper BAK species and understanding the dose dependency for tear film stability.

1. Introduction

Long-term use of topical ophthalmologic drug formulations is a common characteristic in chronic eye conditions such as glaucoma (GLC) and dry eye disease (DED). As multiple daily doses of a drug are administered during extended periods of time, side effects of a treatment, which can accumulate in time, are of particular concern [1,2]. Notably, such a buildup of adverse effects was observed in the case of eye drop formulations containing commonly used benzalkonium chloride (BAK) excipients [3,4]. Therefore, many preservative-free, meaning BAKs-free, topical products have been introduced in recent years [2,5].

BAKs are typically used in ophthalmologic topical formulations in the form of mixtures containing several compounds with different lengths of the alkyl chain, mainly from C12 to C14, lower amounts of C8, C10, and trace amounts of C16 [6]. When present, they play several roles. First, they act as preservative agents thanks to the bactericidal and microbicidal properties of the C12 and C14 alkyl chain form of the quaternary ammonium [7]. Second, as surfactants, they stabilize micellar and nanodroplet formulations, for example, in the latanoprost preparation Xalatan® [8,9]. Third, some BAKs exhibit direct therapeutic functions. In particular, the C16-chain cetalkonium chloride (CKC) positively affects the corneal epithelium wound healing properties and the tear film stability when formulated in emulsions [6], in contrast to the mixtures of BAKs with shorter chain lengths (<C14). Indeed, this was observed in clinical settings where 0.002 to 0.005% CKC emulsions were demonstrated to improve the corneal epithelium wound healing process in DED patients [10–14]. To the best of our knowledge, so far, it was not reported that CKC-containing artificial tears or drug products induced tolerability issues in dry eye patients. The underlying mechanism of CKC's action in the cornea was shown to be related to its anti-inflammatory property via specific inhibition of the protein kinase C alpha (PKCα) [15,16]. On the other hand, the therapeutic function of CKC in the tear film is still not fully understood.

We previously employed a mixed in vitro and in silico approach to study the interactions between CKC and tear film lipid layer (TFLL). We demonstrated that CKC localizes in TFLL at low concentrations (~10^{-7} M) and stabilizes it mechanically [17]. Furthermore, we showed that at low concentrations, CKC could act in synergy with other ophthalmic drugs [18]. Concerning the differences between C16 CKC and other shorter BAKs, the in silico molecular modeling hinted at the mechanism of TFLL destabilization by short-chain BAKs due to the mismatch of their chain length with polar lipids of TFLL [17]. However, a complete insight

* Corresponding author.
E-mail address: lukasz.cwiklik@jh-inst.cas.cz (L. Cwiklik).

https://doi.org/10.1016/j.ejpb.2023.03.007
Received 16 January 2023; Received in revised form 10 March 2023; Accepted 13 March 2023
Available online 16 March 2023
0939-6411/© 2023 Elsevier B.V. All rights reserved.

regarding BAKs' influence on tear film (TF), particularly at high concentrations, is missing. Note that the ocular drug delivery with drops is inherently related to significant changes in the drug concentration in the precorneal area with a high concentration at drop instillation, which then rapidly declines [19,20].

Here, we comprehensively study the influence of selected BAKs (Fig. 1) at different concentrations on a realistic TFLL model. To this end, we combine in vitro methods with in silico molecular simulations. We show that short BAKs destabilize TFLL while the long CKC stabilizes it, and the effect is concentration-dependent. We explain these observations (in agreement with clinical ones) at both macro- and nanoscales. These results are relevant for topical delivery in the context of the selection of BAKs and an understanding of dose dependency for TF stability.

2. Methodology

2.1. Experimental

2.1.1. Materials

1-palmitoyl-2-oleyl-*sn*-glycero-3-phosphocholine (POPC) was purchased from Avanti Polar Lipids (Alabaster, AL). Behenyl oleate (BO) and cholesteryl erucate (CE) were ordered from Larodan (Solna, Sweden). Benzalkonium chlorides, C8 (BAK8), C12 (BAK12), and cetalkonium chloride (CKC) were supplied by Santen (Evry, France). Fluorescent probes, 1,2-dioleoyl-*sn*-glycero-3-phosphoethanolamine-Atto 633 (DOPE–Atto633), 4,4-difluoro-1,3,5,7,8-pentamethyl-4-bora-3a,4a-diaza-s-indacene (Bodipy 493/503), and 6-lauroyl-2-dimethylaminonaphthalene (Laurdan), were ordered from ATTO-TEC (Siegen, Germany), Thermo Fisher Scientific (Waltham, MA), and Invitrogen (Eugene, OR), respectively. Organic solvents, chloroform, methanol, and ethanol, of spectroscopic grade were purchased from Merck (Darmstadt, Germany). Phosphate-buffered saline (PBS) (Merck, Darmstadt, Germany) was prepared using Milli-Q water (Milipore, USA). After the addition of 0.2 mM ethylenedinitrilotetraacetic acid (EDTA) (Sigma-Aldrich, St. Louis, MO), it was used as a subphase in all experiments.

2.1.2. Langmuir isotherms

The lipid film was deposited from a chloroform solution (1 mM) with a Hamilton syringe over an aqueous subphase containing none or one of the BAK components in the Langmuir trough (Kibron, Helsinki, Finland) equipped with a surface pressure sensor (KBN 315; Kibron) with the DyneProbe. After chloroform evaporation and formation of a lipid film at the aqueous-air interface (~8 min), surface pressure-molecular area isotherms were measured. All measurements were performed at 34.4 °C, corresponding to the temperature of the human cornea [21]. The system's temperature was controlled by the metal plate with circulating water from the attached thermostat placed below the trough. The film deposition was performed at completely opened barriers, corresponding to low material packing at the interface and hence low lateral pressure. For each system, first, three fast compression-relaxation cycles (at ~0.55 (nm^2/chain)/minute; for pure POPC monolayer) were run by the symmetrical movement of two barriers up to the surface pressure of 35 mN/m, then the isotherm was recorded at slow compression speed (at ~0.04 (nm^2/chain)/minute; for pure POPC monolayer) up to the collapse. Usually, three measurements were performed for each system, while only representative isotherms are presented further in the figures. For quantification of the lipid packing at the interface, area per polar lipid (APPL) was used. It was defined as a ratio of the number of POPC molecules to the surface area spanned by the film. APPL allows quantification and direct comparison of interfacial lipid packing in pure POPC and mixed POPC-nonpolar films [22]. Compressibility modulus C_s^{-1} was calculated for the isotherms using a standard definition [23].

2.1.3. Widefield fluorescence imaging

Widefield fluorescence imaging was performed using an inverted fluorescence microscope (Olympus, Hamburg, Germany) and MicroTroughXS setup (Kibron, Helsinki, Finland) with the in-house modified stainless steel trough with PTFE edges and a glass window. Fluorescent probes, DOPE–Atto633 (referred to as "red") and Bodipy 493/503 (referred to as "blue"), were added simultaneously to the TFLL model film in the lipid-to-probe ratio 500 to 1 (mol/mol) and were excited with a Mercury lamp with its intensity controlled with neutral density filters. The excitation and emission beams were passing through an air objective UPlanSApo 10× (NA 0.4, WD 3.1 mm; Olympus, Tokyo, Japan) and two interchangeably used filter cubes mounted in the light pathway; i.e., Cy5-A-Basic-000 (single-band 630/38 excitation and 694/44 emission filters; Semrock, Rochester, NY) and U-MWB2 (single-band 475/30 excitation and 525/39 emission filters; Olympus, Tokyo, Japan). The fluorescence signal was recorded with a CMOS camera (IDS, Obersulm, Germany), and the time exposure was 100 ms.

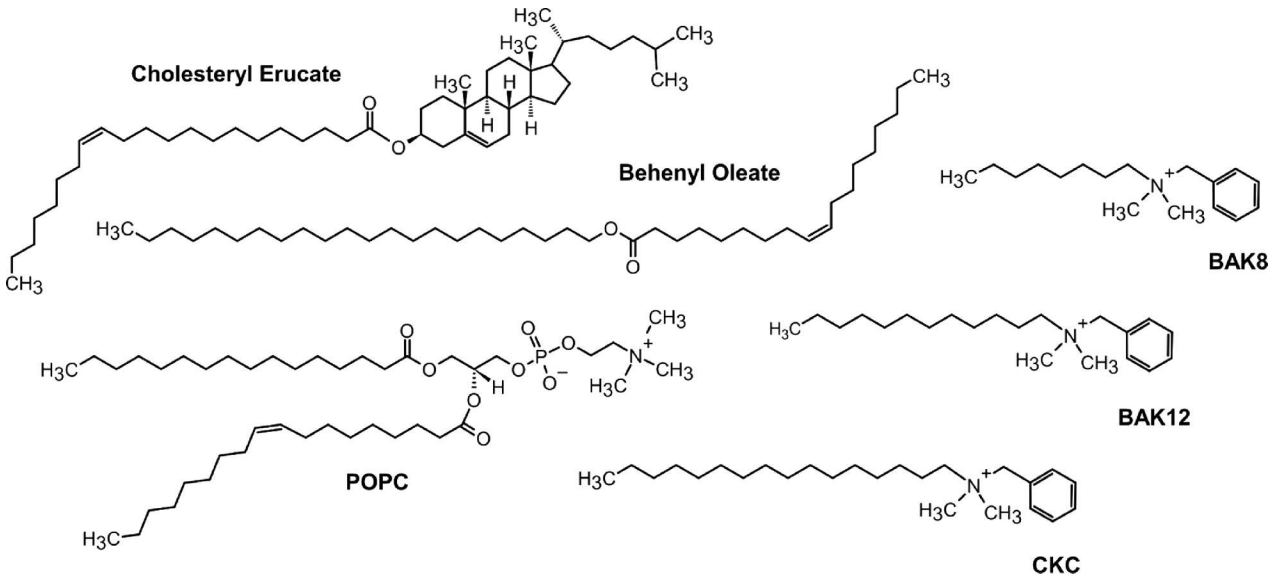

Fig. 1. Structures of the considered molecules: cholesteryl erucate (CE), behenyl oleate (BO), 1-palmitoyl-2-oleyl-*sn*-glycero-3-phosphocholine (POPC), benzalkonium chlorides C8 (BAK8), benzalkonium chlorides C12 (BAK12), and cetalkonium chloride (CKC).

2.1.4. GP imaging

Generalized polarization (GP) measurements were performed using the same confocal microscope body (Olympus, Hamburg, Germany) and Langmuir setup (MicroTroughXS; Kibron, Helsinki, Finland) as for the widefield imaging. Methanol solution of Laurdan was added to the lipid-in-chloroform mixture at the ratio of 1 to 100 (mol/mol) before film deposition at the aqueous-air interface. After the organic solvents evaporated (~8 min), the film was compressed to a selected surface pressure value and 5 min later imaged using water-immersion UPlanSApo 60x objective (NA 1.2, WD 0.28 mm; Olympus, Tokyo, Japan). Laurdan was excited with the picosecond diode laser (LDH-P-C-405; PicoQuant, Berlin, Germany). To calculate GP values, 2D confocal intensity images in the film plane were acquired with SPAD detectors (MPD, Bolzano, Italy) at two emission wavelength ranges, i.e., 419–465 (band-pass filter CFW BP01-Clin-25; Semrock, Rochester, NY) and 473–515 nm (band-pass filter FF01-494-41-25; Unice, Taoyuan City, Taiwan). The GP values were calculated from the recorded intensity images using Python software according to the equation:

$$GP = (I(440) - I(490))/(I(440) + I(490)),$$

where I(440) and I(490) are the emission intensities collected at 419–465 and 473–515 nm wavelength ranges, respectively.

Since GP values depend on instrumental settings (filters, detectors, objectives), calibration is necessary. For this purpose, suspension of Laurdan-labeled POPC small unilamellar vesicles (SUVs) was used. Correction factors for each channel were determined based on the comparison of the results obtained for the same POPC SUVs sample at the same temperature on the confocal microscope and using spectrofluorometer FS5 (Edinburgh Instruments, Edinburg, UK).

Histogramming of the GP images was performed employing ImageJ software.

2.2. MD simulations

In silico molecular modeling of TFLL was conducted using coarse grain molecular dynamics (MD) simulations. MD is a standard computational method used in biophysics which in recent years also proved extremely useful in pharmaceutical research, including drug delivery [24] and interactions of drugs with TFLL [18]. The mimic of TFLL used in the simulations is based on our previous work [22]. We employed a minimalistic model of polar lipids with one polar lipid component (1-palmitoyl-2-oleoyl-phosphatidylcholine, POPC) [25]. Nonpolar lipids were modeled as an equimolar mixture of cholesteryl erucate (CE) and behenyl oleate (BO), which are a good representation of nonpolar lipids in TF [26]. In accordance with lipidomics and similar to our previous studies, the TFLL model was characterized by an abundance of nonpolar lipids (here, 4:1 nonpolar to polar molar ratio) [27]. Interactions of all molecules were described using the coarse-grained MARTINI force field [28] and the force field parameters are presented in the Supporting Information.

Detailed compositions of all simulated systems are given in Table S1 in the Supporting Information. First, we simulated the behavior of BAK molecules in the bulk of water at different concentrations, from 20 to 200 mmol. Here, the NVT ensemble was used with a cubic simulation box of ~19 × 19 × 19 nm^3 at the temperature of 310 K. Next, we opened the equilibrated box in one direction (with the final size of ~19 × 19 × 60 nm^3), thus forming a system with two water–air interfaces, and simulated behavior of BAK molecules at the water surface. Finally, we conducted multiple simulations employing a pre-equilibrated TFLL model. In this model, an elongated simulation box (~22 × 22 × 104 nm^3) was used with the NVT ensemble at 310 K. A water slab was placed in the box, forming two water–air interfaces. At these interfaces, TFLL-mimicking lipids (as described beforehand) were placed. After equilibration, at both interfaces, the lipids formed a monolayer of polar POPC covered with a thick layer of nonpolar CE and BO, in agreement with previous in silico TFLL modeling studies [22,29]. In such a pre-equilibrated system, BAK molecules (BAK8, BAK12, or CKC) were added to the water subphase at either low (40 mmol) or high (150 mmol) concentrations. The resulting system was then simulated for additional 1 μs, reaching an equilibrium. The simulations were performed using the GROMAC software package [30]. Further computational details are given in the Supporting Information. The simulated systems were visualized with VMD [31] and numerical results were analyzed by in-house Python scripts and visualized using the Python matplotlib library [32].

3. Results and discussion

3.1. Experimental

3.1.1. BAKs influence film packing

The influence of BAKs on lateral pressure and packing of TFLL models was investigated experimentally by employing the Langmuir trough technique. A synthetic in vitro model of TFLL consisting of a lipid film containing a 1:4 (mol/mol) mixture of polar and nonpolar lipids was prepared and measured. POPC served as the polar lipid, and the 1:1 (mol/mol) mixture of BO and CE was used as nonpolar lipids. Such a lipid composition mimics the actual composition of human TFLL, which consists of a relatively small fraction of polar lipids and a more extensive fraction of nonpolar lipids, with wax esters (WE) and CE forming up to 95% of the whole TFLL lipidome [27]. Nevertheless, we previously showed that synthetic films similar to the one used here can mimic the basic biophysical behavior of human TFLL extracts and their interactions with drugs [18].

Before measuring the complete TFLL model system, a pure POPC film was studied to estimate the amount of lipid material necessary for isotherm measurements on the Langmuir trough. To this end, 12.5 nmol of POPC was deposited at the water–air interface with completely opened Langmuir trough barriers (corresponding to the area per polar lipid APPL = 1.4 nm^2) to obtain ~ zero initial surface pressure. Next, the surface pressure-surface area isotherm was recorded by closing the barriers and hence reducing APPL (Fig. 2A dashed line). With the amount of POPC used, a full isotherm was collected, i.e., spanning from zero to nearly 50 mN/m pressure where a film collapse occurred.

Next, the TFLL model was studied by depositing the polar-nonpolar lipid mixture at the aqueous interface with completely opened barriers. Notably, the amount of polar POPC in the deposited material was the same as that used for pure POPC measurements (12.5 nmol, APPL = 1.4 nm^2). The resulting TFLL isotherm is shown in Fig. 2A (solid line). The initial lateral pressure of the deposited TFLL model was ~5 mN/m, in contrast to the ~ zero value for the pure POPC film. It shows that in TFLL, nonpolar lipids at least partially co-spread with POPC at the water–air interface, increasing the lateral lipid packing. With closing the Langmuir trough barriers and hence reducing APPL, the TFLL isotherm shows a smooth increase of surface pressure up to ~48 mN/m where the film collapses. A similarly smooth behavior is observed for the pure POPC film. In the large and moderate APPL (0.7–1.4 nm^2), the lateral pressure of TFLL is above that of pure POPC, showing that nonpolar lipids are present at the water–lipid interface. On the contrary, for APPL < 0.7 nm^2, the lateral pressure is reduced with respect to POPC, demonstrating that the TFLL model restructures with nonpolar lipids being squeezed out from the interface together with some polar lipids. We previously observed such behavior for different TFLL models. The mechanical properties of thin films can be further analyzed by means of the lateral compressibility modulus C_s^{-1}, shown in Fig. 2C. According to Davies and Rideal classification, for lipid films, the compressibility modulus is related to the state (phase) of the film [33]. The values of 0–12.5 mN/m correspond to the gas phase, 12.5–50 mN/m to the liquid-expanded phase (LE), 50–100 mN/m to the coexistence of LE and liquid-condensed phase (LC) denoted as LE/LC, 100–250 mN/m to the liquid-condensed phase. For the TFLL model, the LE phase is detected for large

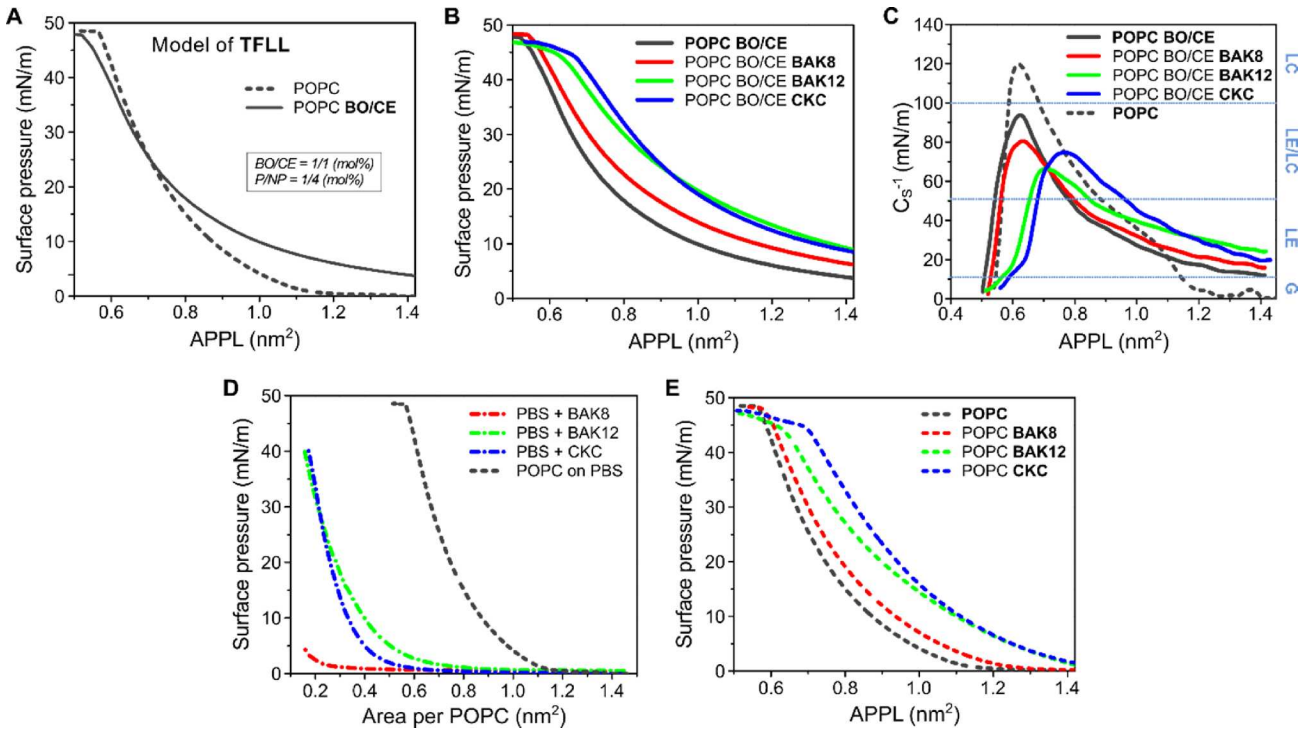

Fig. 2. Surface pressure-molecular area isotherms of TFLL model (solid) and pure POPC monolayer (dashed) (A); surface pressure-molecular area isotherms of TFLL model spread on an aqueous subphase and the aqueous subphase containing $3.6x10^{-7}$ M of BAKs (B); compressibility modulus C_s^{-1} dependence on APPL (C). The isotherms for control systems: BAKs at the water–air interface (D) and BAKs in pure POPC monolayer (E). Surface area per polar lipid (APPL) was used to define the surface area.

(> 0.8 nm^2) and small (< 0.52 nm^2) APPL, while LE/LC coexistence occurs for intermediate APPL. Hence, the TFLL model is relatively elastic even at high packing close to the collapse. On the contrary, in the pure POPC film, prior to the collapse (APPL = ~0.7 nm^2), the transition to a relatively inelastic LC phase is observed.

The influence of BAKs on the TFLL model was investigated by measuring the surface pressure-molecular area isotherms of the TFLL model spread over the aqueous phase containing $3.6x10^{-7}$ M of BAKs in the PBS buffer. Such a BAKs concentration was chosen to mimic the estimated remaining concentration of BAK on the ocular surface following the instillation of one drop of the CKC-containing emulsions. The corresponding isotherms are shown in Fig. 2B.

In all cases, the presence of BAKs in the subphase increases the surface pressure with respect to the systems without BAKs. It means that BAKs incorporate into the TFLL film and enhance the lateral packing at the water–lipid interface. The effect is more pronounced for CKC and BAK12 while less pronounced for BAK8. Regarding the isotherm shape, BAK8 introduces mainly a systematic shift toward higher pressure values. In contrast, CKC and BAK12 isotherms are qualitatively different at high lateral packing with more pronounced deflection points at ~45 mN/m occurring at a slightly lower pressure than in the case of pure TFLL and TFLL with BAK8 (~48 mN/m).

Overall, all BAKs increase lateral packing, while the long-tail CKC and BAK12 have a more substantial effect than the short-tail BAK8.

The influence of BAKs on the mechanical properties of TFLL can be further analyzed by means of lateral compressibility modulus, shown in Fig. 2C. The presence of BAKs influences the values of C_s^{-1}. Namely, at large and moderate APPL (0.7–1.4 nm^2), BAKs increase C_s^{-1}, reducing the liquid character of the film. At the molecular level, it can be rationalized by the presence of additional molecular components at the interface. These effects are minor for BAK8, stronger for BAK12, and significantly pronounced for CKC. On the contrary, for APPL < 0.7 nm^2, BAKs decrease C_s^{-1}, preserving the liquid character of the film at higher packing. Such a decrease of C_s^{-1} can be explained by a tendency of BAK molecules to diminish the formation of LC domains within the LE phase of the film as the film compresses.

To help rationalize the behavior of TFLL in the presence of BAKs, we investigated two control systems. First, we measured isotherms for BAKs at the pure water–air interface, i.e., without a lipid film (Fig. 2D). Second, the isotherms were measured for BAKs interacting with a pure POPC monolayer, i.e., without nonpolar lipids (Fig. 2E). At the pure water–air interface, the presence of BAKs in the subphase leads to an increase of lateral pressure, proving that BAKs are surface active. The activity is the strongest for CKC and BAK12 and significantly weaker for BAK8. It corresponds well to the length of the acyl chain, in agreement with previous experimental results for surfactants [34–36]. Notably, isotherms obtained for CKC and BAK12 are qualitatively similar to those observed for typical surfactants. It shows that CKC and BAK12 at the air–water interface can form monomolecular Langmuir films on their own. On the contrary, the isotherm of BAK8 reaches only low-pressure values (< 5 mN/m), showing that BAK8 molecules alone cannot easily assemble in a monolayer structure. In the second control system, pure POPC monolayer, the isotherms are qualitatively the same as those recorded for the TFLL model (Fig. 2B). These two control experiments show a crucial role of BAKs-polar lipids interactions in TFLL supplemented with BAKs.

Summarizing the Langmuir trough experiments, all BAKs incorporate into the TFLL model, increasing the lateral packing. The long-tail CKC and BAK12 have a more substantial effect than the short-tail BAK8. At the macroscopic level, longer BAKs improve the compressibility of the films at significant compression. The experiments also show that interactions between BAKs and polar lipids are predominantly responsible for the alterations of the film properties.

3.1.2. *Fluorescence microscopy imaging and generalized polarization maps*

We applied two fluorescence techniques to get further insight into the interactions of BAKs with the TFLL model. First, we used widefield imaging to investigate whether the presence of BAKs leads to

macroscopic (within the diffraction-limited optical resolution, i.e., > 200 nm) film restructuring. We employed simultaneously two fluorescent probes to report on the polar lipid layer ("red" DOPE-Atto633) and the nonpolar layer ("blue" Bodipy 493/503). In Fig. 3A-D, widefield fluorescence images of the labeled films under low and high lateral pressure in the pure TFLL model and TFLL + CKC are shown for both fluorescent probes. Small inhomogeneities in both polar and nonpolar lipids (visible as brighter dots) are observed under all lateral pressures; they are inherent to the TFLL model and are not altered by the presence of CKC. We detected similar inhomogeneities in other previously studied polar-nonpolar films; they result from the formation of mixed polar-nonpolar aggregates [25]. Similar results were obtained for BAK8 and BAK12 (images not shown). Hence, with the widefield method, we do not observe changes in the macroscopic structure of TFLL in the presence of BAKs.

The second fluorescence technique used here is generalized polarization (GP) imaging. In contrast to regular widefield imaging, GP allows for investigating sub-diffraction-limited optical resolution (nanometer length scale) alterations of lipid film packing caused by the presence of BAKs. It relies on the solvatochromic fluorescent probe Laurdan with the chromophore residing in the carbonyl region of polar lipids, probing their hydration and mobility. Thanks to this location, Laurdan is highly sensitive to alterations in the lipid film's headgroup and tail region. Since lipid mobility is strongly related to their order, we use GP here as an estimate of the local order of lipid molecules. In Fig. 4A, typical GP images obtained using Laurdan in the TFLL + CKC system are shown. These images are constructed by calculating GP values for each pixel based on the pixel values from the corresponding fluorescence intensity images measured at two different wavelength channels (see Methodology). Small heterogeneities are observed at both lateral pressures shown; they roughly correspond to those detected by the two other dyes (note the different magnifications used in both methods) and are not influenced by the presence of BAKs.

More detailed information can be obtained by analyzing GP values distributions (Fig. 4B-E). Negative values of GP indicate less locally packed (ordered), and positive values indicate more locally packed lipid environment. For all investigated systems (Fig. 4B-E), we observed a shift of GP distributions toward higher values during film compression. It demonstrates that, as expected, lateral compression of each film increases the local lipid packing and enhances local lipid order. However, significant differences depending on BAKs content occur. Namely, the presence of BAK8 (Fig. 4C) leads to lower order than in the pure TFLL model (Fig. 4B). This effect is particularly visible at low lateral pressure where the whole GP distribution of the system with BAK8 is shifted to negative values. On the contrary, the presence of CKC (Fig. 4E) shifts the GP distribution toward higher values than those in the pure TFLL model, and this ordering effect is visible at both low and high lateral pressures. BAK12 (Fig. 4D) also shows an ordering influence on the film, but to a lower extent than CKC.

Summarizing the microscopic data, we observe that the presence of BAKs does not influence small lateral inhomogeneities typically observed in the mixed polar-nonpolar films. On the contrary, BAKs alter the local order of the film. Short-tail BAK8 has a disordering effect, while the longer-tail BAK12 and, in particular, the longest-tail CKC display an ordering effect on the films.

3.2. MD

3.2.1. BAKs in water

Before simulating interactions of BAKs with TFLL, we performed preparatory simulations of the behavior of BAKs in water only. We considered two BAKs concentrations, low (~0.04 M) and high (~0.2 M). We aimed to mimic different conditions that occur in the tear film upon administration of BAKs-containing formulations. Namely, directly upon topical instillation, a local concentration of BAKs in the TFLL vicinity is high, but decreases with time. Note that BAKs are cationic surfactants with relatively low CMC; an experimentally estimated CMC for a mixture of BAKs equals 0.15 mM [37]. Both concentration values used here are above the CMC to facilitate system equilibration in simulations.

First, we simulated BAKs in the bulk of water. We started the simulation with BAKs molecules randomly placed in the simulation box. At the low concentration, surfactant molecules remained mainly in the monomeric or dimeric form. At high concentration, we observed the formation of elongated micelle-like structures; typical snapshots for CKC are shown in Fig. 5A i-iii. Importantly, it was suggested previously, based on experiments, that BAKs can form elongated micelle-like aggregates [38,39]. Here, we directly confirm such behavior. Furthermore, we observed qualitatively the same behavior for BAK8 and BAK12.

Second, we simulated BAKs in the water with a water–air interface present. At low concentration, we observed the transfer of BAKs to the interface and the formation of a film (results not shown here). CKC and BAK12 formed relatively well-packed films, while the shortest BAK8 formed a less-packed film at the interface. At high concentration, the formation of micelle-like structures occurred, accompanied by the transport of BAKs to the interface and formation of BAKs films; the process for CKC is shown in Fig. 5B. This behavior is in order with the

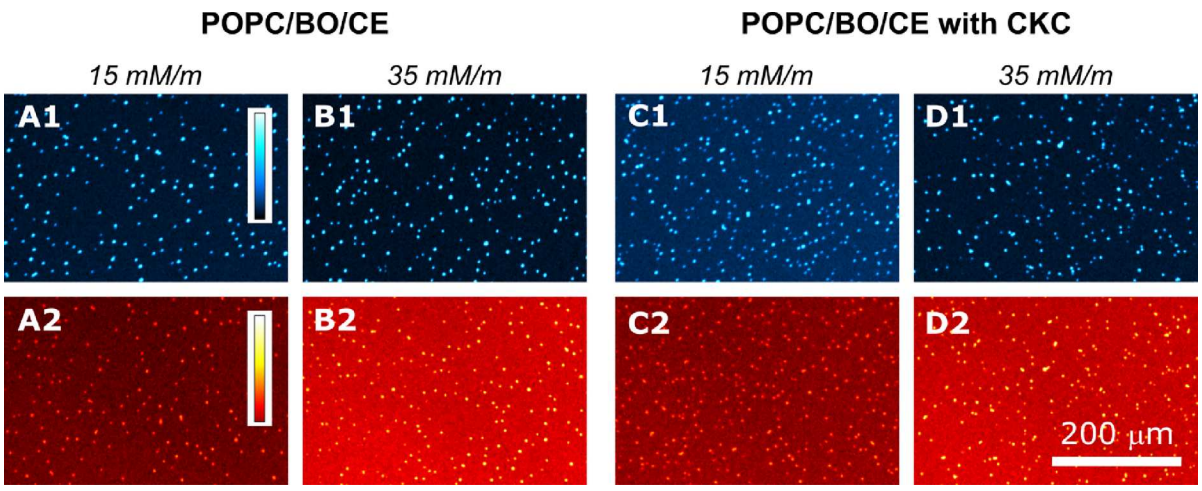

Fig. 3. Widefield fluorescence images (pseudo-color) of the TFLL model and TFLL + CKC collected at surface pressures 15 (A1, A2, C1, C2) and 35 mN/m (B1, B2, D1, D2). The bottom panel ("red"), A2-D2, depicts the polar and top panel ("blue"), A1-D1, nonpolar fluorescence channels. The bars show the fluorescence intensity scale; the range of pixel values is 0–255 ("blue") and 60–255 ("red"). (For interpretation of the references to color in this figure legend, the reader is referred to the web version of this article.)

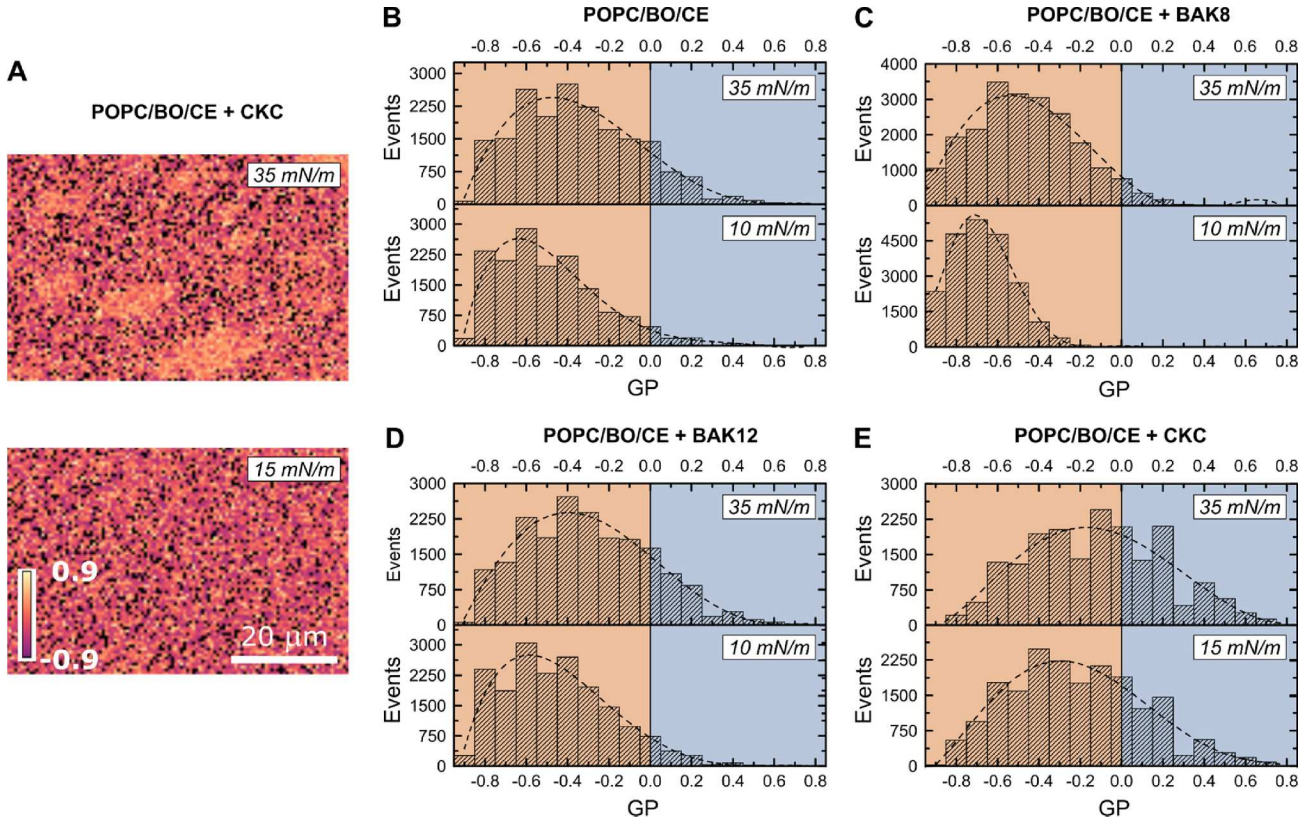

Fig. 4. GP measurements in the TFLL model in the absence and presence of BAKs. GP image (pseudo-color) of POPC/BO/CE + CKC system at 15 and 35 mN/m (A). GP values distributions for four systems: POPC/BO/CE (B), POPC/BO/CE + BAK8 (C), POPC/BO/CE + BAK12 (D), and POPC/BO/CE + CKC (E) at low (10 or 15 mN/m) and high (35 mN/m) surface pressure.

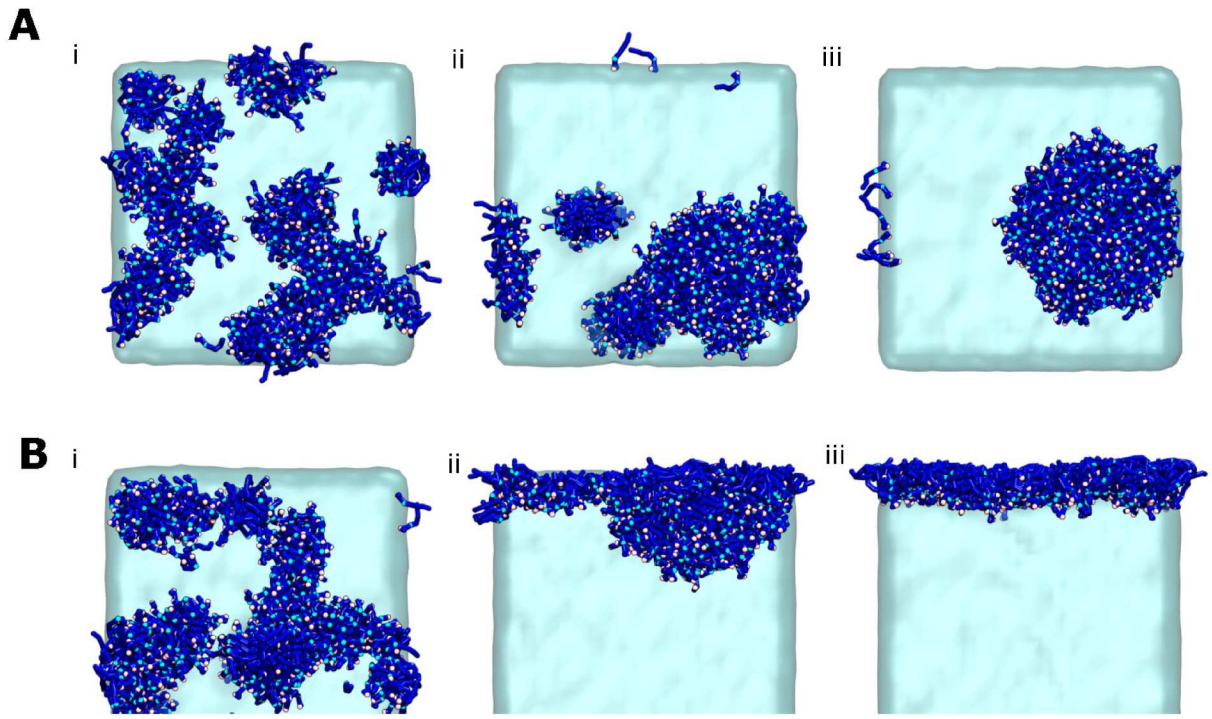

Fig. 5. MD simulations of CKC in the bulk of water (A) and at the water–air interface (B) at high (~0.2 M) concentration. Color coding: turquoise - water, dark blue - CKC, light blue and pink – polar heads of CKC. (For interpretation of the references to color in this figure legend, the reader is referred to the web version of this article.)

surface activity of BAKs observed in our experiments (indicated by the shift of the isotherms in Fig. 2D). It also demonstrates that all considered BAKs have intrinsic surface activity at the water–air interface. Of note, MD simulations provide valuable insight into the structure of the micelle-like aggregates formed by BAKs in water. We observe that BAKs typically form 3D assemblies in which several smaller subunits occur. This is important from the point of view of drug delivery, as BAKs micelles and CKC/oil vesicles are directly used drug vesicles, e.g., in topical eye drops [6,9].

3.2.2. *BAKs in TFLL*

In the next stage, we used MD simulations to investigate molecular-level interactions of BAKs with the TFLL model. We employed the in silico model of TFLL that we previously introduced [22]. In short, the model consists of ~6000 lipid molecules spread at the water–air interface. Lipid composition corresponded to that used in experiments, 1:4 (mol/mol) polar (POPC) to nonpolar (1:1 BO/CE). The lateral packing, quantified by surface area per polar lipid APPL = 0.67 nm^2 was chosen here; such a value mimics the spontaneous pressure that POPC lipids attain in bilayers; it also corresponds to the relatively highly-packed LC phase of POPC monolayer (see the experimental isotherm in Fig. 2A). Under such conditions, the model mimics a ~20 x 20 nm^2 patch of TFLL. Similar conditions regarding the lateral film packing were employed in our previous TFLL model studies [18,22].

The model lipid film has a multilayer structure at the water–air interface, with a monolayer of polar lipids and a thick layer of nonpolar lipids (see the density profile in Fig. 7A), as described previously [22]. Similarly to the simulations of BAKs in water, here we also considered BAKs at low (~0.02 M) and high (~0.15 M) concentrations. In this way, we mimic two distinctive modes that likely occur in tear film after topical instillation of BAK-containing drug formulations. The high concentration mode corresponds to a situation directly after installation when local concentration of BAKs in the actual film is high. The low concentration mimics the situation occurring in later phases after instillation, when the formulation components are spread in the film, mixed by blinking, and partially removed from the film by adsorption to the mucin layer and outflow via the nasolacrimal duct.

At low concentration, to speed up equilibration, we pre-prepared a simulation system with BAKs already incorporated in the polar layer and simulated it. In this case, we observed that BAKs were stably integrated into the polar layer of POPC for the whole simulation time. For CKC, a typical snapshot of the equilibrated system is shown in Fig. 6A, and its structure is quantified by density profiles presented in Fig. 7B. A stable localization of CKC in the polar region occupied by POPC is clearly visible. CKC molecules orient their polar heads toward the water and nonpolar tails toward the nonpolar interior of the TFLL film. A comparison with the density profiles of pure TFLL (Fig. 7A) shows that the presence of low-concentration CKC does not visibly change the structure of TFLL. Qualitatively the same results were obtained for BAK8 and BAK12. However, for the shorter BAKs, we observed a somewhat less ordered orientation in the POPC layer. It can be quantified by tilt angle values presented in Fig. 7D. The distribution of the tilt angles demonstrates that the long CKC chains attain in-parallel orientation to the chains of POPC. With the shortening of the BAKs' chain, the average orientation is broader, corresponding to lower-order and reorientation of the incorporated tails. We observed such behavior also in previously studied computational models in TFLL [17]. The different orientation of BAK tails in the polar lipid layer is in line with the experimentally observed influence of BAKs on the TFLL model. Namely, long-tails of CKC, by orienting in parallel to POPC, significantly increase lateral pressure and diminish water content in the lipid film. On the other hand, short-tail BAK8 molecules also locate between POPC molecules, leading to somewhat increased lateral pressure. However, their tails stay relatively flexible, enabling water penetration and the formation of water defects in the polar layer of TFLL. BAK12 behaves in an intermediate fashion between CKC and BAK8.

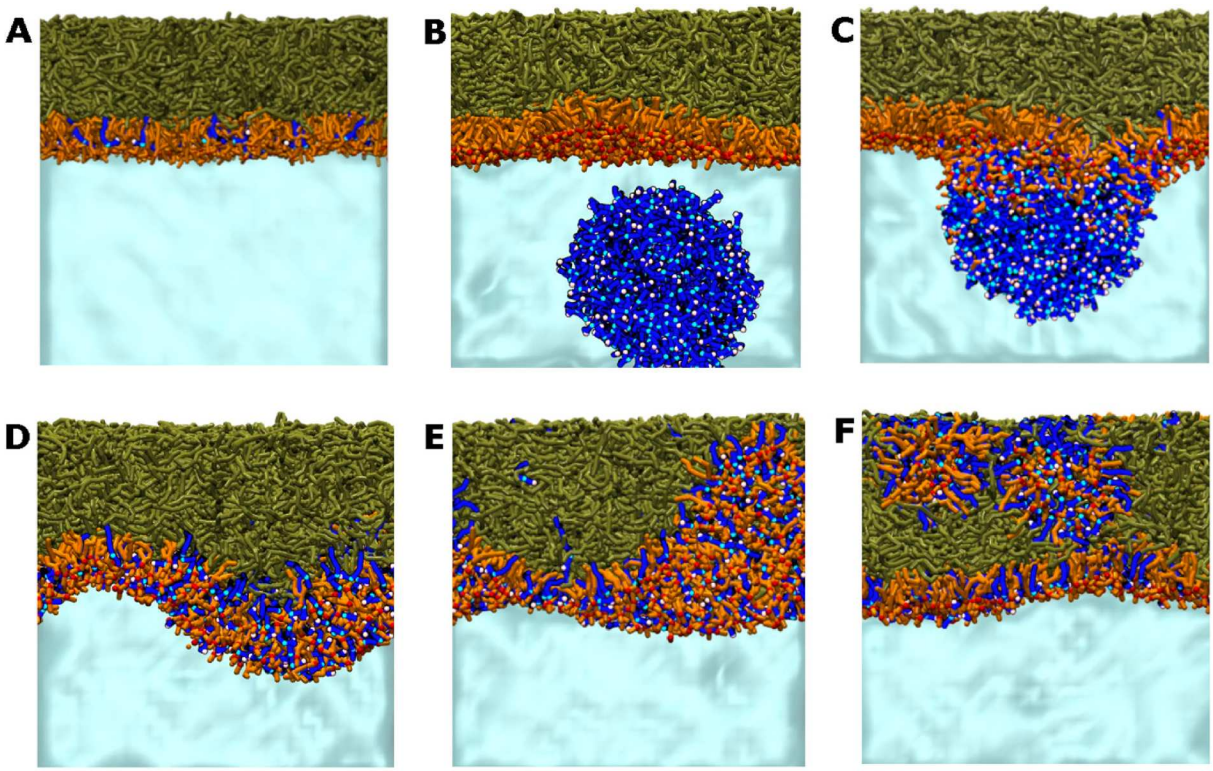

Fig. 6. MD simulations of CKC at low (~0.02 M) (A) and high (~0.15 M) (B-F) concentrations interacting with the TFLL model. Color coding: turquoise - water, dark blue - CKC, light blue and pink – polar heads of CKC, orange - POPC lipid tails, red – polar heads of POPC, olive - BO and CE molecules. (For interpretation of the references to color in this figure legend, the reader is referred to the web version of this article.)

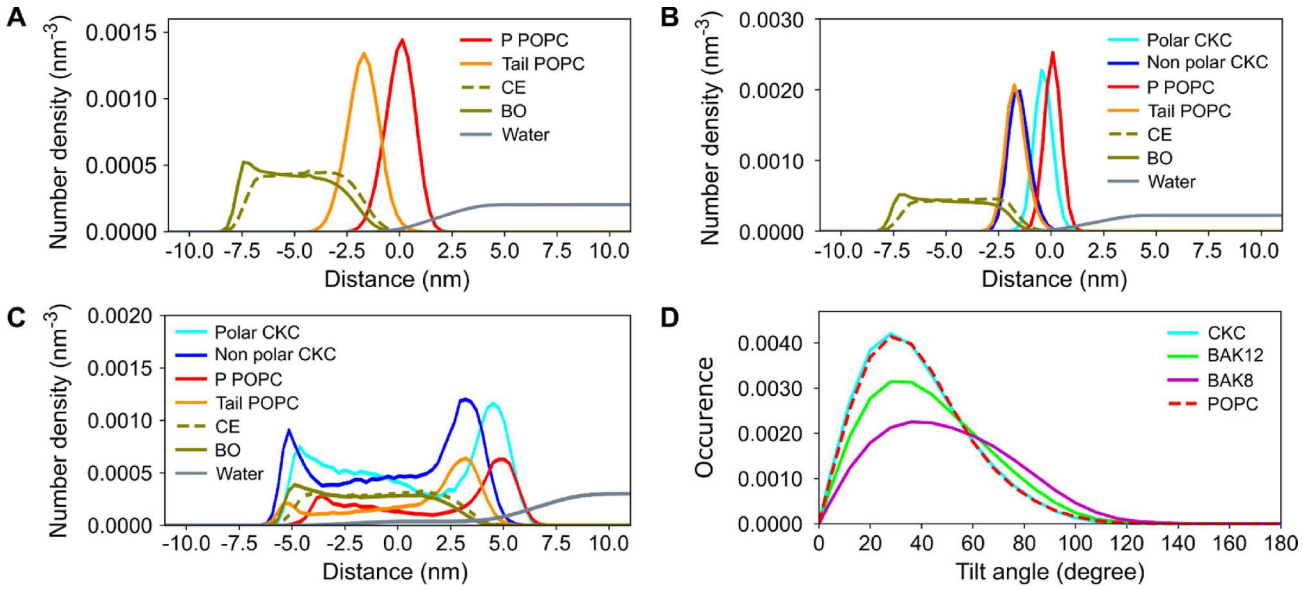

Fig. 7. Density profiles of TFLL (A), CKC molecules incorporated in the TFLL at low (B) and high (C) concentration and tilt angles of the three BAKs species (D).

For MD simulations at high BAKs concentration, the BAK micelle-like structures (taken from the preparatory simulations in the aqueous phase, Fig. 5A i-iii) were initially placed in the aqueous phase of the TFLL model.

In the course of simulations, BAK aggregates diffused, adsorbed, and then transferred to the polar POPC layer. Next, they caused a significant restructuring of the polar layer. Namely, as the packing of the material was above the collapse packing, a collapse-like behavior with the transport of BAKs and POPC to the nonpolar layer, accompanied by some water molecules occurred, forming eventually elongated inverse micelle-like structures. Furthermore, some of the BAK molecules were able to go to the outer (lipid-air) interface and create a film there. This multi-stage process is illustrated for CKC in a series of snapshots in Fig. 6B-F. The film restructuring is quantified by density profiles (Fig. 7C). It should be noted that the observed transfer and accumulation of polar lipid assemblies containing BAKs to the nonpolar layer of TFLL may play an essential role after topical drop instillation. Namely, it can lead to the accumulation of the drug components in the nonpolar lipid phase that is relatively stable in the tear film and undergoes only slow removal. Note that, half-life of the TFLL is close to 8–9 h, while the half-life of the aqueous phase is in the range of minutes [40]. The TFLL is relatively stable and its slow removal is mainly via its spreading onto the lids and eyelashes [41]. At the same time, it cannot be excluded that some of TFLL lipids, when expelled upon blinking from the interface, can form dispersed lipid micelles in the aqueous phase of the TF which then follow the same elimination route as the water-soluble components.

In summary, MD simulations show that at low concentrations, BAKs incorporate in the polar layer of TFLL. Long-tail BAKs incorporate between polar lipids, are relatively ordered, and increase lateral packing. Short-tail BAK molecules also integrate into the polar layer, but their tails are relatively flexible, leading to water penetration. It is in accord with the experimental observations. At high concentrations, BAKs form lipid aggregates that, to a certain extent, disorganize the TFLL and lead to the transfer and accumulation of polar lipids together with BAKs in the nonpolar layer of TFLL.

4. Conclusions

We investigated the influence of BAKs, the surfactants commonly used in topical ophthalmologic formulations, on the models of TFLL. The experiments employing synthetic mixed polar-nonpolar lipid films spread on the aqueous subphase containing BAKs show that the surfactants interact with the TFLL model by incorporating into it and, consequently, increasing the lateral packing. The influence depends on the tail length; the long-tail CKC and BAK12 have a substantial effect, while the shorter BAKs have a weaker effect. Long BAKs also enhance film compressibility at higher packing. Furthermore, the experiments show that interactions between BAKs and polar lipids are predominantly responsible for the alterations of the film properties. Microscopy imaging demonstrates that the presence of BAKs does not influence small lateral inhomogeneities typically observed in the mixed polar-nonpolar films. However, BAKs alter the local order of the film. In particular, the long-tail CKC orders the lipids in TFLL, while the short-tail BAK8 has a disordering effect.

By using MD simulations, we showed that BAKs above CMC form micelle-like 3D aggregates in water. In some cases, we observed that these aggregates were composed of smaller repeatable units. Determination of an exact structure of such 3D assemblies would be an interesting topic, particularly in cases where BAKs micelles containing drugs are directly used for ophthalmologic drug delivery.

By employing MD simulations, we showed that two modes of BAKs-TFLL interactions could be identified. At low BAKs concentration, which mimics the later stage after topical drug instillation, BAKs incorporate in the polar layer of TFLL. Long-tail BAKs incorporate between polar lipids, they are relatively ordered and increase lateral packing. Short-tail BAK molecules also integrate into the polar layer, but their tails are relatively flexible, leading to water penetration. It is in accord with the experimental observations. At high concentrations, mimicking BAKs-TFLL interactions directly after instillation, BAKs form lipid aggregates that, to a certain extent, disorganize the TFLL and lead to the transfer and accumulation of polar lipids together with BAKs in the nonpolar layer of TFLL.

In summary, the results discussed here suggest that the presence of BAKs alters TFLL. Short-tail BAKs, represented here by BAK8, disorganize the film, decreasing its compressibility and leading to high water penetration to the film. On the other hand, long-tail BAKs, particularly CKC, stabilize the film by increasing its lateral packing and enhancing both macro- and nanoscale lipids order. The simulations also shed light on the film arrangement directly after the instillation of BAKs when a local concentration of the surfactant is high. Namely, under such conditions, BAKs form aggregates with polar lipids of TFLL, which then can accumulate in the nonpolar fraction of the film. We can speculate that if BAKs are then accompanied by an active drug, such behavior may lead to the accumulation of the drug in the relatively stable nonpolar lipid

phase leading to prolonged presentation and a slow release of a drug from TFLL to the aqueous subphase.

Declaration of Competing Interest

The authors declare the following financial interests/personal relationships which may be considered as potential competing interests: L. C. has consulted Santen SAS.; P.D and J.-S. G are employed by Santen SAS. The authors have no other conflicts of interest that are directly relevant to the content of this manuscript, which remains their sole responsibility.

Data availability

Data will be made available on request.

Acknowledgements

This work was supported by the Czech Science Foundation (grant no. 21-19854S).

Appendix A. Supplementary data

Supplementary data to this article can be found online at https://doi.org/10.1016/j.ejpb.2023.03.007.

References

[1] R.D. Fechtner, D.G. Godfrey, D. Budenz, J.A. Stewart, W.C. Stewart, M.C. Jasek, Prevalence of ocular surface complaints in patients with glaucoma using topical intraocular pressure-lowering medications, Cornea 29 (2010) 618–621.
[2] F. Fineide, N. Lagali, M.Y. Adil, R. Arita, M. Kolko, J. Vehof, T.P. Utheim, Topical glaucoma medications–Clinical implications for the ocular surface, Ocul. Surf. 26 (2022) 19–49.
[3] C. Baudouin, A. Labbé, H. Liang, A. Pauly, F. Brignole-Baudouin, Preservatives in eyedrops: the good, the bad and the ugly, Prog. Retin. Eye Res. 29 (2010) 312–334.
[4] X. Zhou, X. Zhang, D. Zhou, X. Duan, A narrative review of ocular surface disease related to anti-glaucomatous medications, Ophthalmol. Ther. 54 (2022) 1–24.
[5] L. D'andrea, M. Montemagni, G. Celenza, R. Iorio, C. Costagliola, Is it time for a moratorium on the use of benzalkonium chloride in eyedrops? Brit. J. Clin. Pharmacol. 88 (2022) 3947–3949.
[6] P. Daull, F. Lallemand, J.-S. Garrigue, Benefits of cetalkonium chloride cationic oil-in-water nanoemulsions for topical ophthalmic drug delivery, J. Pharm. Pharmacol. 66 (2014) 531–541.
[7] P. Furrer, J.M. Mayer, R. Gurny, Ocular tolerance of preservatives and alternatives, Eur. J. Pharm. Biopharm. 53 (2002) 263–280.
[8] T. Farías, L.-C. de Ménorval, J. Zajac, A. Rivera, Solubilization of drugs by cationic surfactants micelles: Conductivity and 1H NMR experiments, Colloids Surf. A Physicochem. Eng. Asp. 345 (2009) 51–57.
[9] F. Lallemand, P. Daull, S. Benita, R. Buggage, J.-S. Garrigue, Successfully improving ocular drug delivery using the cationic nanoemulsion, novasorb, J. Drug Deliv. 2012 (2012), 604204.
[10] P.-Y. Robert, B. Cochener, M. Amrane, D. Ismail, J.-S. Garrigue, P.-J. Pisella, C. Baudouin, Efficacy and safety of a cationic emulsion in the treatment of moderate to severe dry eye disease: a randomized controlled study, Eur. J. Ophthalmol. 26 (2016) 546–555.
[11] A. Leonardi, E.M. Messmer, M. Labetoulle, M. Amrane, J.-S. Garrigue, D. Ismail, M. Sainz-de-la-Maza, F.C. Figueiredo, C. Baudouin, Efficacy and safety of 0.1% ciclosporin A cationic emulsion in dry eye disease: a pooled analysis of two double-masked, randomised, vehicle-controlled phase III clinical studies, Brit. J. Ophthalmol. 103 (2019) 125–131.
[12] C. Baudouin, F.C. Figueiredo, E.M. Messmer, D. Ismail, M. Amrane, J.-S. Garrigue, S. Bonini, A. Leonardi, A randomized study of the efficacy and safety of 0.1% cyclosporine A cationic emulsion in treatment of moderate to severe dry eye, Eur. J. Ophthalmol. 27 (2017) 520–530.
[13] M. Amrane, C. Creuzot-Garcher, P.-Y. Robert, D. Ismail, J.-S. Garrigue, P.-J. Pisella, C. Baudouin, Ocular tolerability and efficacy of a cationic emulsion in patients with mild to moderate dry eye disease–A randomised comparative study, J. Fr. Ophtalmol. 37 (2014) 589–598.
[14] R. Deshmukh, D.S.J. Ting, A. Elsahn, I. Mohammed, D.G. Said, H.S. Dua, Real-world experience of using ciclosporin-A 0.1% in the management of ocular surface inflammatory diseases, Br. J. Ophthalmol. 106 (2022) 1087–1092.
[15] P. Daull, M. Amrane, D. Ismail, G. Georgiev, L. Cwiklik, C. Baudouin, A. Leonardi, G. Garhofer, J.-S. Garrigue, Cationic emulsion-based artificial tears as a mimic of functional healthy tear film for restoration of ocular surface homeostasis in dry eye disease, J. Ocul. Pharmacol. Ther. 36 (2020) 355–365.
[16] P. Daull, S. Guenin, V.H. De Almeida, J.-S. Garrigue, Anti-inflammatory activity of CKC-containing cationic emulsion eye drop vehicles, Mol. Vis. 24 (2018) 459–470.
[17] K. Riedlova, A. Melcrova, A. Olżyńska, P. Daull, J.-S. Garrigue, L. Cwiklik, Influence of benzalkonium chloride on tear film lipid layer stability: a molecular level view by employing in silico modeling, MAIO 2 (2019) 36–42.
[18] P. Eftimov, A. Olżyńska, A. Melcrová, G.A. Georgiev, P. Daull, J.-S. Garrigue, L. Cwiklik, Improving stability of tear film lipid layer via concerted action of two drug molecules: A biophysical view, Int. J. Mol. Sci. 21 (2020) 9490.
[19] A. Patel, K. Cholkar, V. Agrahari, A.K. Mitra, Ocular drug delivery systems: An overview, World J. Pharmacol. 2 (2013) 47.
[20] S. Reimondez-Troitiño, N. Csaba, M. Alonso, M. De La Fuente, Nanotherapies for the treatment of ocular diseases, Eur. J. Pharm. Biopharm. 95 (2015) 279–293.
[21] N. Efron, G. Young, N.A. Brennan, Ocular surface temperature, Curr. Eye Res. 8 (1989) 901–906.
[22] A. Wizert, D.R. Iskander, L. Cwiklik, Organization of lipids in the tear film: a molecular-level view, PLOS ONE 9 (2014) e92461.
[23] A. Olżyńska, P. Delcroix, T. Dolejšová, K. Krzaczek, B. Korchowiec, A. Czogalla, L. Cwiklik, Properties of lipid models of lung surfactant containing cholesterol and oxidized lipids: A mixed experimental and computational study, Langmuir 36 (2020) 1023–1033.
[24] A. Bunker, T. Rog, Mechanistic understanding from molecular dynamics simulation in pharmaceutical research 1: Drug delivery, Front. Mol. Biosci. 7 (2020), 604770.
[25] A. Olżyńska, A. Wizert, M. Štefl, D.R. Iskander, L. Cwiklik, Mixed polar-nonpolar lipid films as minimalistic models of tear film lipid layer: A langmuir trough and fluorescence microscopy study, Biochim. Biophys. Acta-Biomembr. 1862 (2020) 183300.
[26] S.H. Brown, C.M. Kunnen, E.B. Papas, P.L. de la Jara, M.D. Willcox, S.J. Blanksby, T.W. Mitchell, Intersubject and interday variability in human tear and meibum lipidomes: a pilot study, Ocul. Surf. 14 (2016) 43–48.
[27] T. Viitaja, J.-E. Raitanen, A. Hynynen, J. Moilanen, K. Svedström, R.O. Paananen, F.S. Ekholm, On the importance of chain branching in tear film lipid layer wax and cholesteryl esters, Colloids Surf. B Biointerfaces 214 (2022), 112429.
[28] S.J. Marrink, H.J. Risselada, S. Yefimov, D.P. Tieleman, A.H. De Vries, The MARTINI force field: coarse grained model for biomolecular simulations, J. Phys. Chem. B 111 (2007) 7812–7824.
[29] L. Cwiklik, Tear film lipid layer: A molecular level view, Biochim. Biophys. Acta-Biomembr. 2016 (1858) 2421–2430.
[30] M.J. Abraham, T. Murtola, R. Schulz, S. Páll, J.C. Smith, B. Hess, E. Lindahl, GROMACS: High performance molecular simulations through multi-level parallelism from laptops to supercomputers, Softwarex 1 (2015) 19–25.
[31] W. Humphrey, A. Dalke, K. Schulten, VMD: visual molecular dynamics, J. Mol. Graphics 14 (1996) 33–38.
[32] J.D. Hunter, Matplotlib: A 2D graphics environment, Comput. Sci. Eng. 9 (2007) 90–95.
[33] J.T. Davies, E.K. Rideal, Interfacial Phenomena, 2nd ed., Academic Press, New York, 1963, pp. 265–289.
[34] H. Ngyugen, C.E. McNamee, Determination and comparison of how the chain number and chain length of a lipid affects its interactions with a phospholipid at an air/water interface, J. Phys. Chem. B 118 (2014) 5901–5912.
[35] H. Shayesteh, F. Raji, A.R. Kelishami, Influence of the alkyl chain length of surfactant on adsorption process: a case study, Surf. Interfaces 22 (2021), 100806.
[36] S. Kalam, S.A. Abu-Khamsin, M.S. Kamal, S. Patil, Surfactant adsorption isotherms: a review, ACS Omega 6 (2021) 32342–32348.
[37] G.N. Mathioudakis, A. Soto Beobide, G. Bokias, P.G. Koutsoukos, G.A. Voyiatzis, Surface-enhanced Raman scattering as a tool to study cationic surfactants exhibiting low critical micelle concentration, J. Raman Spectrosc. 51 (2020) 452–460.
[38] M. Törnblom, U. Henriksson, Effect of solubilization of aliphatic hydrocarbons on size and shape of rodlike C16TABr micelles studied by 2H NMR relaxation, J. Phys. Chem. B 101 (1997) 6028–6035.
[39] Y. Zhu, M.L. Free, Evaluation of ion effects on surfactant aggregation from improved molecular thermodynamic modeling, Ind. Eng. Chem. Res. 54 (2015) 9052–9056.
[40] H. Mochizuki, M. Yamada, S. Hatou, K. Tsubota, Turnover rate of tear-film lipid layer determined by fluorophotometry, Br. J. Ophthalmol. 93 (2009) 1535–1538.
[41] S. Khanal, T.J. Millar, Nanoscale phase dynamics of the normal tear film, Nanomed.: Nanotechnol. Biol. Med. 6 (2010) 707–713.

4 Supporting information of Publication II

Supporting Information

Influence of BAKs on Tear Film Lipid Layer:

in vitro and in silico models

Kamila Riedlová,[1, 2] Maria Chiara Saija,[1, 2] Agnieszka Olżyńska,[1] Piotr Jurkiewicz,[1] Philippe Daul,[3] Jean-Sebastien Garrigue,[3] and Lukasz Cwiklik[1*]

[1]J. Heyrovský Institute of Physical Chemistry, Czech Academy of Sciences, Dolejškova 3, 18223 Prague, Czech Republic

[2]Department of Physical and Macromolecular Chemistry, Faculty of Science, Charles University, Hlavova 8, 12800, Prague, Czech Republic

[3]SANTEN SAS, Novagali Innovation Center, 1, rue Pierre Fontaine, Bâtiment Genavenir IV, CEDEX, F-91458 Evry, France

[*] corresponding author: lukasz.cwiklik@jh-inst.cas.cz

1. Composition of simulated systems

Table 1. Composition of the systems in MD simulations. Chloride anions were used as counterions to neutralize the charge of BAKs. Note that each MARTINI water bead represents four water molecules. If present, lipids were split symmetrically between the two water-air interfaces present in the simulation box.

System	approximate BAK concentration (mmol)	# BAK8 (BAK12, CKC)	# MARTINI water beads	# POPC	# CE	# BO
Bulk 1	20	80	49272	-	-	-
Bulk 2	40	160	49272	-	-	-
Bulk 3	200	728	49272	-	-	-
Air-water 1	20	80	49272	-	-	-
Air-water 2	40	160	49272	-	-	-
Air-water 3	200	728	49272	-	-	-
TFLL low conc.	40	292	89706	2×581	2×1250	2×1250
TFLL high conc.	150	728	66387	2×727	2×1250	2×1250

2. Force field parameters and computational details of MD simulations.

MARTINI 2.2. force field was used for accounting for molecular interactions [1, 2]. Additional in-house MARTINI-type force field parameters were developed for BAKs used in this study (not available in the standard MARTINI library), and are can be accessed online at:

https://zenodo.org/deposit/7515840

MD simulations were performed using GROMACS (ver. 2016.1) software package [3]. Non-bonded interactions were calculated employing the cutoff distance of 1.1 nm with the potential-shift Verlet method. The reaction-field algorithm with the relative electrostatic

screening parameter of 15 was used for accounting for long-range electrostatic interactions. MD trajectories were calculated with 10 fs time step for integration of the Newton equations of motions. Periodic boundary conditions were used for the simulation boxes, with the NVT ensemble. Average temperature of 310 K was maintained by the v-rescale algorithm [4]. The LINCS algorithm was used to keep the bond length constant in MARTINI molecules [5]. Periodic boundary conditions (PBC) were used for all systems and the box size was fixed.

References

[1] S.J. Marrink, H.J. Risselada, S. Yefimov, D.P. Tieleman, A.H. De Vries, The MARTINI force field: coarse grained model for biomolecular simulations, J. Phys. Chem. B 111 (2007) 7812-7824.

[2] X. Periole, S.-J. Marrink, The Martini coarse-grained force field, Biomol. Simul. (2013) 533-565.

[3] M.J. Abraham, T. Murtola, R. Schulz, S. Páll, J.C. Smith, B. Hess, E. Lindahl, GROMACS: High performance molecular simulations through multi-level parallelism from laptops to supercomputers, Softwarex 1 (2015) 19-25.

[4] G. Bussi, D. Donadio, M. Parrinello, Canonical sampling through velocity rescaling, J. Chem. Phys. 126 (2007) 014101.

[5] B. Hess, H. Bekker, H.J. Berendsen, J.G. Fraaije, LINCS: a linear constraint solver for molecular simulations, J. Comput. Chem. 18 (1997) 1463-1472.

5 Publication III: The potential role of SP-G as surface tension regulator in tear film: From molecular simulations to experimental observations

International Journal of
Molecular Sciences

MDPI

Article

The Potential Role of SP-G as Surface Tension Regulator in Tear Film: From Molecular Simulations to Experimental Observations

Martin Schicht [1,*,†], Kamila Riedlová [2,3,†,‡], Mercedes Kukulka [2,4], Wenyue Li [1,‡], Aurelius Scheer [1], Fabian Garreis [1], Christina Jacobi [5], Friedrich Paulsen [1], Lukasz Cwiklik [2,†] and Lars Bräuer [1,†]

1 Institute of Functional and Clinical Anatomy, Friedrich-Alexander-Universität Erlangen- Nuremberg, Universitätsstr. 19, 91054 Erlangen, Germany; wenyue.li@fau.de (W.L.); aurelius.scheer@fau.de (A.S.); fabian.garreis@fau.de (F.G.); friedrich.paulsen@fau.de (F.P.); lars.braeuer@fau.de (L.B.)
2 J. Heyrovský Institute of Physical Chemistry, Czech Academy of Sciences, 182 00 Prague, Czech Republic; kamila.riedlova@jh-inst.cas.cz (K.R.); mercedes.kukulka@uj.edu.pl (M.K.); lukasz.cwiklik@jh-inst.cas.cz (L.C.)
3 Department of Physical and Macromolecular Chemistry, Faculty of Science, Charles University, 128 40 Prague, Czech Republic
4 Faculty of Chemistry, Jagiellonian University, 30387 Krakow, Poland
5 Ophthalmology Private Practice, 17, 81034 Nuremberg, Germany; jacobi2001@gmx.de
* Correspondence: martin.schicht@fau.de
† These authors contributed equally to this work.
‡ The present work was performed in fulfilment of the requirements of obtaining the degree Dr. med. dent (W.L.) and PhD (K.R.).

check for updates

Citation: Schicht, M.; Riedlová, K.; Kukulka, M.; Li, W.; Scheer, A.; Garreis, F.; Jacobi, C.; Paulsen, F.; Cwiklik, L.; Bräuer, L. The Potential Role of SP-G as Surface Tension Regulator in Tear Film: From Molecular Simulations to Experimental Observations. *Int. J. Mol. Sci.* **2022**, *23*, 5783. https://doi.org/10.3390/ijms23105783

Academic Editors: Murat Dogru and Alexander V. Ljubimov

Received: 6 April 2022
Accepted: 18 May 2022
Published: 21 May 2022

Publisher's Note: MDPI stays neutral with regard to jurisdictional claims in published maps and institutional affiliations.

Copyright: © 2022 by the authors. Licensee MDPI, Basel, Switzerland. This article is an open access article distributed under the terms and conditions of the Creative Commons Attribution (CC BY) license (https://creativecommons.org/licenses/by/4.0/).

Abstract: The ocular surface is in constant interaction with the environment and with numerous pathogens. Therefore, complex mechanisms such as a stable tear film and local immune defense mechanisms are required to protect the eye. This study describes the detection, characterization, and putative role of surfactant protein G (SP-G/SFTA2) with respect to wound healing and surface activity. Bioinformatic, biochemical, and immunological methods were combined to elucidate the role of SP-G in tear film. The results show the presence of SP-G in ocular surface tissues and tear film (TF). Increased expression of SP-G was demonstrated in TF of patients with dry eye disease (DED). Addition of recombinant SP-G in combination with lipids led to an accelerated wound healing of human corneal cells as well as to a reduction of TF surface tension. Molecular modeling of TF suggest that SP-G may regulate tear film surface tension and improve its stability through specific interactions with lipids components of the tear film. In conclusion, SP-G is an ocular surface protein with putative wound healing properties that can also reduce the surface tension of the tear film.

Keywords: tear film; surfactant protein; surface tension; ocular surface; dry eye

1. Introduction

Dry eye disease (DED, keratoconjunctivitis sicca) is a global problem, afflicting 15% to 20% of the human population in Central Europe, at least 344 million people worldwide, and is one of the most frequent causes of patient visits to eye care practitioners [1–3]. Exogenous influences (e.g., contact lenses, air, drugs, and diet) and endogenous factors (e.g., age, hormonal imbalances, and diabetes mellitus) are the main causes of this disease. DED is based upon a discontinuity of the normal tear film [3,4] characterized by cardinal symptoms such as burning, itchy and watery eyes, painful eye pressure, oppressive feelings, foreign body sensations, and light sensitivity. In most cases, DED is the result of a diminished outer lipid layer at the surface of the tear film [5], a condition called evaporative DED. A quantitative deficit of tears, on the other hand, is considered to be somewhat less common. Meibomian gland dysfunction (MGD) is the leading cause of evaporative DED, which

affects countless people worldwide (e.g., more than 40 million in the United States alone) and is one of the most common causes of patient visits in ophthalmology [6].

The meibomian glands (MGs) are important in preventing evaporation and premature disintegration of the tear film. The secretory lipid component of the tear film is mainly derived from the MGs and forms a superficial layer under physiological conditions [5,7,8]. MG lipids and proteins functionally serve to form a clear optical surface, are antimicrobial (act as an effective barrier against noxae and colonization by microorganisms), stabilize the tear film, and reduce its evaporation [7,9]. Some of the MG lipids reduce the surface tension of the tear film, thus ensuring a stable optical interface [8].

During the last years, it has been shown that the surfactant proteins (SP)-A, -B, -C, and -D, which are well known from the lung studies, regulate surface activity in the alveoli and have immunological properties with respect to both innate and adaptive immunity, are not only present in the lung but also play a role at many sites in the human body [10–14], including the ocular surface [15–17]. In addition to the well-known surfactant proteins (SP)-A, -B, -C, and -D, two additional surfactant proteins have recently been described by us: SP-G and SP-H. They are also produced by tissues of the ocular surface, among others [13,18]. However, little is known about the functions of SP-G in particular.

The first publication by Mittal et al. shows that SP-G is a secretory protein of lung cells, and their preliminary data raise speculation about its regulatory role in the immune response [19]. SP-G is located on human chromosome 6, a susceptibility locus for diffuse panbronchiolitis [20]. The sequence length suggests that SP-G belongs to the SP group of small and hydrophobic proteins (SP-B, SP-C, and SP-H), but it does not share domains with members of this group and the sequence identities are very low (about 10%) [21]. In earlier studies, we have been able to demonstrate by means of molecular dynamics simulations that SP-G can interact with a lipid system after post-translational modifications due to its hydrophobic properties [21]. SP-G has also been shown to be similar to SP-B and SP-C in its physicochemical properties [13].

The aim of the present studies was to find out whether SP-G is a regular component of the human ocular surface, the lacrimal apparatus, MGs and tears in particular, and whether it plays a role in the context of dry eye disease (DED). In addition to molecular biology and immunohistochemistry studies, we performed molecular dynamics simulations of the tear film to investigate the interaction of SP-G with the lipid component of tears and to uncover a possible mechanism of tear film stabilization at the molecular level. In doing so, the insights gained during the modeling and simulation process support and enhance our cell culture experimental studies.

2. Results

2.1. Detection of SP-G in Tissue of the Ocular Surface, Lacrimal Apparatus and in Tears

Tissues of ocular surface and lacrimal system (lacrimal gland, eyelid, conjunctiva, and cornea) as well as cells (human corneal epithelial cells (HCE) and human conjunctival epithelial cells (HCjE)) revealed amplification of SP-G mRNA (Figure 1A), which was in accordance with Genebank (https://www.ncbi.nlm.nih.gov/genbank/ (accessed on 17 May 2022), NM_205854). Western blot analysis with proteins derived from different tear fluid samples showed distinct and SP-G specific protein bands at 15 kDa, Bronchoalveolar lavage served as a positive control and revealed the already described bands at 15 and 28 kDa (Figure 1B).

2.2. Localization of SP-G within the Tissue of the Ocular Surface and in Cultured HCE and HCjE Cells

SP-G was detected in lacrimal- and meibomian gland, corneal, and conjunctival epithelium as well as in the eyelid (Figure 2) by fluorescence (green, left column) and aminoethylcarbazole (AEC) substrate staining (red, right column). Green and red staining represented a positive antibody response of SP-G in all samples. Paraffin-embedded tissue sections of the ocular system (lacrimal gland, eyelid, conjunctiva, and cornea), 5–7 µm in

size, were analyzed. Only samples incubated with primary and secondary antibodies only were negative and showed no staining. The insets in the figure show higher magnification of the tissue used. In the lacrimal gland, cells of the tubular system and, to a minor extent, the acinar cells, showed the presence of SP-G (Figure 2(Aa,Ab)). The lining epithelium of the eyelid showed visible strong SP-G reactivity in the basal epithelial cell layer and faint reactivity within the other layers of the epidermis; strong reactivity was visible on the apical surface of the lining cells (Figure 2(Ac,Ad)). In the conjunctiva, epithelial cells of the healthy conjunctiva showed weak reaction (asterisks) with the SP-G antibody (Figure 2(Ae,Af)). In the meibomian glands, meibocytes were SP-G positive, as well as the lining cells of the excretory duct system. In particular, meibocytes at different stages of maturation showed marked reactivity (Figure 2(Ag,Ah)). In the cornea, SP-G reactivity could be detected in the cytoplasm of basal and apical epithelial cells (Figure 2(Ai,Aj)). Endothelial cells also showed marked reactivity against the SP-G antibody (Figure 2(Ak,Al)). Immunocytochemical studies of corneal (HCE) and conjunctival (HCjE) epithelial cells demonstrated that SP-G is distributed in the cytoplasm and perinuclear region, especially as granula (Figure 2B).

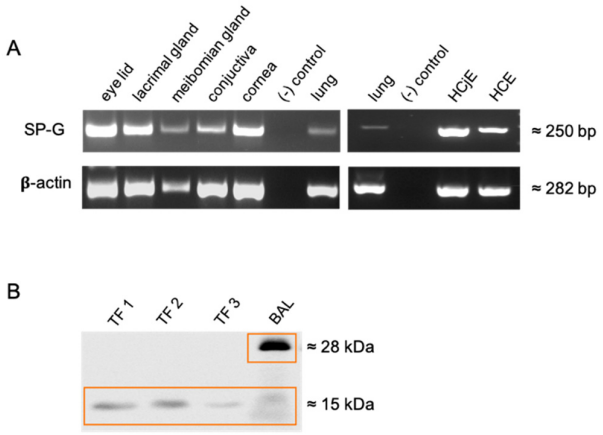

Figure 1. (**A**) Detection of SP-G mRNA in the following samples: lacrimal gland, meibomian gland, eyelid, conjunctiva, cornea, human corneal epithelial cells (HCE), human conjunctival epithelial cells (HCjE). Samples without cDNA were used as negative controls, whereas samples containing lung cDNA were used as positive controls. (**B**) Western blot analysis with a polyclonal anti-rabbit SP-G antibody incubated on tear film (TF) (TF 1–3) and bronchoalveolar lavage (BAL) as positive control.

2.3. Quantification of SP-G in Tears by ELISA and Determination of Tear Surface Tension as a Function of SP-G Protein Concentration

Comparative quantification of SP-G content in tears by Enzyme-Linked Immunosorbent Assay (ELISA) revealed an average value of 0.6411 ng/mg (n = 40) in samples from DED patients (hyper-evaporative form, EDE) (Figure 3A). Healthy donors had an average SP-G protein concentration of 0.1529 ng/mg (n = 20). Thus, the level of SP-G in TF was significantly increased in DED compared to healthy subjects (Figure 3A). Mean SP-G concentrations in ocular tissue samples quantified by ELISA were 0.991 ng/mg in the lacrimal gland (n = 6), 0.826 ng/mg in the conjunctiva (n = 5), and 3.578 ng/mg in the cornea (n = 4) (Figure 3B).

2.4. Putative Surface Activity of SP-G in Tears

SP-G is characterized by surface activity and a certain degree of hydrophobic surface exposure. The putative influence of recombinant SP-G on tear film surface tension was investigated using a spinning drop tensiometer (KRÜSS GmbH, Hamburg, Germany). Changing the concentration of SP-G in the tear film alone resulted in a slight decrease in tear-film IFT from 54 to 49 mN/m (n = 3). A concentration of 100, 500, and 1000 ng/mL SP-G in combination with phospholipid solution (Tears Again (TA)) resulted in a significant

decrease in tear-film IFT from 37 to 32 mN/m (n = 3). The other two samples used as loading controls showed no effect (Figure 3C). In combination with recombinant SP-G (rhuSP-G) in a tear substitute solution (TA), the surface tension is reduced even more than with rhuSP-G alone.

2.5. In Vitro Wound Healing Scratch Assay

The cell culture-based wound healing scratch test (n = 4) mimicked corneal epithelial cell damage and demonstrated the effect of rhuSP-G on wound closure rate in combination with phospholipid solution (Tears Again (TA)) (Figure 4A).

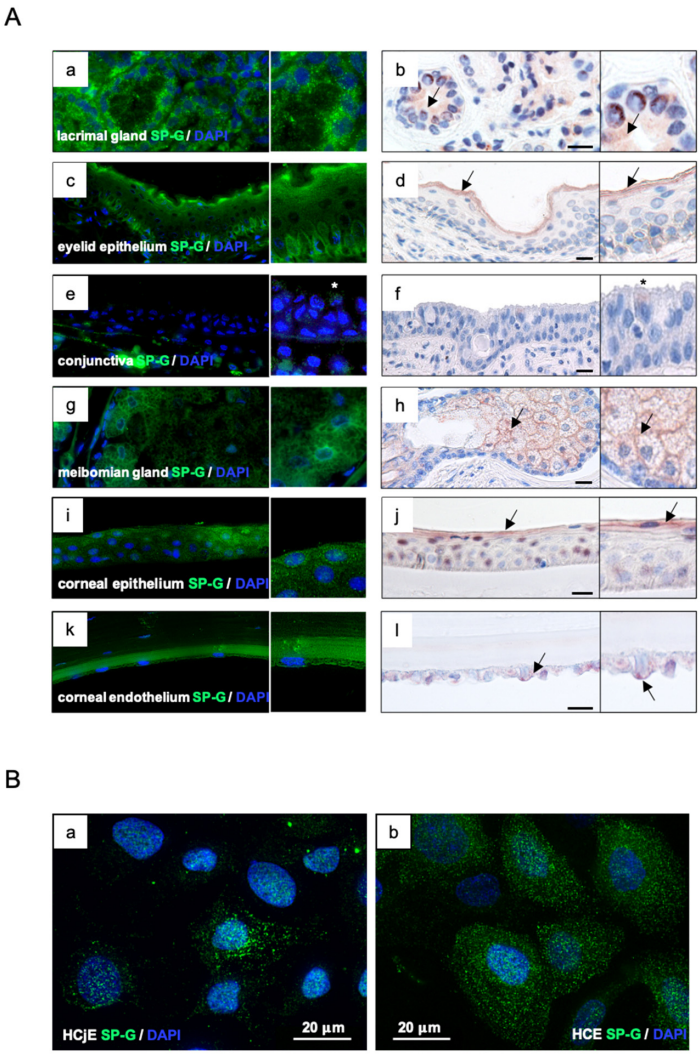

Figure 2. (**A**) Immunohistochemical detection of SP-G (green and red) in lacrimal glands, meibomian glands, eyelid, conjunctiva, corneal epithelium, and corneal endothelium by fluorescence (green, left column) and AEC substrate staining (red, black arrow, right column). (**a**,**b**) Lacrimal glands: detection in cells of secretory ducts as well as in serous acini of the gland. (**c**,**d**) Eyelid: SP-G was detected in the basal epithelium of the eyelid and protein distribution as a superficial layer. (**e**,**f**) Conjunctiva: multilayered epithelium of the conjunctiva from healthy donors shows weak reactivity (white/black star). (**g**,**h**) Meibomian glands: SP-G detected within the cytoplasm of the gland and the excretory duct system cells. (**i**,**j**) Cornea epithelial: protein detected in the basal epithelium and superficial layers of epithelial cells. (**k**,**l**) Cornea endothelial: SP-G detected in the basal epithelial cells. (**B**) HCE (**a**) and HCjE (**b**) cell lines: cytoplasmatic localization of SP-G red and green (SP-G = green; DAPI (4′,6-diamidino-2-phenylindole) = blue). The scale bar equal 50 µm (**A**) and 20µm (**B**).

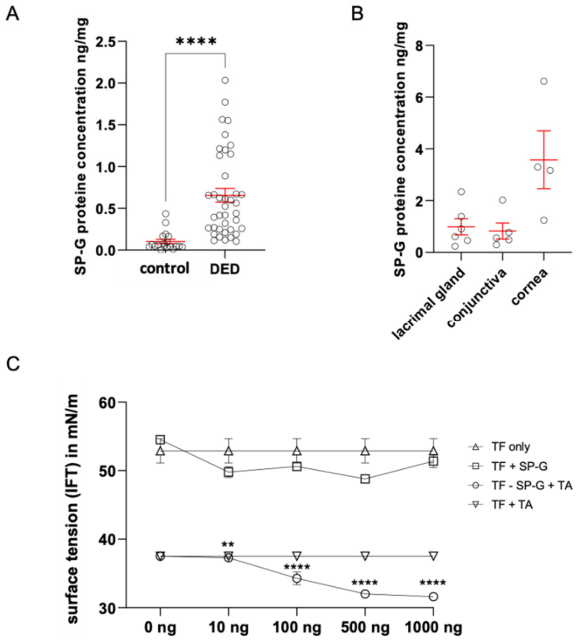

Figure 3. Protein quantification of Human Putative Protein SP-G (SFTA2) in tear fluid and interfacial tension (IFT) analysis. (**A**) Quantification of SP-G in TF. Mean values (red) of healthy subjects: 0.152 ng/mg, EDE: 0.641 ng/mg. (**B**) Quantification of SP-G in ocular tissue samples. Mean values of lacrimal gland: 0.991 ng/mg, conjunctiva: 0.862 ng/mg and in cornea 3.578 ng/mg. (**C**) IFT for different rhu-SP-G concentrations in tear fluid samples. As control we used TF only and TA with TF. The IFT is expressed in mN/m and as mean ± SEM. Statistical significance: ** $p \leq 0.005$, **** $p \leq 0.0005$.

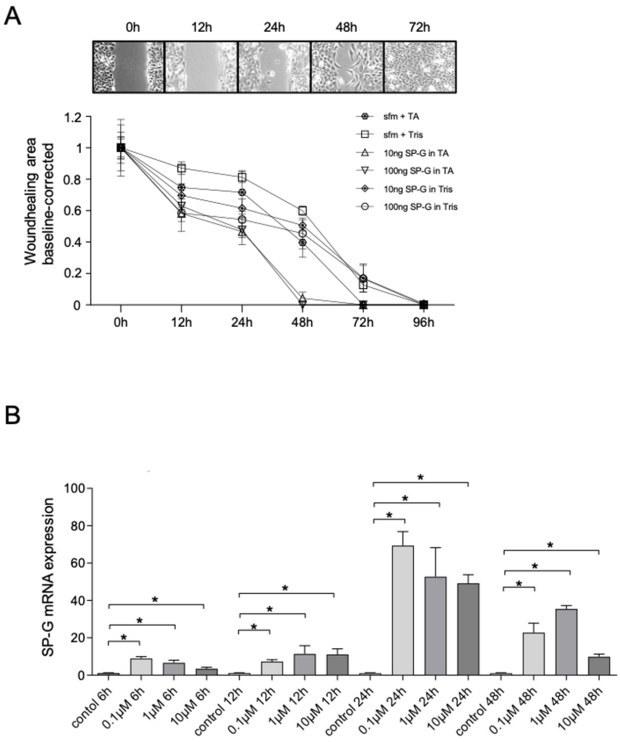

Figure 4. In vitro wound healing scratch assay with HCE cells. (**A**) Baseline corrected wounded area in HCE monolayer cultures incubated with 10 and 100 µg/mL SP-G in TA were compared to the control

control group only treated with TA and with 10 and 100 µg/mL SP-G in tris buffer were compared to the control group with pure tris buffer. The wound-healing rates (closure of the scratch) were significantly higher during stimulation with rhuSP-G, combined to TA the effect was more obvious. After 48 h of incubation with 100 µg/mL rhuSP-G and combined with TA, the wound area is already closed. The wound-healing distance was expressed as mean ± SEM. (**B**) Stimulation of HCE cells for 6, 12, 24, and 48 h after treatment with 0.1, 1, and 10 µM cortisol, respectively. SP-G mRNA expression of HCE cells after stimulation with cortisol was determined by qRT-PCR. SP-G mRNA expression levels are expressed as mean ± SEM. (n = 4; * $p \leq 0.05$).

Both rhuSP-G in Tris buffer and in TA increased the wound closure rate in vitro. The addition of rhuSP-G resulted in increased gap closure by HCE cells in the presence of 100 µg/mL SP-G compared with 0 µg/mL. After 12, 24, and 48 h of incubation with 100 µg/mL SP-G, the remaining wound area was significantly smaller compared to controls (Table 1). A total of 10 µg/mL SP-G showed no effect on wound-healing rate. After 72 h, no effect could be detected even with 100 µg/mL SP-G.

Table 1. Results of the statistical analysis of the scratch assays with the individual pairings. ** $p \leq 0.005$, *** $p \leq 0.0005$.

Time Points	Pairings	Statistical Significance
12 h	sfm + TA vs. 100 ng SP-G + TA	***
12 h	sfm + Tris vs. 100 ng SP-G + Tris	***
24 h	sfm + TA vs. 10 ng SP-G + TA	***
24 h	sfm + TA vs. 100 ng SP-G + TA	***
24 h	sfm + Tris vs. 100 ng SP-G + Tris	**
48 h	sfm + TA vs. 10 ng SP-G + TA	**
48 h	sfm + TA vs. 100 ng SP-G + TA	***

In combination with TA, a significant pronounced wound-closure rate was observed after 12, 24, and 48 h incubation with 10 and 100 µg/mL SP-G compared to the TA control (Table 1). After 48 h incubation with SP-G + TA, the wound area was closed, whereas it took a longer time when incubating the cells with SP-G alone.

2.6. Effects of Cortisol on SP-G mRNA Levels

Cortisol is known for its stimulatory effect on surfactant protein synthesis [22]. We examined different concentrations of cortisol (0.1 µM, 1 µM, and 10 µM) and their effects on SP-G expression in cultured HCE cells. The concentrations of 0.1 µM and 1 µM of cortisol reflect similar levels to those found in stress conditions, and higher concentrations (10 µM) simulate pharmacological doses of glucocorticoids [23]. The use of cortisol leads to a significant increase in SP-G mRNA expression (Figure 4B). After incubation of the cells for 6 h, a significant increase (up to 15-fold) in mRNA expression was initially observed. After an incubation period of 24 h, the highest SP-G mRNA level was observed in the group with a concentration of 0.1 µM. It is noticeable that the effect of cortisol seems to decrease after 24 h, which was also observed after 48 h.

2.7. In Silico Molecular-Level Insight into Interactions of SP-G with Lipids of the Tear Film Lipid Layer (TFLL)

In molecular dynamics (MD) simulations, TFLL models with three different values of polar lipid packing were considered, with area per phospholipid (APPL) = ~0.7, 1.0, and 1.3 nm^2. In each system, SP-G was initially placed in the aqueous subphase at ~2 nm distance from the water–lipid interface. In the two more packed systems (APPL = 0.7 and 1.0 nm^2), the protein did not adsorb to the lipid film during 1 µs of the calculated MD trajectory. However, in the least packed system (APPL = 1.3 nm^2), SP-G preferentially adsorbed at the water–polar 1-palmitoyl-2-oleyl-sn-glycero-3-phosphocholine (POPC) headgroup

boundary within ~250 ns. After adsorption, during the following ~10 ns, the protein was partially incorporated in the lipid film and attained a stable orientation (Figure 5A) for the next 2.7 μs. The analysis of contacts between the protein and lipids (Figure 5E) revealed that polar, basic, and acidic residues of the adsorbed protein were, on average, interacting with water and polar POPC lipids. In contrast, the hydrophobic residues penetrated the POPC monolayer and interacted with nonpolar lipids, mostly with cholesteryl erucate (CE, Figure 5F,G). Spatial density profiles of molecular occupancy in the vicinity of the adsorbed protein (Figure 5H) demonstrate that adsorption of SP-G to the TFLL led to the formation of a pore in the POPC monolayer. The pore was occupied not only by the protein but also by water molecules that hydrated hydrophilic protein residues. Furthermore, some of the nonpolar lipids penetrated the formed pore and interacted with nonpolar residues.

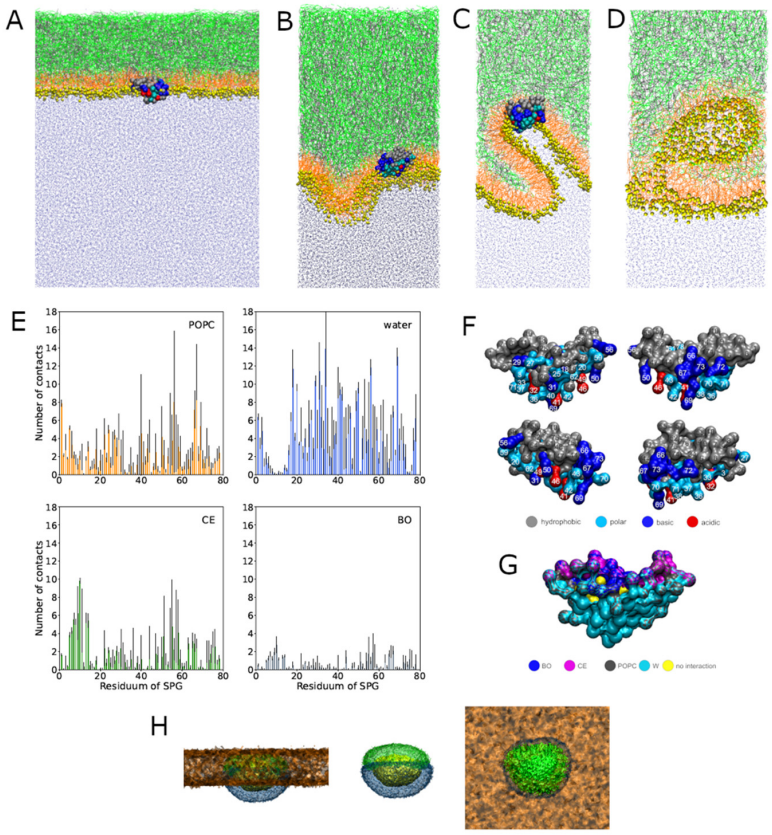

Figure 5. In silico MD simulations of SP-G interactions with a TFLL model. (**A–C**) Representative snapshots of the simulation boxes showing SP-G interacting with TFLL. (**D**) A representative snapshot of the collapsed TFLL in the absence of SP-G. Color coding in all snapshots: POPC lipids—orange lines; polar head groups of POPC—yellow spheres; CE—green lines; behenyl oleate (BO)—gray lines; water—blue dots; SP-G represented by spheres with coloration dependent on the residue type (hydrophobic—gray; polar—blue; basic—dark blue; acidic—red). (**E**) Contact numbers (within the 0.7-nm cutoff) between SP-G and POPC, water, CE, and BO; error bars calculated by block averaging. (**F**) Visualization of the character (hydrophobic, polar, basic, and acidic) of the SP-G residues; four different orientations of the SP-G protein are shown for clarity. (**G**) Visualization of the contact residues (within the 0.7-nm cutoff) of SP-G with individual lipid types and water in the equilibrated system (as shown in panel **A**). (**H**) Spatial densities of SP-G (yellow), POPC (orange), water (blue), and CE (green) in the equilibrated system (as shown in panel **A**). The density of all POPC groups is shown, while only the density of the closely interacting molecules is shown for water and CE. A side view of the film is shown on the left, the same view without POPC is shown in the middle, and the top view (from the air side) is shown on the right.

In a separate MD trajectory, the system with adsorbed SP-G was laterally compressed from APPL = 1.4 to 0.3 nm^2 in the course of 200 ns. During this simulation, the TFLL underwent significant structural alterations, with the formation of initial undulations of the polar POPC layer (Figure 5B), followed by the creation of invaginated structures (Figure 5C). Importantly, during this restructuring, SP-G remained stably adsorbed to the lipid film, and the integrity of the film (continuity of the polar and nonpolar layers) was not compromised (Figure 5B,C). In contrast, the TFLL without the protein, during the same lateral compression process, underwent a collapse forming inverse micelle-like structures, composed of POPC with water, which were pushed out from the polar layer to the nonpolar lipid phase (Figure 5D).

3. Discussion

The first description of a regulatory SP-G-mRNA, which locates in human chromosome 6p21.33, was achieved by Zhang et al. [24]. SP-G was demonstrated in developing lung tissue, bronchoalveolar lavage (BAL), and the immortalized alveolar type II cell line A549 [13,19]. Here, we demonstrate that SP-G is a component of the ocular surface and tears. It is produced by different tissues of the ocular system and the lacrimal apparatus, such as cornea, conjunctiva meibomian gland, and lacrimal gland. From these tissues, SP-G is secreted and becomes part of the tear film. We detected SP-G in corneal and conjunctival epithelial cells that are responsible for the formation of the mucous component of the tear film mainly in the form of membrane-bound mucins. However, we can only speculate that the SP-G produced here is also secreted into the tear film. Moreover, we detected SP-G in secretory duct cells as well as acinar cells of the lacrimal gland, which, together with the accessory lacrimal glands, form a major part of the aqueous component of the tear film (TF). Finally, we also localized SP-G in the meibomian gland acinar cells as well as cells lining the excretory duct, which are responsible for most of the superficial lipid component of the tear film. Since our Western blot and ELISA studies clearly show that SP-G is present in tear fluid, it is most likely that it is secreted into the tear film by all these tissues of the ocular surface (lacrimal gland, meibomian glands, conjunctiva, and cornea). In a previous study, we already demonstrated the presence of SP-G in various extrapulmonary tissues of the ocular surface but also other organs such as heart, kidney, sebaceous glands, and testis [13]. It is interesting to note that the SP-G concentration in human corneas is often up to four-fold higher than in the lacrimal gland tissue and conjunctiva. However, due to the lack of knowledge about the function of SP-G, this finding can only be speculated. However, a correspondingly higher concentration in the cornea was also detected for the protein PLUNC (Palate Lung Nasal Clone), which belongs to the family of surfactant proteins [25]. Here, it is speculated that PLUNC may have a function in the cornea, which is an organ with a very finely regulated fluid balance, in the context of fluid regulation or in immune defense. Similar functions are also conceivable for SP-G, especially since we were also able to detect it in the corneal endothelium, but remain speculative. Our Western blot analysis of tear fluid revealed distinct SP-G protein bands at 15 kDA. Considering that the protein might be posttranslational modified due to glycosylation, phosphorylation and palmitoylation, the distinct protein band at ≈15 kDa seems to represent the mature protein. This expression pattern (15 and 28 kDa) is in accordance with findings in human lung tissue, bronchoalveolar lavage (BAL), and the immortalized alveolar type II cell line A549 [13,19]. In tear fluid from patients with a hyperevaporative form of DED, our ELISA studies revealed a highly significant increase in SP-G concentration in the tear film. Since SP-G is also produced by meibocytes and the epithelial cells of the excretory ducts of the meibomian glands, it is probably integrated into the oily meibum during meibocyte differentiation. It has been clearly demonstrated that meibocytes produce various proteins that interact with the lipids of the meibum [8]. Interestingly, in this context, it appears that DED patients suffering from an evaporative form of DED also have increased SP-G concentrations. In these patients, less meibum is formed with an additional change in viscosity, so the increased SP-G concentration is rather surprising. Three hypotheses are

conceivable for this: (1) More tears and SP-G are produced in response to increased evaporation in the absence of the protective lipid layer of the tear film in MGD, whereupon more SP-G is secreted by the lacrimal gland, conjunctiva, and cornea because of a possible immunologic function and to regulate the fluid balance of the ocular surface, resulting in a higher concentration of SP-G in the tear fluid. (2) A second conceivable reason for the increased SP-G concentration in the tear film is that the relative fluid volume in the tear film is greatly reduced and therefore the ratio of tear film components has shifted in favor of the SP-G protein or other proteins. (3) Another reason could be that SP-G may play a role in immune defense, as has been shown in particular for the surfactant proteins SP-A and SP-D, but also for SP-H [14,26,27]. Since in DED there is a subclinical to clinical inflammatory response at the ocular surface [28,29], SP-G could be upregulated here in response to inflammation. However, Mittal et al. reported that SP-G expression was downregulated by lipopolysaccharides in mice, which is contrary to the SP-G increase observed here in patients with evaporative form of the eye [19].

Our studies show that both HCE and HCjE cell lines we analyzed also express SP-G and thus can serve as in vitro models for SP-G studies. Immortalized cells in most cases deviate from the vital primary cells, also in the case of the used SV-40 HCE cells, which is a limitation of the study. This issue is known from numerous experiments and also other cells lines. But nevertheless, using these cells can provide first insights into to function of SP-G with respect to cellular function. For the experiments we used corneal epithelial cells for initial in vitro studies and performed stimulations with cortisol and wound healing experiments with recombinant SP-G. We chose cortisol as a stimulant because its physiological and pharmacological properties are well known, particularly in the context of maturation of the pulmonary surfactant system of premature infants [30,31]. Despite the commonly known assumption that cortisol might disturb wound healing, the effect of increased SP-G expression seems to exceed the influence of cortisol. After mechanical stress or wounding of confluent HCE cells, treatment with recombinant SP-G in combination with TA resulted in an increased rate of wound healing, such that specific lipids appear to promote the SP-G properties in question. The wound healing is presumably based on an increased migration of the cells through SP-G. An influence by proliferation cannot be excluded at present. Further investigations such as Ki-67 (proliferation marker) must follow. The molecular or even physical mechanisms behind this observation are still unclear and further experiments are needed to unravel this finding, but at least similar properties are known from SP-H [18]. The finding that recombinant SP-G reduces surface tension in tears, as shown by spinning drop analysis (Figure 3C), is further evidence for the function of SP-G. SP-G appears to be able to interact with lipids. The combination with TA enhances the effect and suggests that SP-G can only exert its full function in combination with specific lipids. TA is a phospholipid liposome spray with a high concentration of phosphatidylcholine 2-lysophosphatidylcholine, which improves the polar properties of the lipid layer (e.g., surface tension and solubility) and enhances the distribution of the lipid in the tear film [22,32,33]. First lipid simulations already pointed out the interaction with lipids [21,34]. Already Krieger et al. mentioned in an analysis of a water box that palmitoylation of SP-G can act as a membrane anchor in the lipid environment to stabilize the protein on the lipid surface or mediate its adsorption to the membrane by penetration into the hydrophobic protein core. Therefore, we hypothesize that SP-G in the tear film may reduce surface tension and stabilize the tear film.

In order to obtain deeper insights into whether and how SP-G may potentially interact with tear film lipids, we performed MD simulations. MD simulations revealed molecular-level details of SP-G interactions with an in silico model of TFLL. SP-G adsorbs, interacts with lipids, and incorporates in TFLL with low packing of polar lipids. In the tear film, the packing of lipids at the tear–air interface varies with time as the tear film undergoes significant restructuring, involving thinning, breaking, and respreading after blinks [35]. Furthermore, the blinks cause mechanical mixing of the lipid material with the aqueous subphase. Hence, it can be assumed that SP-G adsorbs to TFLL in the actual tear film.

Simulations also show that SP-G remains stably incorporated upon adsorption despite the lateral mechanical stress. The adsorption of SP-G observed at the molecular level is in accord with previous MD simulations, which considered SP-G interacting with purely polar lipid films [21].The hydrophilic and hydrophobic residues of the adsorbed SP-G interact predominantly with polar and nonpolar lipid molecules, respectively. After incorporating to the lipid film, SP-G spans from the aqueous subphase, through the polar monolayer layer, to the nonpolar lipid layer. To a certain extent, the hydrophilic residues stay hydrated, with the hydrating water partially penetrating the lipid environment in the vicinity of the protein. The adsorption and interaction with lipids reported at the molecular scale by MD are in accord with the experimentally observed surface tension reduction by SP-G. Interactions with POPC lipids are dominant, which agrees well with the observed enhanced activity of SP-G in the presence of phospholipids in tear substitutes. Importantly, MD revealed that the incorporation of SP-G to TFLL enhances the structural stability of the lipid film, allowing it to withstand higher lateral pressure than the TFLL without the protein. In the absence of SP-G, a collapse was observed under corresponding lateral pressure. The present simulations point to an essential role of both polar and nonpolar lipids for SP-G embedment. Of note, the previous computational models of SP-G-lipid interactions considered only polar lipids. It should also be mentioned that no posttranslational modifications of SP-G were considered here; as shown in previous studies, such modifications can additionally enhance SP-G interactions with lipids [21].

In summary, we identified SP-G as a secretory protein at the ocular surface and in tear fluid. There it has been shown to be involved in wound healing of the corneal epithelium. In addition, SP-G is able to reduce the tension of the tear film, especially of tear fluid from patients suffering from dry eyes. Molecular simulations show that SP-G specifically interacts with polar and nonpolar components of the tear lipid film and increases its mechanical stability. Further studies are needed to gain deeper insights into the function and mode of action of SP-G at the ocular surface, particularly with regard to SP-G on the ocular surface immune system and in relation to the pathogenesis and potential treatments of DED and meibomian gland dysfunction.

4. Materials and Methods

4.1. Generation of Samples

Tissue samples were obtained from 6 body donors (3 men, 3 women; age range: 63–95 years) donated to the Institute of Functional and Clinical Anatomy, FAU Erlangen-Nuremberg, Erlangen, Germany. The study was approved according to institutional review board regulations and is consistent with the goals of the Declaration of Helsinki. Samples were collected from the body donors within 24 h post mortem. Half of each sample was immediately frozen at −80 °C for biological studies. The other half was fixed in 4% paraformaldehyde for subsequent embedding in paraffin. Bronchial mucosa and lung tissue were used as positive controls.

The procedure of collecting tear fluid as well as the clinical diagnosis of dry eye has already been described and performed in detail by Schicht et al. [25]. Tear fluid samples were collected with Schirmer strips through PD (Dr. Jacobi at the Department of Ophthalmology, Friedrich Alexander University Erlangen-Nuremberg, Germany). These specimens were obtained in compliance with good clinical practice and with informed consent. Ethical approval was obtained from the Ethics Committee of the University of Erlangen-Nuremberg (54-2532.1-35/13). Written consent was received from all patients and subjects after explanation of the procedures and study requirements. Tears from 20 control samples were included in the study. They showed no symptoms for dry eye disease or ocular discomfort, did not use any artificial tears or lubricant eye drops, and did not suffer from any autoimmune disorders or other eye diseases, including ocular allergies, and had no history of eye surgery or contact lens wearing. A total of 40 tear fluid samples of 40 patients (mean age 42.8 ± 8.3 years) with dry eye (DEWS dry eye severity level 2) were also enrolled in the study. Inclusion criteria were as follows: (i) Ocular Surface Disease Index

questionnaire Score (OSDI Score) > 40, (ii) tear break-up time (TBUT) $\leq$ 10 s, (iii) Schirmer test with anesthesia $\leq$ 10 mm, (iv) lid-parallel conjunctival folds (LIPCOF) > 2. A more detailed description of these points is given below. For the ELISA, the study of patients was limited to the most common form, i.e., evaporative dry eye due to meibomian gland dysfunction (EDE, n = 40). EDE patients had a tear break-up time of $\leq$5 s and a Schirmer test $\leq$ 10 mm. Exclusion criteria consisted of a medical history of trauma or infection, ocular allergies, pregnancy, lactation, history of refractive surgery/ocular surgery/any other surgery within the previous 6 months, immunosuppressive medications, or the use of contact lenses within 14 days prior to ophthalmological examination. Moreover, patients wearing punctum plugs, patients with history or evidence of epithelial keratitis derived from herpes simplex infection, recent varicella infection, corneal or conjunctival viral disease, acute corneal, conjunctival, or palpebral bacterial infection, or ocular fungal infection, were excluded from this study.

4.2. Cell Culture

Immortalized HCE and HCjE cells were cultured as previously described by [18]. SV40-transformed human corneal epithelial cells (HCE cells, obtained from Kaoru Araki-Sasaki, Tane Memorial Eye Hospital, Osaka, Japan, passage number 18–27) [36] as well as a human spontaneously immortalized epithelial cell line from normal human conjunctiva [IOBA-NHC, here referred to as HCjE cells, obtained from Yolanda Diebold, University Institute of Applied Ophthalmobiology (IOBA), University of Valladolid, Valladolid, Spain] [37] were cultured as monolayer and used for further stimulation experiments. For stimulation experiments, cells (1×10^6) were seeded in Petri dishes and cultured until confluence was reached. Before cells were treated with cortisol (0.1 µM, 1 µM, and 10 µM) (Sigma-Aldrich, St. Louis, MO, USA), they were washed with phosphate-buffered saline (PBS) and incubated with serum-free medium for at least 6 h. They were respectively collected after incubating for 6 h, 12 h, 24 h, and 48 h, then isolated for RNA extraction and for continuing further qPCR analysis.

4.3. mRNA Extraction and cDNA Synthesis

Total mRNA was extracted from cell cultures as well as from human tissues: lacrimal gland (n = 12), eyelids (n = 12), conjunctiva (n = 12), and cornea (n = 12) using peqGOLD Tri-Fast reagent (VWR International GmbH, Darmstadt, Germany). For mechanical comminution, SpeedMill plus (Analytik Jena AG, Jena, Germany) was used. After centrifugation (10 min, 15,520$\times$ g), the supernatant was applied for mRNA isolation. DNA contaminations were removed using a standard protocol. Reverse transcription of mRNA samples into first-strand cDNA was performed using the RevertAid Reverse Transcriptase Kit (Thermo Fischer, Waltham, MA, USA) according to the manufacturer's protocol. Two micrograms of total RNA were used for each reaction to cDNA. Gene-specific intron-spanning primers previously synthesized at MWG Biotech AG (Ebersberg, Germany) were used for PCR.

4.4. Polymerase Chain Reaction (PCR)

RT-PCR was performed according to the following standard protocol. Primers used for conventional PCR: SP-G sense (5′- AGCGTGAGCAGGAAGGTTCT -3′) and antisense (5′- GCGCCATGTAAGAGAGCTCT -3′) were used for qRT PCR (i.e., real time). To estimate the amount of amplified PCR product, a β-actin PCR was performed with specific primers: sense (5′-GAT CCT CAC CGA GCG CGG CTA CA-3′) and antisense (5′-GCG GAT GTC CAC GTC ACA CTT CA-3′). The reference gene β-actin was used as an internal control for assessing the integrity and stability of the transcribed cDNA.

4.5. Quantitative Real-Time RT-PCR

Gene expression was analyzed with quantitative Real-Time RT-PCR (qPCR) using a LightCyler480® system (Roche) as previously described by Schicht et al., 2018 [18]. The PCR reaction mixture contained 10 µL LightCycler480®5x probe mastermix, 0.25 µL of

each primer and 2 µL of each cDNA, 0,4 µL Universal ProbeLibrary probe #13 (UPL, Roche) for SFTA2 or #22 for 18S (10 µM) and 7,1 µL nuclease free water. On each 96-well plate, qPCR was performed with a cycle of 5 min at 95 °C, 55 cycles of 15 s at 95 °C, 30 s at 60 °C and 1 s at 72 °C, to confirm amplification of specific transcripts. SP-G and 18 s (sense 5′-GGT GCA TGG CCG TTC TTA-3′ and antisense 5′-TGC CAG AGT CTC GTT CGT TA-3′) primers as well as the corresponding UPL probes (see above) were generated by using the ProbeFinderTM software (Version 2.04, Roche). A standard curve was generated by serial dilutions of cDNA from non-stimulated cells. To standardize mRNA concentration the transcript levels of the housekeeping gene small ribosomal subunit (18S rRNA) were determined in parallel for each sample, and relative transcript levels were corrected by normalization based on the 18S rRNA transcript levels. Each sample was performed in triplicate, and the changes in gene expression were calculated by applying the ΔΔCt method.

4.6. Western Blot

The Western blot aimed to detect SP-G in tear fluid from patients suffering from DED and healthy donors. The tear fluid was mixed with RSB buffer (consisting of Glycerin, 10% SDS, Tris·Base and Mercaptoethanol) and heated at 95 °C for 5 min before loading. Considering the molecular weight of samples, 15% SDS-polyacrylamide gel for electrophoresis was chosen to separate the protein. Afterwards, separated proteins were transferred into a nitrocellulose membrane using a Semi-Dry Transfer Cell (BIO-RAD). Membrane was incubated with the rabbit anti-SP-G antibody in 1% BSA-PBST (1:200) (ABBEXA, Cambridge, UK) at 4 °C overnight and anti-rabbit-HRP in 5% BSA-PBST (1:1000) (Cell Signaling, Danvers, MA, USA) at room temperature for 2 h after blocking with 5% BSA in 1xPBST. Then, the bands were detected with ECL Western blotting detection reagents (EMD Millipore Corporation, Burlington; MA, USA). The molecular weights of the detected protein bands were estimated by using the standard protein marker, Precision Plus Protein Dual Color Standards (ranging from 10 to 250 kDa).

4.7. Immunohistochemistry

Immunohistochemical analysis was performed as previously described by [38]. Tissue samples of lacrimal gland, eyelids, conjunctiva, and cornea from donors were embedded in kerosene, sectioned (5 µm), and deparaffinized for immunohistochemical staining.

Immunohistochemistry was performed according to a standard general protocol. Sections were incubated with primary polyclonal antibodies (1:50) (Abbexa) against SP-G overnight at 4 °C, and secondary antibodies (goat anti-rabbit) (1:200) (Dako) were incubated for at least 2 h at room temperature. Visualization was performed with AEC (Dako) for an appropriate time.

For immunohistochemical analysis of cells, cells were cultured on glass coverslips and fixed with 4% PFA for 1 min. Visualization of antibody binding was performed with AEC for an appropriate time. Sections were counterstained with hematoxylin and then coverslipped with Aquatex (Merck kGaA, Darmstadt, Germany).

For fluorescent staining, cells were incubated overnight with rabbit anti-SP-G antibody (1:50 in TBST) (Seqlab) and for 2 h with fluorescein isothiocyanate (FITC)-conjugated antibody (Alexa 488, green) diluted 1:200 with TBS. Cells were embedded with DAPI-glycerol (PBS-glycerol 1:1, by adding 10 µL of a 2 mg/mL stock DAPI solution) on glass slides. The slides were examined using a Keyence Biorevo BZ9000 microscope.

4.8. Enzyme-Linked Immunosorbent Assay (ELISA)

Tear fluid of healthy donors and from patients suffering from DED (hyperevaporative) as well as ocular tissue samples were analyzed by quantitative sandwich ELISA. The analysis was performed by using SFTA2 ELISA kit and the relevant protocols from Cusabio Biotech Co., Ltd. (Wuhan, China). Quantification was accomplished by comparison with the 2-fold standard dilution series and the determined values for antigen concentration

ranging from 0.312 ng/mL to 20 ng/mL. Subsequently, each sample was approximated to ng/mg.

4.9. In Vitro Wound Healing Scratch Assay

HCE cells were seeded in Petri dishes and cultured until confluence was reached. Before scratching, the cells were incubated with serum-free medium (sfm) for at least 6 h. Then, the cell lawn was disrupted with a pipette tip (100 µL yellow tip, Eppendorf) to create an epithelial defect. Subsequently, cells were stimulated with 10 or 100 ng/mL rhuSP-G in combination with a tear replacement solution (phospholipid liposome spray—Tears Again (TA) Optima Pharmazeutische GmbH, Hallbergmoos, Germany) in sfm. TA is a phospholipid liposome spray with a high concentration of phosphatidylcholine 2-lysophosphatidylcholine, which improves the polar properties of the lipid layer (e.g., surface tension and solubility) and improves the distribution of the lipid in the tear film [32–34]. TA was purchased at a local pharmacy. Optima GmbH did not financially support the investigations in this study. Tris (Tris(hydroxymethyl)aminomethane) buffer were used to stabilize the SP-G protein and as an internal control (sfm + Tris) to exclude the influence of Tris buffer. Subsequently, the wound edges were measured at different time points (0 h, 3 h, 6 h, 12 h, 18 h, 24 h, 36 h, and 48 h). ImageJ (open source software) was used to evaluate the wound area. The average distance was calculated and analyzed to evaluate the effect of SP-G.

4.10. Interfacial Tension

The experiment was performed as previously described by [18]. The method itself is described by www.kruss.de (accessed on 17 May 2022). A spinning drop interfacial tensiometer (model Kruss, Germany) was used to measure the surface and interfacial tensions of the tear fluid containing various concentrations of SP-G at room temperature in combination with Tears Again (TA) (see above).

4.11. Molecular Dynamics Simulations

Molecular dynamics simulations were performed employing the setup similar to that used in previous tear film computational studies [39,40]. In short, in the simulation box elongated along one direction, a slab of water was placed forming two water–air interfaces. At each interface, a lipid film consisting of POPC (1-palmitoyl-2-oleyl-sn-glycero-3-phosphocholine), BO (behenyl oleate), and CE (cholesteryl erucate) was spread, and the system was equilibrated for a few hundred nanoseconds. One molecule of SP-G was then placed in the water slab and its adsorption was simulated in a direct MD simulation. The MARTINI coarse grain model was used for describing molecular interactions, with the elastic network method used to maintain the shape of the protein [41]. The slab consisted of ~90,000 water beads and the lipid film at each interface comprised of 727 molecules of POPC, and 1250 molecules of each BO and CE. The size of the simulation box was equal to $22 \times 22 \times 104$ nm^2 and the corresponding area per polar POPC was equal to 0.7 nm^2. Less laterally packed interfaces were simulated be reducing the number of POPC lipids, equally at both interfaces. The size of the simulation box was kept constant, and the temperature was set to an average 310 K (NVT ensemble). Simulations of lateral film compression were realized by turning on the pressure coupling algorithm with the lateral pressure of 15 bar. Several replicas of each simulation were performed. GROMACS (ver. 2020.4) software was employed as the MD simulation engine and VMD (ver. 1.9.3) was used for visualization [42,43].

4.12. Statistical Analysis

Calculations and visualizations were performed using GraphPad Prism 6 (GraphPad Prism Software). The statistical analysis was carried out by using an unpaired, a two-sided Mann–Whitney U-test (nonparametric data) or two-sided Welch's t-test (parametric data) with mean ± standard error of the mean (SEM) of all data. Significance value was defined at * $p < 0.05$, ** $p < 0.005$ or *** $p < 0.0005$.

Author Contributions: Conceptualization, L.B., M.S., F.P. and L.C.; methodology, M.S., K.R., M.K., W.L. and A.S.; software, K.R., M.K. and L.C.; tear fluid acquisition and clinical testing, L.B., M.S. and C.J.; validation, L.B., F.P. and L.C.; investigation, M.S., K.R., W.L., A.S. and F.G.; resources, M.S., L.B., C.J. and F.P.; writing—original draft preparation, M.S., F.P., L.C. and L.B.; writing—review and editing, all authors; visualization, M.S., K.R. and M.K.; supervision, L.B., L.C. and F.P.; project administration, L.B.; funding acquisition, F.P. All authors have read and agreed to the published version of the manuscript.

Funding: F.P. was supported by Deutsche Forschungsgemeinschaft (DFG), grant PA738/15-1. M.S. was supported by Sicca Forschungsförderung of the professional Association of German Ophthalmologists and by the Ernst und Berta Grimmke Stiftung (Program Grant 1/15), K.R. and L.C. were supported by Czech Science Fundation, grant 21-19854S.

Institutional Review Board Statement: This study was conducted in compliance with institutional review board regulations, informed consent regulations, and the provisions of the Declaration of Helsinki and its later amendments. This study was approved by the university's ethical review committee (Ref. No. 3555; FAU Erlangen-Nürnberg, Ref. No. 2013-30; MLU Halle-Wittenberg).

Informed Consent Statement: Written informed consent was obtained from each patient concerning diagnostic procedures, treatment, and the subsequent use of these specimens for research purposes, including data analysis, prior to inclusion in this study.

Data Availability Statement: Please contact authors for data requests (M.S.; email: martin.schicht@fau.de).

Acknowledgments: The authors sincerely thank those who donated their bodies to science so that anatomical research could be performed. Results from such research can potentially increase knowledge that can improve patient care. Therefore, these donors and their families deserve our highest gratitude. Moreover, the authors would like to thank the participating patients for donating samples for our research. The authors would also like to thank Maike Hemmerlein, Anke Fischer-Gößwein, and Hong Nguyen for their technical support. M.K. acknowledges the PL-Grid Infrastructure and the Academic Computational Center Cyfronet of the University of Science and Technology in Krakow, Poland, for computational resources.

Conflicts of Interest: The authors declare no conflict of interest. The authors (M.S., K.R., M.K., W.L., A.S., F.G., C.J., F.P., L.C. and L.B.) have no proprietary or commercial interest in any materials discussed in this manuscript.

References

1. Craig, J.P.; Nelson, J.D.; Azar, D.T.; Belmonte, C.; Bron, A.J.; Chauhan, S.K.; de Paiva, C.S.; Gomes, J.A.P.; Hammitt, K.M.; Jones, L.; et al. TFOS DEWS II Report Executive Summary. *Ocul. Surf.* **2017**, *15*, 802–812. [CrossRef] [PubMed]
2. Uchino, M.; Schaumberg, D.A. Dry Eye Disease: Impact on Quality of Life and Vision. *Curr. Ophthalmol. Rep.* **2013**, *1*, 51–57. [CrossRef] [PubMed]
3. Kurihara, H.; Sato, T.; Akimoto, N.; Ogura, T.; Ito, A. Identification and characterization of ABCB1-mediated and non-apoptotic sebum secretion in differentiated hamster sebocytes. *Biochim. Et Biophys. Acta* **2011**, *1811*, 1090–1096. [CrossRef] [PubMed]
4. Craig, J.P.; Nichols, K.K.; Akpek, E.K.; Caffery, B.; Dua, H.S.; Joo, C.K.; Liu, Z.; Nelson, J.D.; Nichols, J.J.; Tsubota, K.; et al. TFOS DEWS II Definition and Classification Report. *Ocul. Surf.* **2017**, *15*, 276–283. [CrossRef]
5. Paulsen, F.; Garreis, F. What drives Meibomian gland disease? *Arch. Soc. Esp. Oftalmol.* **2014**, *89*, 175–176. [CrossRef]
6. Nelson, J.D.; Shimazaki, J.; Benitez-del-Castillo, J.M.; Craig, J.P.; McCulley, J.P.; Den, S.; Foulks, G.N. The international workshop on meibomian gland dysfunction: Report of the definition and classification subcommittee. *Investig. Ophthalmol. Vis. Sci* **2011**, *52*, 1930–1937. [CrossRef]
7. Dietrich, J.; Garreis, F.; Paulsen, F. Pathophysiology of Meibomian Glands—An Overview. *Ocul. Immunol. Inflamm.* **2021**, *29*, 803–810. [CrossRef]
8. Green-Church, K.B.; Butovich, I.; Willcox, M.; Borchman, D.; Paulsen, F.; Barabino, S.; Glasgow, B.J. The international workshop on meibomian gland dysfunction: Report of the subcommittee on tear film lipids and lipid-protein interactions in health and disease. *Investig. Ophthalmol. Vis. Sci.* **2011**, *52*, 1979–1993. [CrossRef]
9. Holly, F.J.; Lemp, M.A. Tear physiology and dry eyes. *Surv. Ophthalmol.* **1977**, *22*, 69–87. [CrossRef]
10. Wright, J.R. Immunoregulatory functions of surfactant proteins. *Nat. Rev. Immunol.* **2005**, *5*, 58–68. [CrossRef]
11. Crouch, E.; Wright, J.R. Surfactant proteins a and d and pulmonary host defense. *Annu. Rev. Physiol.* **2001**, *63*, 521–554. [CrossRef] [PubMed]
12. Yu, S.H.; Possmayer, F. Role of bovine pulmonary surfactant-associated proteins in the surface-active property of phospholipid mixtures. *Biochim. Biophys. Acta* **1990**, *1046*, 233–241. [CrossRef]

13. Rausch, F.; Schicht, M.; Paulsen, F.; Ngueya, I.; Bräuer, L.; Brandt, W. "SP-G", a putative new surfactant protein-tissue localization and 3D structure. *PLoS ONE* **2012**, *7*, e47789. [CrossRef]
14. Schicht, M.; Rausch, F.; Finotto, S.; Mathews, M.; Mattil, A.; Schubert, M.; Koch, B.; Traxdorf, M.; Bohr, C.; Worlitzsch, D.; et al. SFTA3, a novel protein of the lung: Three-dimensional structure, characterisation and immune activation. *Eur. Respir. J.* **2014**, *44*, 447–456. [CrossRef] [PubMed]
15. Bräuer, L.; Kindler, C.; Jäger, K.; Sel, S.; Nölle, B.; Pleyer, U.; Ochs, M.; Paulsen, F.P. Detection of Surfactant Proteins A and D in Human Tear Fluid and the Human Lacrimal System. *Investig. Ophthalmol. Vis. Sci* **2007**, *48*, 3945–3953. [CrossRef] [PubMed]
16. Bräuer, L.; Johl, M.; Börgermann, J.; Pleyer, U.; Tsokos, M.; Paulsen, F.P. Detection and Localization of the Hydrophobic Surfactant Proteins B and C in Human Tear Fluid and the Human Lacrimal System. *Curr. Eye Res.* **2007**, *32*, 931–938. [CrossRef] [PubMed]
17. Schicht, M.; Posa, A.; Paulsen, F.; Bräuer, L. The ocular surfactant system and its relevance in the dry eye. *Klin. Mon. Fur Augenheilkd.* **2010**, *227*, 864–870. [CrossRef]
18. Schicht, M.; Garreis, F.; Hartjen, N.; Beileke, S.; Jacobi, C.; Sahin, A.; Holland, D.; Schroder, H.; Hammer, C.M.; Paulsen, F.; et al. SFTA3—A novel surfactant protein of the ocular surface and its role in corneal wound healing and tear film surface tension. *Sci. Rep.* **2018**, *8*, 9791. [CrossRef]
19. Mittal, R.A.; Hammel, M.; Schwarz, J.; Heschl, K.M.; Bretschneider, N.; Flemmer, A.W.; Herber-Jonat, S.; Konigshoff, M.; Eickelberg, O.; Holzinger, A. SFTA2-A Novel Secretory Peptide Highly Expressed in the Lung-Is Modulated by Lipopolysaccharide but Not Hyperoxia. *PLoS ONE* **2012**, *7*, e40011.
20. Keicho, N.; Ohashi, J.; Tamiya, G.; Nakata, K.; Taguchi, Y.; Azuma, A.; Ohishi, N.; Emi, M.; Park, M.H.; Inoko, H.; et al. Fine localization of a major disease-susceptibility locus for diffuse panbronchiolitis. *Am. J. Hum. Genet.* **2000**, *66*, 501–507. [CrossRef]
21. Rausch, F.; Schicht, M.; Brauer, L.; Paulsen, F.; Brandt, W. Protein modeling and molecular dynamics simulation of the two novel surfactant proteins SP-G and SP-H. *J. Mol. Modeling* **2014**, *20*, 2513. [CrossRef] [PubMed]
22. Craig, J.P.; Purslow, C.; Murphy, P.J.; Wolffsohn, J.S. Effect of a liposomal spray on the pre-ocular tear film. *Cont. Lens Anterior Eye* **2010**, *33*, 83–87. [CrossRef] [PubMed]
23. Miller, D.B.; O'Callaghan, J.P. Neuroendocrine aspects of the response to stress. *Metabolism* **2002**, *51* (Suppl. S1), 5–10. [CrossRef]
24. Zhang, Z.; Henzel, W.J. Signal peptide prediction based on analysis of experimentally verified cleavage sites. *Protein Sci.* **2004**, *13*, 2819–2824. [CrossRef] [PubMed]
25. Schicht, M.; Rausch, F.; Beron, M.; Jacobi, C.; Garreis, F.; Hartjen, N.; Beileke, S.; Kruse, F.; Bräuer, L.; Paulsen, F. Palate Lung Nasal Clone (PLUNC), a Novel Protein of the Tear Film: Three-Dimensional Structure, Immune Activation, and Involvement in Dry Eye Disease (DED). *Investig. Ophthalmol. Vis. Sci* **2015**, *56*, 7312–7323. [CrossRef] [PubMed]
26. Hartshorn, K.L.; Crouch, E.; White, M.R.; Colamussi, M.L.; Kakkanatt, A.; Tauber, B.; Shepherd, V.; Sastry, K.N. Pulmonary surfactant proteins A and D enhance neutrophil uptake of bacteria. *Am. J. Physiol* **1998**, *274 Pt 1*, L958–L969. [CrossRef]
27. Diler, E.; Schicht, M.; Rabung, A.; Tschernig, T.; Meier, C.; Rausch, F.; Garreis, F.; Bräuer, L.; Paulsen, F. The novel surfactant protein SP-H enhances the phagocytosis efficiency of macrophage-like cell lines U937 and MH-S. *Bmc Res. Notes* **2014**, *7*, 851. [CrossRef]
28. Lemp, M.A.; Foulks, G.N. The definition and classification of dry eye disease. *Ocul. Surf.* **2007**, *5*, 75–92.
29. Albertsmeyer, A.-C.; Kakkassery, V.; Spurr-Michaud, S.; Beeks, O.; Gipson, I.K. Effect of pro-inflammatory mediators on membrane-associated mucins expressed by human ocular surface epithelial cells. *Exp. Eye Res.* **2010**, *90*, 444–451. [CrossRef]
30. Ballard, P.L. Hormonal influences during fetal lung development. *Ciba Found. Symp* **1980**, *78*, 251–274.
31. Liley, H.G.; White, R.T.; Benson, B.J.; Ballard, P.L. Glucocorticoids both stimulate and inhibit production of pulmonary surfactant protein A in fetal human lung. *Proc. Natl. Acad. Sci. USA* **1988**, *85*, 9096–9100. [CrossRef] [PubMed]
32. Dausch, D.; Lee, S.; Dausch, S.; Kim, J.C.; Schwert, G.; Michelson, W. Comparative study of treatment of the dry eye syndrome due to disturbances of the tear film lipid layer with lipid-containing tear substitutes. *Klin. Mon. Fur Augenheilkd.* **2006**, *223*, 974–983. [CrossRef] [PubMed]
33. Nosch, D.S.; Joos, R.E.; Job, M. Prospective randomized study to evaluate the efficacy and tolerability of Ectoin(R) containing Eye Spray (EES09) and comparison to the liposomal Eye Spray Tears Again(R) (TA) in the treatment of dry eye disease. *Cont. Lens Anterior Eye* **2021**, *44*, 101318. [CrossRef] [PubMed]
34. Krieger, E.; Joo, K.; Lee, J.; Lee, J.; Raman, S.; Thompson, J.; Tyka, M.; Baker, D.; Karplus, K. Improving physical realism, stereochemistry, and side-chain accuracy in homology modeling: Four approaches that performed well in CASP8. *Proteins Struct. Funct. Bioinform.* **2009**, *77* (Suppl. S9), 114–122. [CrossRef]
35. Cwiklik, L. Tear film lipid layer: A molecular level view. *Biochim. Et Biophys. Acta* **2016**, *1858*, 2421–2430. [CrossRef]
36. Araki-Sasaki, K.; Ohashi, Y.; Sasabe, T.; Hayashi, K.; Watanabe, H.; Tano, Y.; Handa, H. An SV40-immortalized human corneal epithelial cell line and its characterization. *Investig. Ophthalmol. Vis. Sci* **1995**, *36*, 614–621.
37. Diebold, Y.; Calonge, M.; Enriquez de Salamanca, A.; Callejo, S.; Corrales, R.M.; Saez, V.; Siemasko, K.F.; Stern, M.E. Characterization of a spontaneously immortalized cell line (IOBA-NHC) from normal human conjunctiva. *Investig. Ophthalmol. Vis. Sci* **2003**, *44*, 4263–4274. [CrossRef]
38. Schicht, M.; Knipping, S.; Hirt, R.; Beileke, S.; Sel, S.; Paulsen, F.; Bräuer, L. Detection of surfactant proteins A, B, C, and D in human nasal mucosa and their regulation in chronic rhinosinusitis with polyps. *Am. J. Rhinol. Allergy* **2013**, *27*, 24–29. [CrossRef]
39. Wizert, A.; Iskander, D.R.; Cwiklik, L. Organization of lipids in the tear film: A molecular-level view. *PLoS ONE* **2014**, *9*, e92461. [CrossRef]

40. Wizert, A.; Iskander, D.R.; Cwiklik, L. Interaction of lysozyme with a tear film lipid layer model: A molecular dynamics simulation study. *Biochim. Biophys. Acta Biomembr.* **2017**, *1859*, 2289–2296. [CrossRef]
41. Marrink, S.J.; Tieleman, D.P. Perspective on the Martini model. *Chem Soc. Rev.* **2013**, *42*, 6801–6822. [CrossRef] [PubMed]
42. Abraham, M.J.; Murtola, T.; Schulz, R.; Páll, S.; Smith, J.C.; Hess, B.; Lindahl, E. GROMACS: High performance molecular simulations through multi-level parallelism from laptops to supercomputers. *SoftwareX* **2015**, *1–2*, 19–25. [CrossRef]
43. Humphrey, W.; Dalke, A.; Schulten, K. VMD: Visual molecular dynamics. *J. Mol. Graph.* **1996**, *14*, 33–38. [CrossRef]

6 Publication IV: H1 helix of colicin U causes phospholipid membrane permeation

BBA - Biomembranes 1864 (2022) 183866

Contents lists available at ScienceDirect

BBA - Biomembranes

journal homepage: www.elsevier.com/locate/bbamem

H1 helix of colicin U causes phospholipid membrane permeation

Kamila Riedlová [a,b], Tereza Dolejšová [a,c], Radovan Fišer [c,*], Lukasz Cwiklik [a,*]

[a] J. Heyrovský Institute of Physical Chemistry, Czech Academy of Sciences, Dolejškova 3, 18223 Prague, Czech Republic
[b] Department of Physical and Macromolecular Chemistry, Faculty of Science, Charles University, Hlavova 8, 12800 Prague, Czech Republic
[c] Department of Genetics and Microbiology, Faculty of Science, Charles University, Viničná 5, 12843 Prague, Czech Republic

ARTICLE INFO

Keywords:
Colicins
Lipid membranes
Permeation
Poration
Molecular dynamics
Leakage

ABSTRACT

In light of an increasing number of antibiotic-resistant bacterial strains, it is essential to understand an action imposed by various antimicrobial agents on bacteria at the molecular level. One of the leading mechanisms of killing bacteria is related to the alteration of their plasmatic membrane. We study bio-inspired peptides originating from natural antimicrobial proteins colicins, which can disrupt membranes of bacterial cells. Namely, we focus on the α-helix H1 of colicin U, produced by bacterium *Shigella boydii*, and compare it with analogous peptides derived from two different colicins. To address the behavior of the peptides in biological membranes, we employ a combination of molecular simulations and experiments. We use molecular dynamics simulations to show that all three peptides are stable in model zwitterionic and negatively charged phospholipid membranes. At the molecular level, their embedment leads to the formation of membrane defects, membrane permeation for water, and, for negatively charged lipids, membrane poration. These effects are caused by the presence of polar moieties in the considered peptides. Importantly, simulations demonstrate that even monomeric H1 peptides can form toroidal pores. At the macroscopic level, we employ experimental co-sedimentation and fluorescence leakage assays. We show that the H1 peptide of colicin U incorporates into phospholipid vesicles and disrupts their membranes, causing leakage, in agreement with the molecular simulations. These insights obtained for model systems seem important for understanding the mechanisms of antimicrobial action of natural bacteriocins and for future exploration of small bio-inspired peptides able to disrupt bacterial membranes.

1. Introduction

The globally increasing antibiotic resistance causes that intensive efforts are ongoing toward designing new antimicrobial agents [1]. One of the strategies for such design is to understand in detail and then take inspiration from various natural agents able to kill bacteria. In this respect, a particularly attractive group of antimicrobial agents are bacteriocins – proteins or peptides produced by bacteria to inhibit or kill similar or related bacterial strains [2]. Colicins are antimicrobial proteins produced mainly by strains of *Escherichia coli* to kill other closely related enterobacteria [3]. Several classes of colicins were characterized based on their function: forming channels in the inner membrane, degrading nucleic acids, and inhibiting cell-wall synthesis [3,4]. Colicins are considered possible alternatives to antibiotics due to their receptor specificity on target bacteria, their various target structures within bacteria, and low or no cytotoxicity for mammalian cells [5,6]. Furthermore, colicins can kill non-growing bacteria, which can be otherwise resistant to antibiotic treatment [7]. Importantly, colicins are also studied due to their potential use in designing novel bacteriocins [5].

Most of colicins include three functional domains: N-terminal (NTD), central (CD), and C-terminal (CTD) [3,8]. The channel-forming colicins recognize and bind to specific outer membrane receptors of the target Gram-negative bacteria by their CD. Subsequently, their NTD enables translocation of the whole colicin through the outer membrane into the periplasmic space. In the next stage, CTD inserts into the inner membrane, undergoes a structural change, and forms a transmembrane pore promoting the cytotoxic activity via inner membrane depolarization followed by ATP depletion and death of the target cell [3]. CTD is highly conserved across pore-forming colicins, in terms of the sequence and three-dimensional structure according to the crystallographic models of the soluble state. Still, its form in a solution is probably significantly different from the membrane-bound structure before and after the pore opening [3]. Although *E. coli* is one of the most widespread bacteria in the human body and plenty of its strains can produce many different colicins, the functional mechanisms of their action, in particular the

* Corresponding authors.
E-mail addresses: fiserr@natur.cuni.cz (R. Fišer), lukasz.cwiklik@jh-inst.cas.cz (L. Cwiklik).

https://doi.org/10.1016/j.bbamem.2022.183866
Received 21 October 2021; Received in revised form 29 December 2021; Accepted 3 January 2022
Available online 8 January 2022
0005-2736/© 2022 Elsevier B.V. All rights reserved.

details of the channel-forming ability, are still not fully understood.

Here, we study the action of a bio-inspired helical peptide (H1) originating from the CTD domain of colicin U on several model lipid membranes. Colicin U is produced by *Shigella boydii*, one of the bacterial species responsible for shigellosis [9,10]. We compare the membrane behavior of the peptide originating from colicin U with that of two analogous peptides derived from a better-known channel-forming colicins A and Ia with the known crystal structure of their CTDs [11,12].

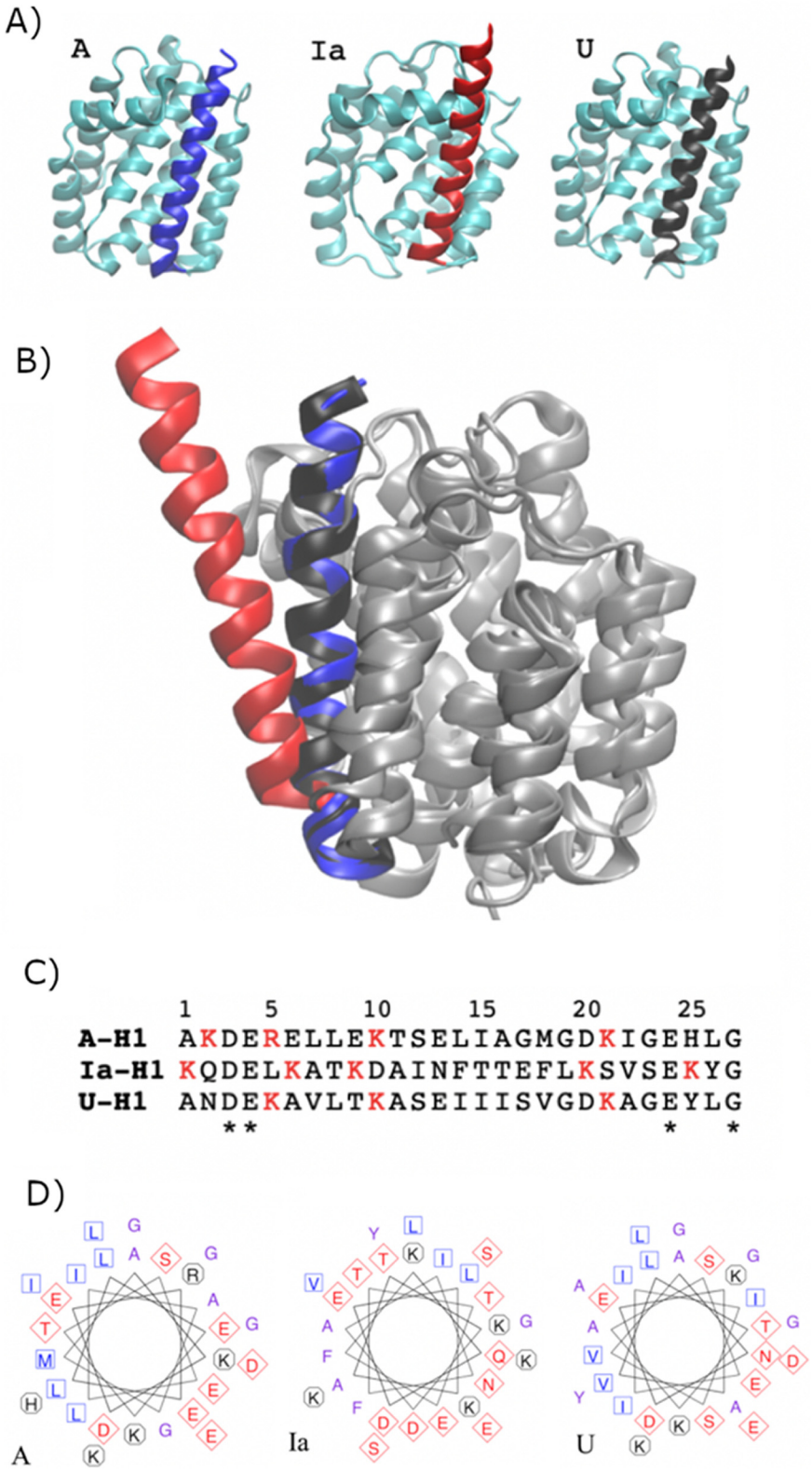

Fig. 1. Individual (A) and overlaid (B) C-terminal domains of the considered colicins with their H1 helices highlighted, demonstrating similar localization of H1 in all three structures. The amino acid sequences (C) and the wheel representations (D) show the presence of polar and nonpolar sides in the three helices (amino acid color coding: red - polar and negatively charged, black - positively charged, blue and violet - nonpolar and hydrophobic).

In the three considered colicins, the CTD consists of ten α-helices H1–H10. Helices H1–H7 and H10 are amphipathic; H8 and H9 are hydrophobic. In the case of colicins A and Ia, such a structure arises from crystallographic data; for colicin U a homology modeling leads to the prediction of an analogic structure. Even though the structural details regarding arrangement and position of the individual helices in membrane-embedded CTD were proposed in the literature [13–16], it is still plausible that these helical arrangements may differ across various pore-forming colicins. Aiming to identify the necessary structural fragments that enable pore formation by colicins, we explore a hypothesis that the first helix from the CTD (H1) of the considered colicins plays a key role in pore formation. This assumption stems from the fact that H1 is a part of CTD that directly continues toward the central domain (CD), and it was proved that following helices of CTDs (H2–H5) in case of colicin A and Ia are translocated after channel opening into the cytoplasm [14]; hence H1 should occur in the transmembrane orientation. Furthermore, the amphipathic character of H1 makes it a good candidate to exhibit a pore-forming activity, as known from other peptidic bacteriocins [2].

To better understand the behavior of the studied peptides in model membranes, we employ atomistic molecular dynamics (MD) simulations. We consider the peptide derived from the H1 helix of CTD in colicin U in three model lipid membranes and compare it with analogous peptides derived from colicins A and Ia. These simulations enabled us to pinpoint the molecular-level mechanism of membrane poration. We also found that poration is most pronounced in the negatively charged lipid membranes. The simulation results are corroborated by experiments using co-sedimentation and leakage assays that prove that the interaction of the H1 helix of colicin U with membranes leads to the permeabilization of negatively charged vesicles.

2. Methods

2.1. All-atom molecular dynamics simulations

The structures of pore-forming domains of colicins A and Ia were taken from the Protein Data Bank PDB: 1COL:A, Ref. [11]; (PDB: 1CII, Ref. [12];). The structure of the CTD of colicin U was generated by homology modeling using iTasser [17]. Then, amino acid sequences of H1 helices were identified between residues 5–31 (colicin A), 442–468 (colicin Ia), and 1–27 (colicin U homology model) based on multiple sequence alignment using Clustal Omega [18]. The amino acid sequences of the considered H1 peptides are shown in Fig. 1. As a control, a highly hydrophobic helical synthetic peptide LW21 (GLLDSKKWWLLLLLLLALLLLLLLWWKKFSRS) was used [19]. AMBER99SB-ILDN force field was employed for proteins [20].

Lipid membranes consisting of 128 lipids (64 in each leaflet) were build using POPC (1-palmitoyl-2-oleoyl-glycero-3-phosphocholine), POPE (1-palmitoyl-2-oleoyl-sn-glycero-3-phosphoethanolamine), or POPG (1-palmitoyl-2-oleoyl-sn-glycero-3-phospho-glycerol) lipids for which the Slipids force field, compatible with the protein force field, was employed [21,22]. Each membrane was solvated with ~5000 water molecules for which TIP3p water model was used [23]. The membranes containing negatively charged peptides were neutralized by an appropriate number of positively charged K^+ counterions. Furthermore, the negatively charged POPG membrane was neutralized by adding 128 K^+ ions. Additionally, in each system, K^+ and Cl^- ions were added at the physiological concentration of 0.154 M. The standard Dang's force field parameters were used for all ions [24]. In the peptide-containing systems, a single H1 peptide (or LW21) was embedded into the model membrane under the protocol by Javanainen, in which the peptide is pushed into a lipid membrane from its side employing high lateral pressure [25]. These pre-prepared membranes were subjected to 300 ns equilibration, as described later on.

MD simulations were performed using the GROMACS 2016.4 package [26]. Periodic boundary conditions were employed. Simulations were run at the temperature of 310 K controlled by the Nose-Hoover thermostat with a time constant of 0.5 ps [27]. Pressure of 1 bar was controlled by the semi-isotropic Parrinello-Rahman barostat with the time constant of 10 ps [28]. All covalent bonds were constrained by the LINCS algorithm, water molecules were constrained by the SETTLE method [29,30]. The Particle Mesh Ewald algorithm was used for long-range electrostatic interactions with the real-space cutoff set to 1.4 nm [31]. For long-range non-bonded interactions, 1.6 nm cutoff was used, and 1.4 nm cutoff was employed for short-range interactions. Equations of motion were solved with 2 fs time step. The simulation length for all simulations was 500 ns, with 300 ns for equilibration and the last 200 ns used for analysis. Stabilization of the area per lipid, RMSD, and peptide-lipid contacts were taken as equilibration criteria. The same simulation protocol was employed for all systems (lipid-only membranes and membranes with embedded H1 or LW21 peptides).

For analysis of trajectories, standard GROMACS tools were employed. For contacts, the following cutoffs, based on radial distribution functions, were used: 0.23 nm for peptide-water contacts; and 0.7 nm for peptide-lipid acyl chains and peptide-lipid headgroups contacts. The numerical data were visualized using the Matplotlib library in Python [32]. Molecular images were obtained by Pymol and VMD software [33,34]. The wheel representations of peptides were created using the pepwheel tool from the EMBOSS online server [35]. The grand average of hydropathicity (GRAVY) was calculated using the ExPASy online server [36].

2.2. Large unilamellar vesicles (LUV) preparation

Liposomes of 100 nm diameter for the leakage assay were prepared following the method described previously [37]. Namely, lipids (1,2-dioleoyl-sn-glycero-3-phospho-(1′-rac-glycerol)) – DOPG (Avanti Polar Lipids, inc., USA) in the amount of 1 mg were dissolved in chloroform, which was subsequently evaporated by a flow of nitrogen at 4 °C, forming a thin layer on the walls of glass tubes. After that, a solution of 50 mM carboxyfluorescein (CF), 5 mM HEPES (pH 7.4) was added, and the multilamellar vesicles were formed by shaking the tube. Subsequently, the large unilamellar vesicles (LUVs) were prepared by repeated extrusion of suspension through a polycarbonate membrane (100 nm pore diameter) using the LiposoFast Basic apparatus (Avestin, Canada). The free probe was removed by gel filtration with a column containing sephadex G50 and elution buffer containing 150 mM KCl, 5 mM HEPES, 0.5 mM EDTA, pH 7.4 (TBS buffer). Finally, flowthrough fractions were collected, and the inorganic phosphate content within the fractions was analyzed [38]. The fractions with the highest phosphate concentration were used as a stock suspension, which was diluted in TBS buffer to obtain the desired LUVs suspension (final phosphate concentration 25 μM). Large unilamellar vesicles from DOPG for co-sedimentation assay were prepared analogically without CF in 150 mM KCl, 10 mM HEPES, pH 7. The gel filtration step was omitted. The final phospholipid concentration used for co-sedimentation assay was 100 μM.

2.3. Carboxyfluorescein leakage assay

In experiments, we used the synthetic H1 peptide (GeneScript, USA) with the same amino acid sequence as a colicin U H1 model used in simulations (ANDEKAVLTKASEIIISVGDKAGEYLG). Liposome leakage assay was performed in 3 × 3 mm quartz cuvettes of a minimal volume of 0.1 ml on FluoroMax-3 spectrofluorometer (Jobin Yvon, Horriba). Fluorescence intensities were recorded continuously after adding various concentrations of H1 peptide into liposome suspension at 515 nm wavelength after excitation at 480 nm. To gain a maximal intensity after the disintegration of all liposomes, Triton X-100 was added (at a final concentration of 0.1% *v*/v) into each measured sample. Every addition of peptide or Triton X-100 was followed by thorough mixing of the sample. Fluorescence intensity was detected every second. The

relative leakage value was calculated according to the equation:

$$\%of\ leakage = \frac{FI - FI_0}{FI_{max} - FI_0} \cdot 100\%$$

where FI_0 and FI are fluorescence intensities measured before and after peptide addition, respectively, and FI_{max} is the maximum fluorescence intensity after Triton X-100 addition. To characterize the rate of liposomal lysis, the first 25 s of each kinetic were fitted to a straight line. Its slope reflects the initial rate of lysis (%·s^{-1}).

2.4. Co-sedimentation assay

To quantify the amount of H1 peptide effectively bound to liposomes, we utilized a co-sedimentation assay. Aliquots of DOPG liposomes at 100 μM final concentration were incubated for 30 min at 37 °C with the H1 peptide or with melittin (MilliporeSigma, USA) as a positive control. After that, the samples (volume 500 μl) were centrifuged at 30,000 *g* at 4 °C for 1 h. Then the pellet (80 μl) and supernatant (420 μl) were separated and treated with 0.1 M Na_2CO_3 (pH 11) to wash out non-specifically bound peptide molecules, centrifuged again (30,000*g*, 4 °C, 1 h) and separated as previously to pellet and supernatant. Finally, the presence of the peptide in the samples was quantified employing relative tyrosine fluorescence (tryptophan fluorescence in case of melittin) with FluoroMax-3 spectrofluorometer (Jobin Yvon, Horriba) in quartz cuvettes of minimal volume 0.1 ml. Synchronous fluorescence spectra in the range from 220 nm to 330 nm were recorded with a fixed 28 nm separation between excitation and emission monochromators (with 5 nm bandpasses). All samples were measured at least in quadruplicate. The spectra were corrected for the background of the blank samples without peptides. Then, the intensities of the corrected spectra of pellets (I_{pellet}) and supernatants ($I_{supernatant}$) were integrated in the range 260 to 290 nm. In case of 100% successful liposome separation by centrifugation, the binding efficiency (BE) could be calculated according to the equation:

$$BE\ (\%) = 2 \cdot \left(\frac{I_{pellet}}{(I_{pellet} + I_{supernatant})} - \frac{1}{2} \right) \cdot 100\%$$

with the assumption that the volume of the pellet also contains the free non-bound peptide in the buffer. However, the technical efficiency of sedimentation was checked by the recovery of liposomes labeled with fluorescent probe 1,6-Diphenylhexatriene (DPH, MilliporeSigma, USA), which were treated in the same way as other samples, and it was found to be around 90%. Therefore, we included the recovery into the calculation that uses fluorescence intensities multiplied with the particular fraction volume (corresponding finally to probe amount):

$$BE\ (\%) = (R_{max} - R_{DPHmin}) / (R_{sample} - R_{DPHmin}) \cdot 100\%,$$

where $R_{max} = (I_{non\text{-}bound} \cdot V_{supernatant}) / (I_{non\text{-}bound} \cdot V_{pellet})$ represents the maximum possible ratio of corrected intensities of supernatant and pellet in case there is 0% peptide (or probe) binding to liposomes. In our case, the volumes are $V_{supernatant} = 420$ μl, $V_{pellet} = 80$ μl and $R_{max} = 5.25$.

The parameter $R_{DPHmin} = (I_{DPHsupernatant} \cdot V_{supernatant}) / (I_{DPHpellet} \cdot V_{pellet})$ characterizes the real technical effectivity of liposomes sedimentation quantified by the intensity of DPH-labeled liposomes in the supernatant and pellet. In our case, $R_{DPHmin} = 0.532$ while expecting ~100% probe binding.

The fractionation of the studied peptide is characterized by the parameter $R_{sample} = (I_{supernatant} \cdot V_{supernatant}) / (I_{pellet} \cdot V_{pellet})$ utilizing the integrated tyrosine (tryptophan) intensities in supernatant and pellet and corresponding fraction volumes. The value of parameter R_{sample} should be between R_{DPHmin} and R_{max}.

3. Results

3.1. MD simulations

Localization of the H1 helical fragment in the C-terminal domain of the three considered colicins is presented in Fig. 1, together with the amino acid sequences of the peptides. For colicins A and Ia, crystal structures are known in their soluble state. In contrast, a crystal structure is not available for colicin U. Hence, the homology model was used here (see Methods section). The three CTDs are structurally similar, with comparable localization of H1 helices (Fig. 1A). In colicins A and U, the H1 position is virtually identical (Fig. 1B). Regarding the amino acid sequence (Fig. 1C), all three H1 fragments show similarity in localization of their polar charged amino acids. More specifically, in each sequence, either arginine or lysine is located at three positions; 5 or 6, 9 or 10, and 19 or 20. Importantly, each H1 is amphipathic, exhibiting segregation of polar and hydrophobic residues between the two faces of the helix (Fig. 1D). The amphipathic character of the helices is quantified via the grand average of hydropathicity (GRAVY) index (see supplementary Table S1).

Localization of H1 peptides in the model membranes is presented at the representative snapshots of the simulated systems obtained after equilibration shown in Fig 2. The snapshots depict the three H1 peptides in the lipid membranes composed of POPC, POPE, and POPG. The POPC system is supposed to be a minimalistic model of the mammalian plasma membrane, while both POPE and POPG bilayers mimic the inner plasma membrane of Gram-negative bacteria. In simulations, the peptide was initially put in the transmembrane orientation, and the systems were allowed to evolve for 500 ns. In all cases, H1 peptides remained stably incorporated in the membranes. It is evidenced by the calculated distances between the helix center of mass and the bilayer midplane shown in the supplementary Fig. S1. While in the membrane, the H1 peptides attained transmembrane orientation as visible in the presented snapshots. Different initial placements of the helices were also tested, such as the peptide adsorbed in parallel to the water-membrane interface or placed in-between the membrane leaflets. Still, these localizations were not stable in the course of MD simulations.

In all cases, the α-helices were tilted with respect to the membrane normal, as shown in Fig. S2. The RMSD values calculated along the simulated trajectories (Fig. S3) show no significant changes in the helical structures. Still, minor but functionally important restructuring was observed. Namely, as visible in the simulation snapshots in Fig. 2, the membrane-embedded H1 peptides were kinked. Based on a visual analysis of the trajectories, we identified several kink positions. In all helices, the kink occurred around the highly hydrophilic charged lysine and arginine residues (positions 5 or 6, position 10, and position 20 or 21). Furthermore, H1 of colicin A and U were also kinked at their glycine and serine residues (position 16 or 17). The presence of the kinks is evidenced in the secondary structure analysis shown in Fig. S4, where a partial loss of helicity is observed along the trajectories. To further analyze these kinks, the tilt angles were calculated for selected shorter fragments of each helix (see Fig. S2). Distributions of these angles have well-defined peaks, demonstrating that the kinks lead to a stable and specific orientation of the helical sub-segments in the membranes. An exception is the H1 of colicin U in POPG, with no distinctive peaks were observed, indicating the peptide's relatively flexible orientation in the membrane (also confirmed by the secondary structure analysis in Fig. S4).

The simulation snapshots depicted in Fig. 2 also show that the presence of the peptides caused the restructuring of all considered membranes. Namely, in the vicinity of the peptide C-terminal, membrane defects were formed by water molecules penetrating the headgroup region of the membrane. Water penetration into the headgroup region was also observed on the N-terminal side, albeit to a lesser extent. Apart from the water defects in the membrane headgroup section, penetration of water molecules into the hydrophobic membrane core

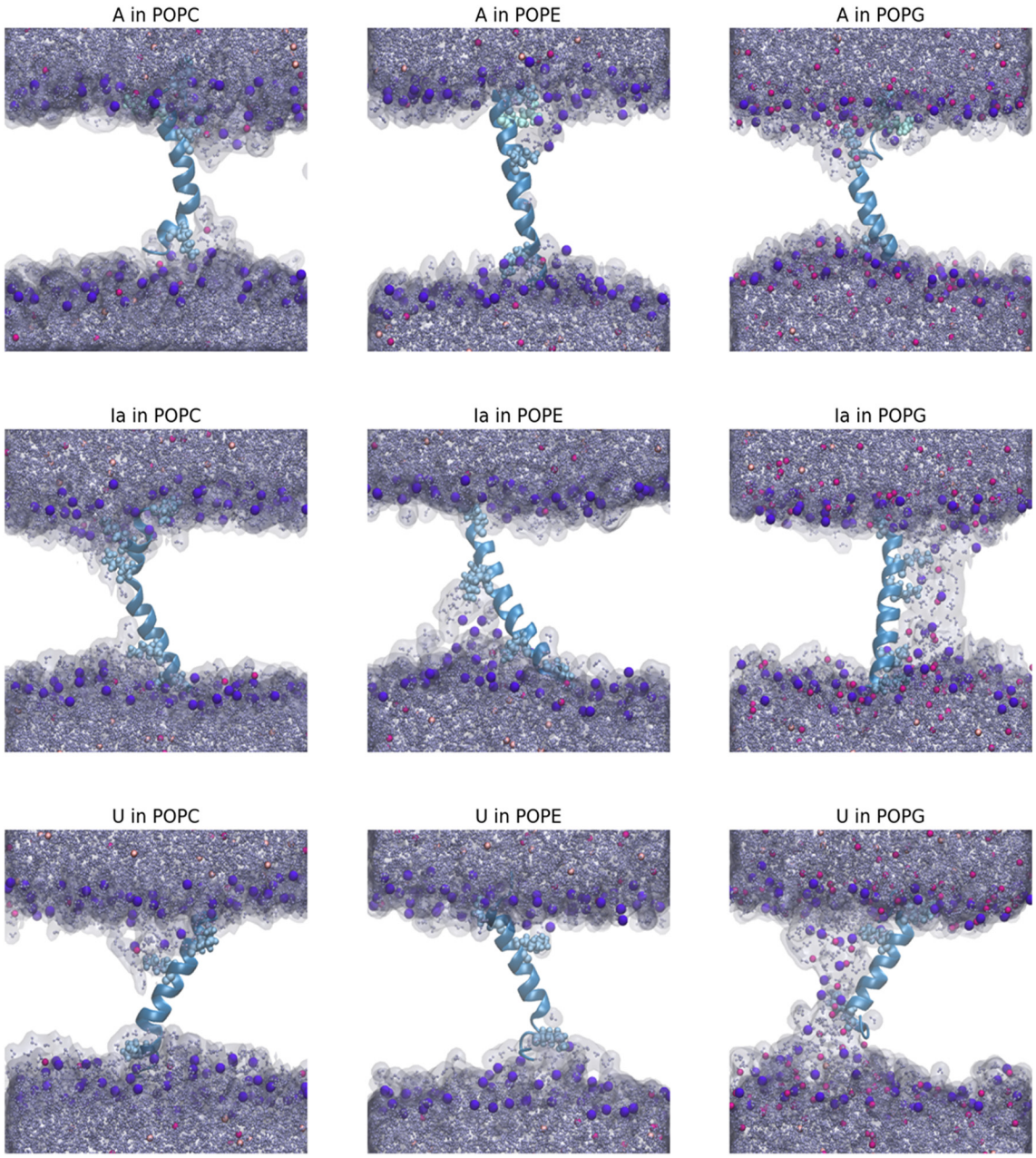

Fig. 2. Representative snapshots of H1 peptides of the considered colicins obtained after system equilibration in MD simulations in different lipid membranes. The snapshots demonstrate transmembrane localization of the helices and the formation of water defects in the membranes. Color coding: grey - water, magenta - K^+ ions, pink - Cl^- ions, violet - phosphate atoms of POPC/POPE/POPG, blue - peptide, white - lipid chains. Peptides are oriented in lipid bilayers from N- (top) to C-terminal (bottom).

was also observed in the vicinity of the transmembrane helices in all studied membranes. The water penetration effectively led to membrane permeation. In most cases, these only individual water molecules penetrated the membrane core; in two instances, H1s of colicin Ia and U in the POPG membrane, the formation of a stable water pore was observed. The development of water defects in the lipid headgroup region also caused remodeling of the water-lipid interface by partial reorientation of polar lipid headgroups. Namely, the entering water caused tilting of the polar headgroups that followed the water molecules hydrating the membrane interior and formation of toroidal pore-like structures (see Fig 2, Ia and U in POPG).

Water penetration was predominantly observed on one face of the H1 peptides. This behavior can be rationalized by the amphipathic character of the helices, with one side mainly being polar and hydrophilic and the other being nonpolar and hydrophobic (see Fig. 1D). The asymmetry is particularly pronounced in H1 of colicin U, and it leads to enhanced water penetration in the vicinity of H1 of colicin U. Water molecules primarily penetrated the membrane to hydrate the charged arginine and lysine residues (at positions 5 or 6; 9 or 10; and 19 or 20). The other polar residues located deeper in the membrane core (from 10 to18) were hydrated to a lesser extent. Again, in the case of H1s of colicin Ia and U in POPG, hydration along the whole peptide was substantial, resulting in pore formation.

Density profiles presented in Fig. 3 provide further insight into the membrane structure with incorporated peptides and demonstrate the presence of water defects mentioned above. In all simulated systems, a stable transmembrane localization of the peptides is evident by comparing the density curves for the whole peptide with that of lipid

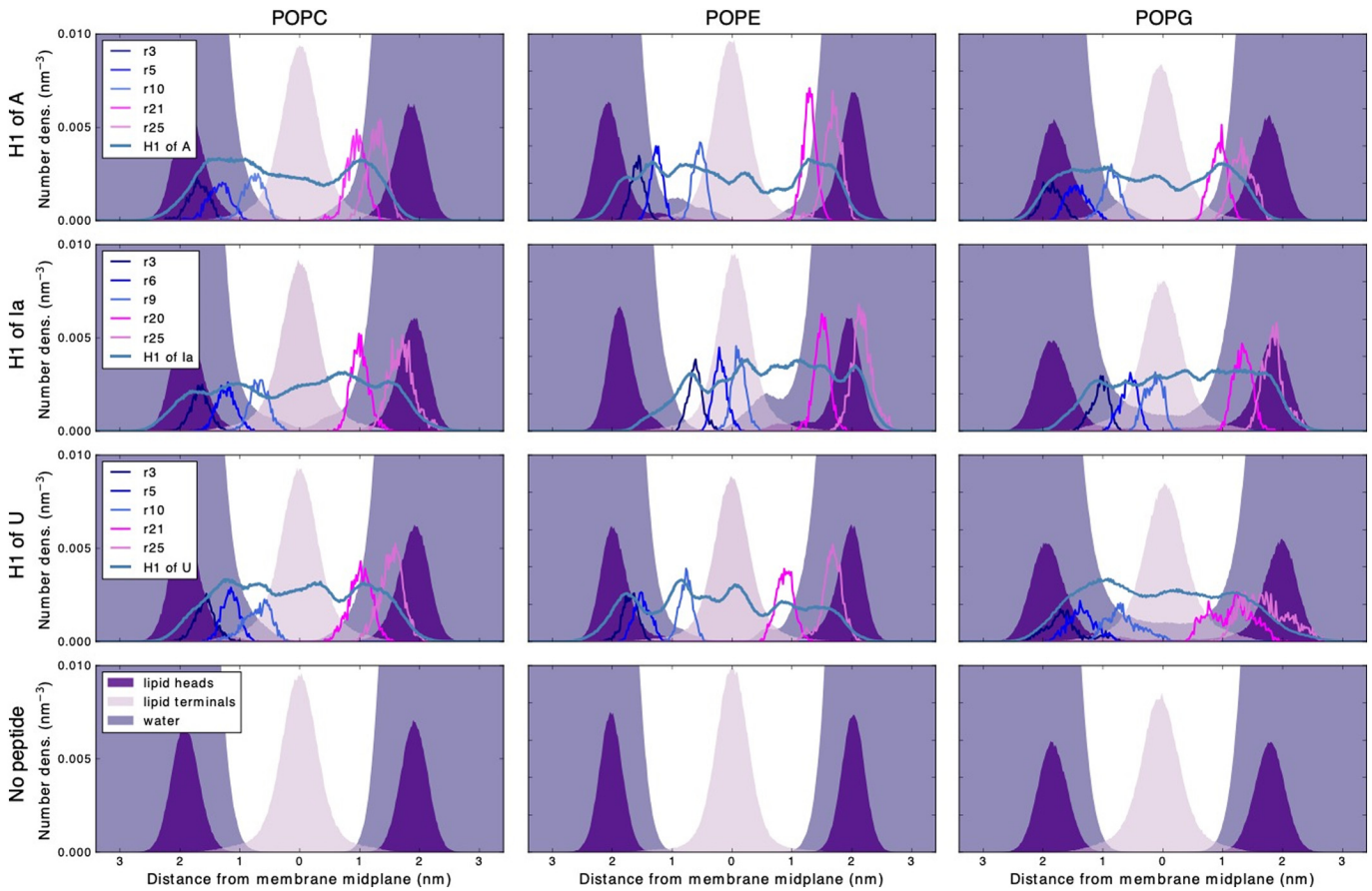

Fig. 3. Number density profiles of the simulated systems for all considered helices (three first rows) and lipid membrane compositions (columns). For comparison, the profiles of peptide-free membranes are presented in the bottom row. Phosphate atom was used for localization of lipid heads, and the last carbon atom of the sn-2 alkyl chain of phospholipids defined its terminal. Selected polar residues of the peptides are also shown. For presentation purposes, the densities of individual groups are scaled (the same in all panels). Note the different peptide density profiles in the central part of the membranes and, for membranes with peptides, water penetration into the hydrophobic membrane core.

headgroups. The sections of the peptides located near the flanking residues (r3, r5 near the N-terminal; and r21, r25 near the C-terminal) span out of the lipid headgroups into the water phase. The secondary structure analysis (Fig. S4) and the helicity analysis (Fig. S5) show that these sections of the peptides are unstructured, as can be expected in the well-hydrated water–membrane interface. The residues that approximately correspond to the beginning and end of the helical fragment (residues 3 and 25, see Fig. 3) are located in the still relatively well-hydrated lipid headgroup regions. The density profiles corresponding to the charged side chains (r5 or r6, r9 or r10, and r25) are in the sub-headgroup area. In all cases, the density profiles of the charged groups overlap with the density profile of water; it proves that the charged side chains remain hydrated while the peptides span the membranes. We quantified the hydration of the residues by counting the contacts between water residues and individual amino acids. The results for H1 of colicin U are presented in Fig. 4 (two upper rows), confirming that the polar residues in the membrane core remain hydrated. Note that the inner residues of hydrophobic helical transmembrane peptides, such as LW21 shown as a control in Fig. 4, are typically entirely dehydrated.

A comparison of the water density profiles in the presence of H1 peptides with those of pure lipid membranes (Fig. 3, bottom row) shows an increased water density in H1-containing membranes. Overall, the embedded H1 peptides cause water penetration into the typically hydrophobic membrane regions. In particular, in H1s of colicin Ia and U in POPG, the water density across all membranes is nonzero. It evidences the presence of a transmembrane pore, as discussed beforehand. Furthermore, in all considered cases, the increased water penetration is accompanied by a distorted density of lipid headgroups. In particular, in the systems with transmembrane pores, the headgroup density spreads into the membrane; it corresponds to the formation of the toroidal pore. The propensity of lipid headgroups toward the transmembrane segment of the pore-forming H1 of colicin U is quantified, employing the contact numbers analysis (Fig. 4, third row). In all considered membranes, we observe a tendency of lipid headgroups to accompany the peptide residues, particularly in the case of the POPG bilayer, for which the pore is formed. Such behavior is absent for the control purely hydrophobic transmembrane helix LW21 (Fig. 4, bottom row). The presence of lipid headgroups in the proximity of transmembrane segments of H1 peptides also caused a reduction of peptide-lipid tails contacts. This effect is quantified for helix U in Fig. 4 (third panel), and it is significantly different from the data obtained for the hydrophobic LW21 (bottom panel). We observed qualitatively similar behavior for other considered helices (see supplementary Figs. S6 and S7).

3.2. *Experiments*

In experiments, we studied interactions of the synthetic H1 peptide derived from colicin U with DOPG liposomes. DOPG lipids were employed to mimic the negatively charged bacterial plasma membrane, and the doubly-unsaturated acyl chains were chosen to assure a liquid membrane state at room temperature. Using the liposome leakage assay, we detected the lysis of DOPG liposomes after adding the H1 peptide derived from colicin U (Fig. 5A). This behavior proved that the peptide associates with the phospholipid bilayer and can cause disintegration of

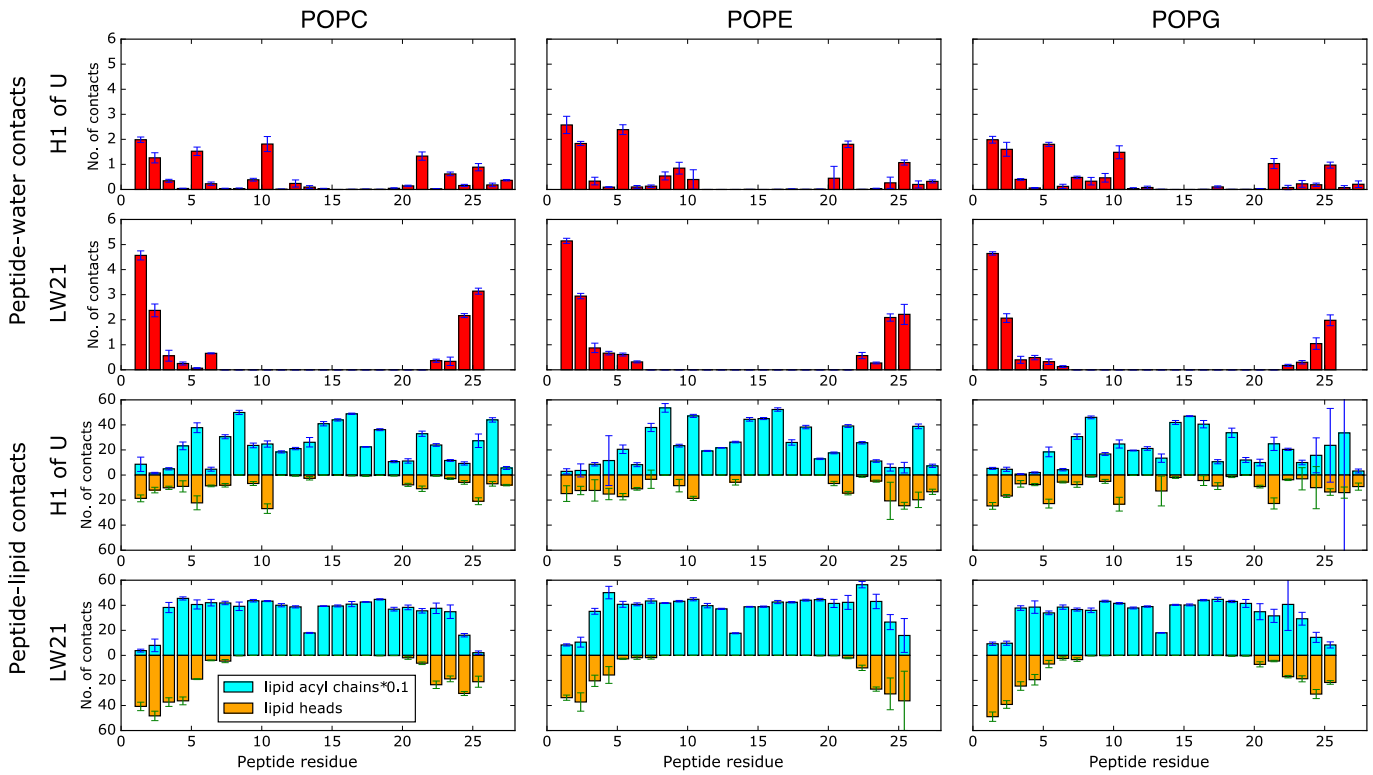

Fig. 4. Numbers of contacts of the considered H1 peptides with water, lipid tails, and lipid headgroups. As a control, the data obtained for LW21 peptide are also shown. Error bars are obtained using the block averaging method. Data for the other peptides are presented in supplementary Figs. S6 and S7.

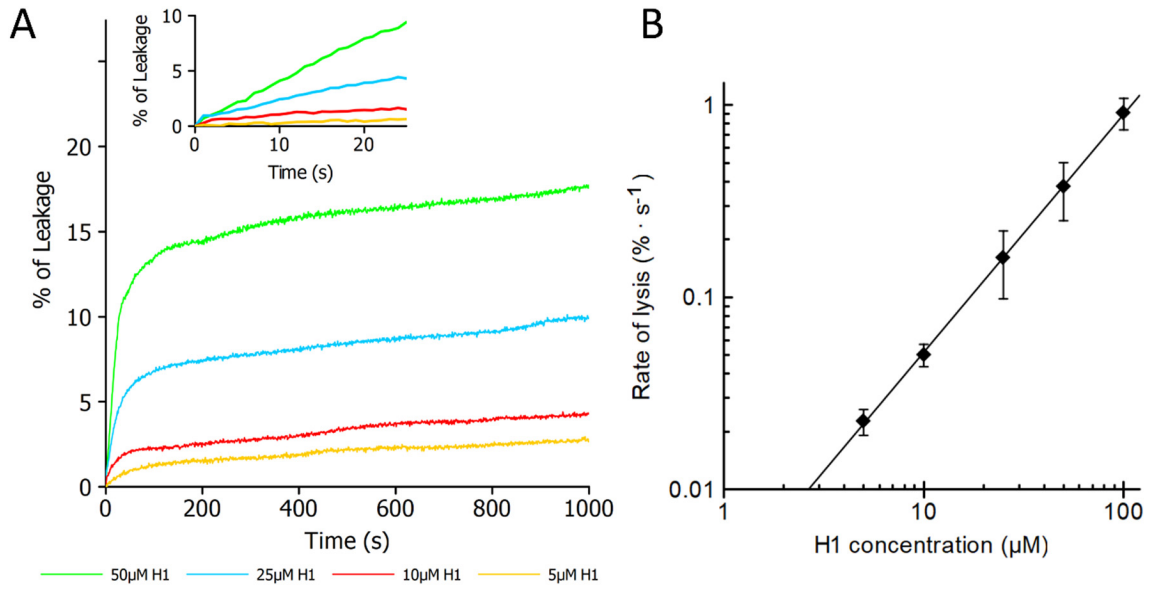

Fig. 5. The H1 peptide of colicin U induces lysis of DOPG liposomes (25 μM final phospholipid concentration). A) Various H1 peptide concentrations (see the graph legend) directly affect both the lysis rate and maximum final leakage of the liposomes. The 100% leakage was determined as lysis after adding 0.1% Triton X-100 at the end of each kinetics. Representative kinetics are shown ($n = 3$). Inset: initial phase of the leakage kinetics (25 s). B) The initial rate of lysis (%·s^{-1}) induced by the H1 peptide shows very weak cooperativity. The data can be fitted to the power function $y = k \cdot x^B$ where $B = 1.24 \pm 0.058$ (asymptotic standard error 4.6%).

the liposomal membranes. Furthermore, we analyzed a dependency of the lysis efficiency on H1 peptide concentration. With an increased concentration of H1 peptide, we detected almost linearly enhanced lysis of the DOPG liposomes (Fig. 5B). In an attempt to estimate the lysis cooperativity, we fitted the initial lysis rate as a function of H1 concentration in a double-logarithmic plot to a power function with exponent 1.24 (Fig. 5B – see Ref. [39], section "Estimation of pore stoichiometry" for derivation). This value suggests very low cooperativity of H1 action on liposomal membranes. Moreover, it lets to deduce that only small H1 complexes or possibly peptide monomers can disturb the bilayer.

To induce a detectable liposomal leakage, we had to use relatively high concentrations of H1 peptide. To find out why it was necessary, we decided to test the H1 peptide efficiency of binding into membranes of

LUVs. Therefore, we proceeded with a co-sedimentation assay on DOPG liposomes. We observed that after the addition of 10 μM of H1 peptide to DOPG liposomes (at final phospholipid concentration 100 μM), only about 2.5 (±1.5) % of the peptide was bound to liposomes, which corresponds to 0.25 μM final concentration of membrane inserted peptide. Such a low amount of peptide was able to induce the leakage of ~3% of liposomal content (at final phospholipid concentration 25 μM) after 5 min (Fig. 5A). Of note, it can be expected that the binding efficiency could be much enhanced in the case of the intact C-terminal domain or whole colicin U, thanks to the predicted hydrophobic hairpin (H8 and H9), which should have a strong tendency to insert into phospholipid bilayer [40]. Another amphipathic peptide, melittin, was used as a positive control of membrane binding, which was detected using the tryptophan fluorescence instead of tyrosin in the case of the H1 peptide. With melittin (10 μM), we detected binding efficiency of about 94% under comparable conditions.

4. Discussion

We investigated the behavior of the H1 peptide of colicin U in model lipid membranes and compared it with that of colicin A and Ia. We aimed to identify whether the H1 peptide can alter the bacterial model membranes and lead to membrane poration. The crystal structure of colicin U is unknown; therefore, we used a homology model and compared it with colicins A and Ia.

Regarding the membranes, we used zwitterionic phospholipids POPC and POPE and anionic POPG. It should be noted that these are single-component models. Nevertheless, such models allow for an understanding of underlying mechanisms of lipid-peptide interactions, which then can be generalized toward natural, multicomponent bacterial membranes. To obtain a molecular-level insight, we employed in silico atomistic molecular dynamics simulations. We complemented simulations by experiments using negatively charged DOPG lipid LUVs; the measurements included carboxyfluorescein leakage assays and binding quantification using co-sedimentation assays.

The three considered H1 helices are located in a similar region of the corresponding CTDs. As demonstrated previously, these CTDs are embedded in a plasmatic membrane after the colicins translocate into a periplasm of an attacked bacteria [3]. Regarding H1, the earlier studies proved that, as a part of CTD, it is embedded in the membrane, most likely in parallel or semi-parallel orientation to the membrane (umbrella and penknife models, see Ref. [3]). However, after the channel opening, the position of H1 changes, and the helices of CTD undergo significant reorientation. The studies focused on colicin A, and Ia in the open channel state proved that the segments of few helices (approximately from H2 to H5) are translocated into the cytoplasm. It suggests that the H1 helix of colicin A and Ia should be in such a case in transmembrane orientation [14]. Therefore, in simulations, we considered the transmembrane orientation of the peptides.

We studied short helical fragments, mimicking the wild-type H1s. Therefore, similarities and differences between these model species and the wild-type peptides should be considered. Overall, the character of the studied helices is intermediate between the hydrophobic and hydrophilic, as demonstrated by their close to zero grand hydropathicity index. In this sense, they resemble other helical, membrane-penetrating, and pore-forming peptides, such as Melittin, Pardaxin P-4, Buforin II, and Magainin 2. Such amphipathic and relatively short peptides (ranging from 23 to 33 amino acids) are typically stabilized in the membrane core by high free-energy barriers related to a robust stabilization of their charged terminals in the polar headgroup regions [41,42]. On the other hand, they can translocate across membranes because their free energy is often lower in the aqueous phase than in the membrane. In simulations, we observed stable transmembrane orientations for all considered helices. It strongly indicates that the investigated peptides derived from colicins are at least kinetically stabilized in the membrane core. Our experimental outcomes also support this finding. Namely, the co-sedimentation assay results prove that the peptide interacts with the lipid membrane, while the leakage assay clearly points to a transmembrane orientation of H1 that causes membrane permeation.

Simulations demonstrate that, while embedded in the membranes, H1s attain tilted transmembrane orientations with the tilt angle toward the membrane plane (between 50 and 70°), similar to other transmembrane peptides [43]. While in the membranes, the peptides showed no significant changes of helicity except for the kink formation. Several kink positions were identified, all located at the hydrophilic charged lysine and arginine residues. In H1 from colicin A and U, the kink also occurred at the isoleucine residue. All observed kinks were stable along the calculated MD trajectories leading to the formation of stable short helical sub-segment in the peptides. The exception was the colicin U in the POPG membrane, where increased flexibility of almost the whole peptide was observed.

While the structure of the considered H1 peptides was mainly unchanged in the membranes, the simulations showed significant alterations of membrane properties. The incorporation of the transmembrane peptides led to the formation of membrane defects in the form of water clusters in the vicinity of the peptide C-terminal. These defects were facilitated by water molecules penetrating the membranes in the headgroup region. Somewhat less pronounced water defects were also observed at the N-terminal side. The presence of the water clusters in the headgroup region also resulted in elevated hydration of the hydrophobic membrane core. Namely, we observed penetration of individual water molecules into the acyl chain area of the membranes. Importantly, in all studied systems, the water molecules were diffusing into the membrane in the vicinity of the transmembrane helices. While these were usually individual water molecules, in two cases, H1 peptides of colicin Ia and U in the POPG membrane, the number of water molecules was significantly increased, and the formation of a stable transmembrane water pore along the peptide surface was observed. The pore formation resulted in membrane permeation by water.

Water penetration into the membrane in the vicinity of H1s can be rationalized by an amphipathic character of these helical peptides, with one hydrophilic and one hydrophobic face. Accordingly, water penetration was primarily observed at the hydrophilic side of each helix. We also observed that the elevated hydration of the membrane core resulted in further membrane restructuring via local bending of lipid headgroups. In the two cases where the water pore was formed, the neighboring lipids were reoriented such that a toroidal pore was formed.

Simulations show that the increased membrane hydration and the observed pore formation are caused by hydrophilic lysine and arginine residues in the parts of the helices located in the membrane core. These charged amino acids, found similarly in the sequence of each of the considered H1s, facilitate water penetration into the membrane core. Such an effect of arginine and lysin was widely reported in the [44–46]. For several synthetic peptides and peptide analogs, it was demonstrated via MD simulations and experiments that the high energetic cost of the presence of the charged residues in the hydrophobic membrane core can be decreased with hydration of the cationic side chains. In the case of lysine, the local penetration of water into the membrane can also be accompanied by the so-called snorkeling effect, where the cationic residue locally pulls the transmembrane peptide toward the more hydrated headgroup region of the membrane. Our results agree with these findings, as the water defects observed here resemble a previously described lysine snorkeling effect [43]. Our simulations demonstrate that water penetration may lead to different outcomes depending on the identity of the lipid headgroups. Namely, while both zwitterionic and negatively charged membranes are penetrated by water, the toroidal pore was effectively formed only in the negatively charged POPG membrane.

At the macroscopic level, we experimentally investigated the influence of the H1 peptide of colicin U on DOPG vesicles that partially mimic the negatively charged bacterial membranes. First, we observed lysis of the large unilamellar vesicles in the presence of the peptide,

demonstrating that H1 is able to disrupt the model membrane. This agrees with simulations showing that H1 of colicin U leads to a reorganization and partial disintegration of negatively charged phospholipid membranes. Almost no cooperativity was observed in the vesicle lysis, as can be concluded from concentration-dependence measurements. It suggests that the membrane disruption is caused by small complexes or even monomers of H1. This finding corroborates with the simulations that showed that even a monomeric H1 can cause water permeation and, in some cases, water pore formation. Regarding the size of the formed pores, we expect that it does not exceed the size of the pores formed by the whole colicin U, which were shown to have the diameter lower than 1 nm [39].

An approach of detecting the cooperativity of a peptide using leakage assay proves very informative. For example, δ-lysin from *Staphylococcus aureus* causes a sigmoidal dependency of calcein leakage rate on toxin concentration, indicating high cooperativity of the peptide pore-formation [47]. Similarly, pores of an artificially designed amphipathic peptide GALA were studied using leakage assay, and their detected cooperativity suggested that GALA pores consist of about ten monomers [48,49]. For the H1 peptide, we operated in peptide/lipid (P/L) molar ratio from 1/200 to 1/20 (when taking into account a binding efficiency of H1, see the next paragraph for the calculation). Within this range of the concentrations, we detected very weak cooperativity ($n = 1.24 \pm 0.058$). Such weak cooperativity at even the highest peptide concentrations (P/L ratio 1/20) could lead us to an assumption that H1 peptide form pores as monomers, maybe occasionally accompanied by forming of small oligomeric structures. Such behavior in membrane differs from magainin 2, which forms oligomeric toroidal pores at specific conditions [50,51]. But it is known that the cooperativity of the peptides varies significantly with experimental conditions used, such as a lipid composition [50]. Therefore, different behavior of the H1 peptide could be possibly observed under varying experimental conditions. The observed binding efficiency of H1 to the vesicles using a co-sedimentation assay was relatively low at about 2.5%. For melittin, which we used as a positive control, we detected 94% binding efficiency. It proves that the H1 peptide is ineffective in binding to the membrane by itself, but once in the membrane, it is successful in the membrane permeation. Like melittin, the amphipathic peptide magainin 2 shows a very high binding efficiency of ~97% to POPC/POPG (1/1) liposomes [52]. At such high binding efficiency, the effective amount of peptide in the membrane is virtually equal to the added quantum.

On the other hand, the effective concentration of the H1 peptide bound to the membrane is many times lower than the one added to the assay. If we suppose that only 2.5% of the H1 peptide binds to the membrane, it corresponds to the effective concentration of bound peptide 1.25–0.125 μM for used concentrations 50–5 μM (subsequently corresponding to the calculated P/L effective molar ratio 1/20–1/200). Using such calculations, we can compare H1s activity with other peptides exerting higher membrane binding efficiency. For example, magainin 2 shows more than 80% leakage of LUVs (at 1/25 P/L molar ratio) with ~97% binding efficiency [52], and melittin shows about 50% leakage of liposomes at 1/40 P/L molar ratio [53]. At similar conditions, the H1 peptide of colicin U caused ~17% leakage after 5 min (at 1/20 calculated effective P/L ratio). In conclusion, when the low binding efficiency is taken into account, the leakage induced by the H1 peptide is considerably high.

Interestingly, the fast initial non-cooperative phase of the liposome leakage followed by very slow dye efflux may suggest that individual H1 peptides that caused vesicle disruption virtually could not dissociate from the membrane and act on the remaining unaffected vesicles. Such a mechanism implies the almost irreversible insertion of those H1 molecules that were bound to the vesicle membrane, which could resemble the behavior of melittin on DOPG liposomes [53].

The relatively low efficiency of spontaneous binding of separated H1 from colicin U to the membranes may be easily consistent with its role in the structure of whole colicin protein. Colicin U, similarly to other pore-forming colicins, interacts with a specific outer membrane receptor which ensures the effective binding to the bacterial surface [9]. After translocation of the CTD across the periplasm, the H1 containing the long helix of the central domain is presumably forced to interact with the plasmatic membrane [14]. As was stated previously, during a channel opening, the helices of related colicin A and Ia are reorganized, and a segment of a few helices (H2–H5) is translocated into the cytoplasm [14], and H1s are probably forced to be in transmembrane orientation. Our simulations clearly prove that H1 helices of colicin A, Ia, and U can remain stable in transmembrane orientation and maintain most of their helical structure. Therefore, it supports our hypothesis that H1 remains in transmembrane orientation when the colicin U channel is opened. Consequently, we cannot rule out a possibility that H1 plays a role in the channel formation by intact colicin U. Even though some studies show that the H1 helix of colicin A is not vital for the formation of the open channel, the authors themselves suggest the possibility that H1 still can have at least a peripheral role, and in case of their deleted versions of CTDs, the role of H1 can be substituted by other amphipathic helices [54,55]. Our simulations show that solitary H1 helix of colicin U and colicin Ia in contrast to colicin A form pores with a toroidal pore-like structure. And some studies on colicin E1 (closely related to colicin Ia) suggest that colicin pores are toroidal [56,57]. Taking it all together, we hypothesize that H1 (of colicin U and Ia) participates directly in the channel formation, which could presumably adopt a toroidal structure.

5. Conclusions

MD simulations and experiments were conducted to unravel how helical peptides derived from H1 helices of colicins U, A, and Ia interact with model membranes. MD simulations demonstrated that the investigated helical peptides could at least transiently incorporate into and influence model zwitterionic and negatively charged lipid membranes. They attain a transmembrane orientation with a moderate tilt. The helical character of the peptides in the membranes is mostly preserved, with the exception of kink formation. While in the membranes, the presence of charged polar residues along the helices causes water clusters formation in the lipid headgroup region of the membrane and subsequent penetration of water molecules into the hydrophobic membrane core. Furthermore, the formation of a toroidal pore was observed in the case of the negatively charged POPG lipid membrane containing H1 of colicin U and H1 of colicin Ia. The simulations are corroborated by experimental measurements performed for the H1 peptide of colicin U in negatively charged DOPG vesicles. The vesicle leakage measurements show that the peptide incorporates into the lipid membrane, causing membrane disruption. Notably, this effect is not cooperative, suggesting that even monomers of H1 are able to permeabilize the membrane. It is important to note that the membrane lysis and pore formation induced by the native colicin proteins may differ from those studied here, the single H1 peptides taken out from the whole protein structures. Nevertheless, the data obtained here for model systems are relevant for understanding the initial action of native colicins in the target plasmatic membrane. Furthermore, our observations can be useful for future exploration of small bio-inspired peptides able to disrupt bacterial membranes.

Declaration of competing interest

The authors declare that they have no known competing financial interests or personal relationships that could have appeared to influence the work reported in this paper.

Acknowledgments

L.C. acknowledges the support of the Czech Science Foundation (grant number 18-26751S). T.D. acknowledges the support of the Charles University Grant Agency (project SVV-260568).

Appendix A. Supplementary data

A detailed analysis of MD simulations for the considered helices in different lipid membranes (distance from the membrane midplane, tilt angle, RMSD, secondary structure, helicity, contacts with water, and lipids). Supplementary data to this article can be found online at https://doi.org/10.1016/j.bbamem.2022.183866.

References

[1] G.H. Cassell, J. Mekalanos, Development of antimicrobial agents in the era of new and reemerging infectious diseases and increasing antibiotic resistance, JAMA 285 (5) (2001) 601–605.
[2] A. Simons, K. Alhanout, R.E. Duval, Bacteriocins, antimicrobial peptides from bacterial origin: overview of their biology and their impact against multidrug-resistant bacteria, Microorganisms 8 (5) (2020) 639.
[3] E. Cascales, et al., Colicin biology, Microbiol. Mol. Biol. Rev. 71 (1) (2007) 158–229.
[4] J. Šmarda, D. Šmajs, Colicins—Exocellular lethal proteins ofEscherichia coli, Folia Microbiol. 43 (6) (1998) 563–582.
[5] X. Jin, et al., Rapid production and characterization of antimicrobial colicins using Escherichia coli-based cell-free protein synthesis, Synth. Biol. 3 (1) (2018) p. ysy004.
[6] S. Murinda, K. Rashid, R.F. Roberts, In vitro assessment of the cytotoxicity of nisin, pediocin, and selected colicins on simian virus 40–transfected human colon and vero monkey kidney cells with trypan blue staining viability assays, J. Food Prot. 66 (5) (2003) 847–853.
[7] R.A. Fisher, B. Gollan, S. Helaine, Persistent bacterial infections and persister cells, Nat. Rev. Microbiol. 15 (8) (2017) 453.
[8] T. Arnold, K. Zeth, D. Linke, Structure and function of colicin S4, a colicin with a duplicated receptor-binding domain, J. Biol. Chem. 284 (10) (2009) 6403–6413.
[9] D. Smajs, H. Pilsl, V. Braun, Colicin U, a novel colicin produced by shigella boydii, J. Bacteriol. 179 (15) (1997) 4919–4928.
[10] K.L. Kotloff, et al., Shigellosis, Lancet 391 (10122) (2018) 801–812.
[11] M.W. Parker, et al., Refined structure of the pore-forming domain of colicin A at 2.4 Å resolution, J. Mol. Biol. 224 (3) (1992) 639–657.
[12] M. Wiener, et al., Crystal structure of colicin Ia, Nature 385 (6615) (1997) 461–464.
[13] M.R. Lugo, D. Ho, A.R. Merrill, Resolving the 3D spatial orientation of helix I in the closed state of the colicin E1 channel domain by FRET. Insights into the integration mechanism, Arch. Biochem. Biophys. 608 (2016) 52–73.
[14] S. Slatin, et al., Gating movements of colicin a and colicin Ia are different, J. Membr. Biol. 202 (2) (2004) 73–83.
[15] D. Duché, et al., Membrane topology of the colicin A pore-forming domain analyzed by disulfide bond engineering, J. Biol. Chem. 271 (26) (1996) 15401–15406.
[16] P.K. Kienker, K.S. Jakes, A. Finkelstein, Protein translocation across planar bilayers by the colicin Ia channel-forming domain: where will it end? J. Gen. Physiol. 116 (4) (2000) 587–598.
[17] J. Yang, et al., The I-TASSER suite: protein structure and function prediction, Nat. Methods 12 (1) (2015) 7–8.
[18] F. Sievers, et al., Fast, scalable generation of high-quality protein multiple sequence alignments using clustal omega, Mol. Syst. Biol. 7 (1) (2011) 539.
[19] A. Melcrova, et al., Surface roughness and palmitoylation of transmembrane helices influence membrane structure and dynamics, Biophys. J. 116 (3) (2019), 89A-89A.
[20] K. Lindorff-Larsen, et al., Improved side-chain torsion potentials for the Amber ff99SB protein force field, Proteins 78 (8) (2010) 1950–1958.
[21] J.P. Jambeck, A.P. Lyubartsev, Derivation and systematic validation of a refined all-atom force field for phosphatidylcholine lipids, J. Phys. Chem. B 116 (10) (2012) 3164–3179.
[22] J.P.M. Jämbeck, A.P. Lyubartsev, An extension and further validation of an all-atomistic force field for biological membranes, J. Chem. Theory Comput. 8 (8) (2012) 2938–2948.
[23] F. Chen, P.E. Smith, Simulated surface tensions of common water models, J. Chem. Phys. 126 (22) (2007).
[24] L.X. Dang, Molecular Simulation Analysis and X-ray Absorption Measurement of Ca2+, K+ and Cl-ions in Solution, ACS Publications, 2006.
[25] M. Javanainen, Universal method for embedding proteins into complex lipid bilayers for molecular dynamics simulations, J. Chem. Theory Comput. 10 (6) (2014) 2577–2582.
[26] M.J. Abraham, et al., GROMACS: high performance molecular simulations through multi-level parallelism from laptops to supercomputers, SoftwareX 1 (2015) 19–25.
[27] S. Nose, A molecular dynamics method for simulations in the canonical ensemble, Mol. Phys. 52 (1984) 255–268.
[28] G. Bussi, D. Donadio, M. Parrinello, Canonical sampling through velocity rescaling, J. Chem. Phys. 126 (1) (2007), 014101.
[29] B. Hess, et al., LINCS: a linear constraint solver for molecular simulations, J. Comput. Chem. 18 (12) (1997) 1463–1472.
[30] R. Hockney, S. Goel, J. Eastwood, Quiet high-resolution computer models of a plasma, J. Comput. Phys. 14 (1974) 148–158.
[31] U. Essmann, et al., A smooth particle mesh ewald method, J. Chem. Phys. 103 (19) (1995) 8577–8593.
[32] J. Hunter, matplotlib: matplotlib v1.5.1, 2016 (url).
[33] L. Schrodinger, The PyMOL Molecular Graphics System, Version 1.8, Schrodinger, LLC, 2015.
[34] W. Humphrey, A. Dalke, K. Schulten, VMD: visual molecular dynamics, J. Mol. Graph. 14 (1) (1996) 33–38.
[35] P. Rice, I. Longden, A. Bleasby, EMBOSS: the european molecular biology open software suite, Trends Genet. 16 (6) (2000) 276–277.
[36] E. Gasteiger, Protein identification and analysis tools on the ExPASy server, in: The Proteomics Protocols Handbook, 2005, pp. 571–607.
[37] R.C. MacDonald, et al., Small-volume extrusion apparatus for preparation of large, unilamellar vesicles, Biochim. Biophys. Acta Biomembr. 1061 (2) (1991) 297–303.
[38] G. Rouser, S. Fleischer, A. Yamamoto, Two dimensional thin layer chromatographic separation of polar lipids and determination of phospholipids by phosphorus analysis of spots, Lipids 5 (5) (1970) 494–496.
[39] T. Dolejšová, et al., Colicin U from shigella boydii forms voltage-dependent pores, J. Bacteriol. 201 (24) (2019).
[40] S.D. Zakharov, W.A. Cramer, Colicin crystal structures: pathways and mechanisms for colicin insertion into membranes, Biochem. Biophys. Res. Commun. 1565 (2) (2002) 333–346.
[41] I. Kabelka, R. Vácha, Optimal hydrophobicity and reorientation of amphiphilic peptides translocating through membrane, Biophys. J. 115 (6) (2018) 1045–1054.
[42] L. Bartoš, I. Kabelka, R. Vácha, Enhanced translocation of amphiphilic peptides across membranes by transmembrane proteins, Biophys. J. 120 (11) (2021) 2296–2305.
[43] M. Jafari, F. Mehrnejad, F. Doustdar, Insight into the interactions, residue snorkeling, and membrane disordering potency of a single antimicrobial peptide into different lipid bilayers, PLoS One 12 (11) (2017), e0187216.
[44] L. Li, I. Vorobyov, T.W. Allen, The different interactions of lysine and arginine side chains with lipid membranes, J. Phys. Chem. B 117 (40) (2013) 11906–11920.
[45] E. Strandberg, J.A. Killian, Snorkeling of lysine side chains in transmembrane helices: how easy can it get? FEBS Lett. 544 (1–3) (2003) 69–73.
[46] N.J. Gleason, et al., Buried lysine, but not arginine, titrates and alters transmembrane helix tilt, Proc. Natl. Acad. Sci. U. S. A. 110 (5) (2013) 1692–1695.
[47] G. Menestrina, Escherichia coli hemolysin permeabilizes small unilamellar vesicles loaded with calcein by a single-hit mechanism, FEBS Lett. 232 (1) (1988) 217–220.
[48] W. Li, F. Nicol, F.C. Szoka Jr., GALA: a designed synthetic pH-responsive amphipathic peptide with applications in drug and gene delivery, Adv. Drug Deliv. Rev. 56 (7) (2004) 967–985.
[49] R.A. Parente, S. Nir, F.C. Szoka Jr., Mechanism of leakage of phospholipid vesicle contents induced by the peptide GALA, Biochemistry 29 (37) (1990) 8720–8728.
[50] K. Matsuzaki, et al., Orientational and aggregational states of magainin 2 in phospholipid bilayers, Biochemistry 33 (11) (1994) 3342–3349.
[51] S.J. Ludtke, et al., Membrane pores induced by magainin, Biochemistry 35 (43) (1996) 13723–13728.
[52] S.M. Gregory, A. Pokorny, P.F. Almeida, Magainin 2 revisited: a test of the quantitative model for the all-or-none permeabilization of phospholipid vesicles, Biophys. J. 96 (1) (2009) 116–131.
[53] G. Van Den Bogaart, et al., On the mechanism of pore formation by melittin, J. Biol. Chem. 283 (49) (2008) 33854–33857.
[54] A. Nardi, et al., The C-terminal half of the colicin A pore-forming domain is active in vivo and in vitro, J. Mol. Biol. 307 (5) (2001) 1293–1303.
[55] D. Baty, et al., A 136-amino-acid-residue COOH-terminal fragment of colicin A is endowed with ionophoric activity, Eur. J. Biochem. 189 (2) (1990) 409–413.
[56] A.A. Sobko, et al., Effect of lipids with different spontaneous curvature on the channel activity of colicin E1: evidence in favor of a toroidal pore, FEBS Lett. 576 (1–2) (2004) 205–210.
[57] A.A. Sobko, et al., Lipid dependence of the channel properties of a colicin E1-lipid toroidal pore, J. Biol. Chem. 281 (20) (2006) 14408–14416.

7 Supporting information of Publication IV

Supporting Information

H1 helix of colicin U causes phospholipid membrane permeation

Kamila Riedlová,[1, 2] Tereza Dolejšová,[3,1] Radovan Fišer,[3*] and Lukasz Cwiklik[1*]

[1]J. Heyrovský Institute of Physical Chemistry, Czech Academy of Sciences, Dolejškova 3, 18223 Prague, Czech Republic

[2]Department of Physical and Macromolecular Chemistry, Faculty of Science, Charles University, Hlavova 8, 12800, Prague, Czech Republic

[3]Department of Genetics and Microbiology, Faculty of Science, Charles University, Viničná 5, 12843, Prague, Czech Republic

Table S1. The grand average of hydropathicity index (GRAVY) calculated for the three considered H1 peptides, compared with four other peptides. The index quantifies hydrophobicity based on the sum of the hydropathy values of the amino acids divided by the sequence length. Positive GRAVY indicates a hydrophobic character while negative values point to a hydrophilic properties. GRAVY was calculated using the ExPASy online server.

Peptide	GRAVY
H1 of colicin A	-0.641
H1 of colicin Ia	-0.885
H1 of colicin U	-0.030
Melittin	0.273
Pardaxin P-4	0.745
Ile_{21}	4.500
Lys_{21}	-3.900
Buforin II	-0.638
Magainin 2	0.083

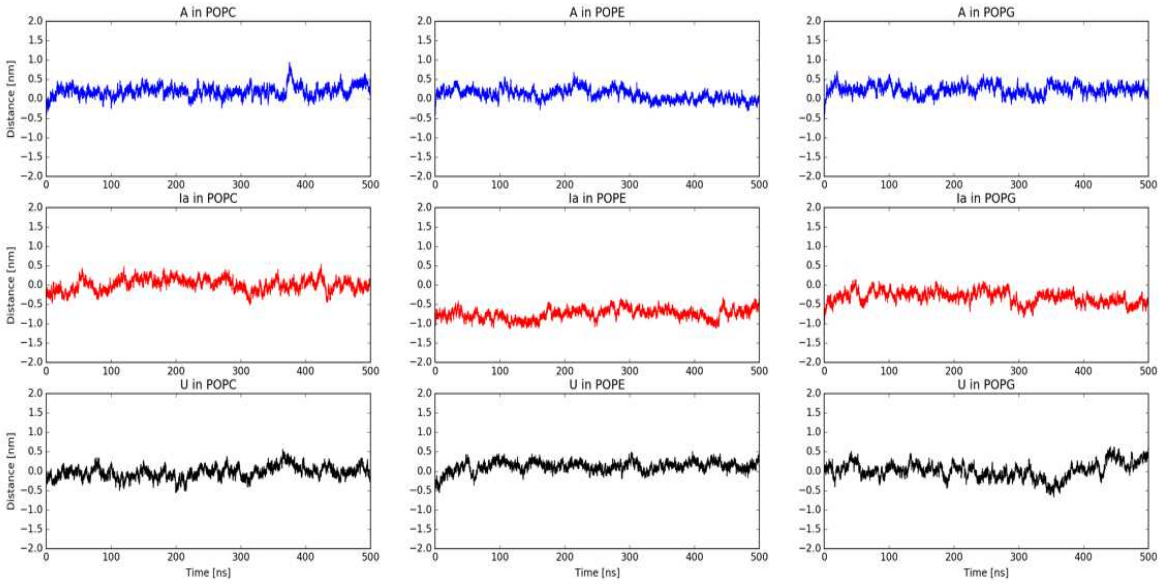

Fig. S1. Distance of H1 helices from the lipid membrane midplane.

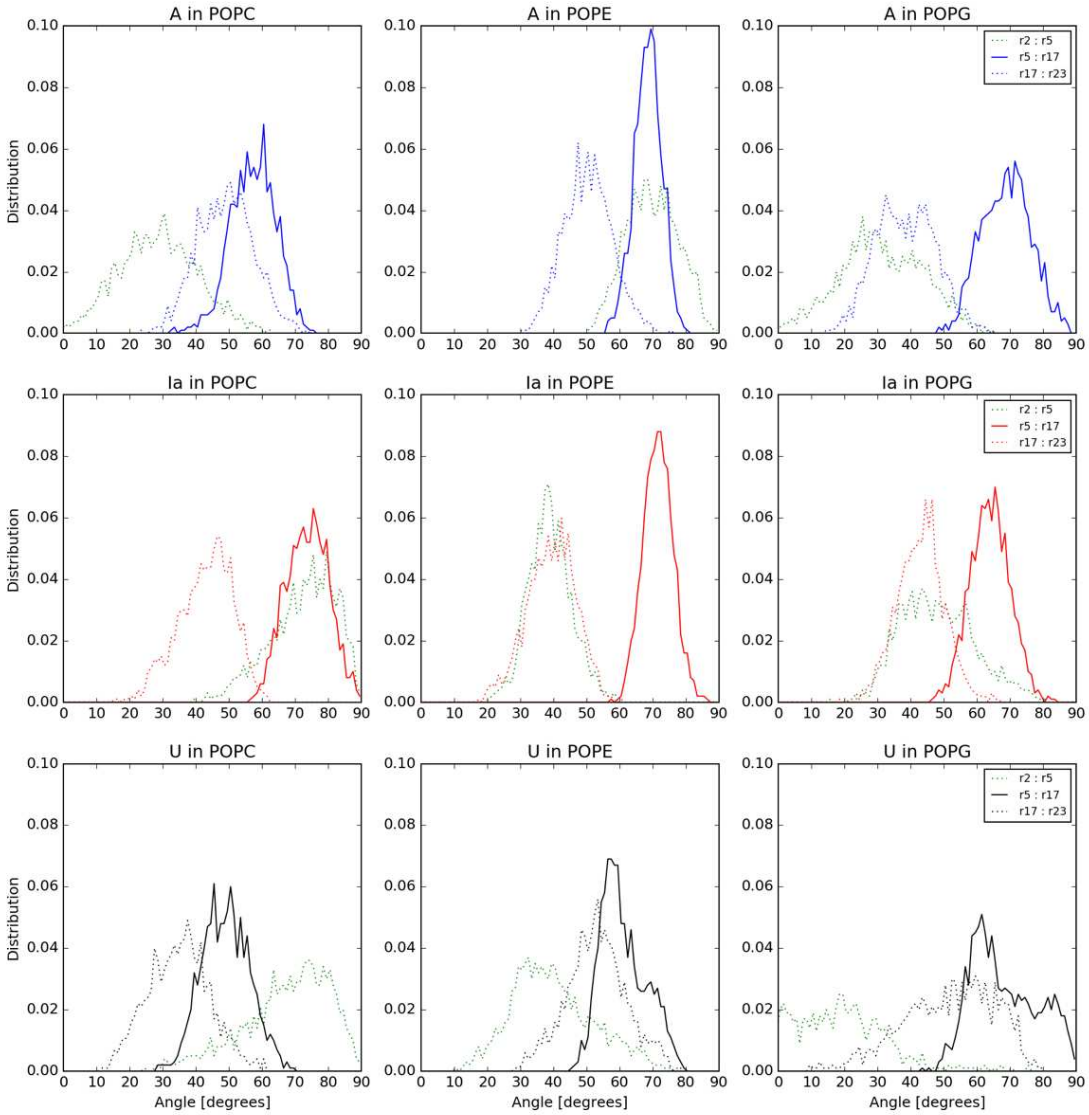

Fig. S2. Tilt angles of the considered H1 colicin helices embedded in different lipid membranes. In each case, the tilt angle of the main middle segment of the peptide (from residues 5 to 17, shown with the solid line) as well as of for the two shorter flanking segments (dotted lines), chosen based on the peptide kink, are presented. The tilt angle of 0 degrees corresponds to a parallel, and 90 degrees corresponds to a perpendicular orientation with respect to the membrane. The distribution was not normalized by means of conditional probability.

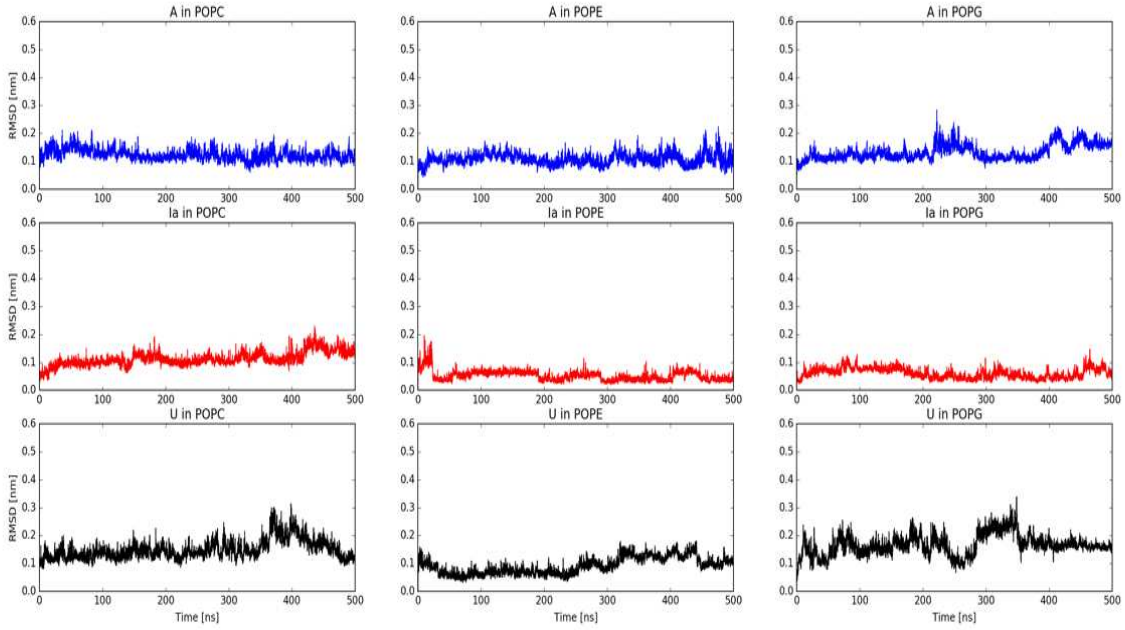

Fig. S3. RMSD of H1 helices in lipid membranes.

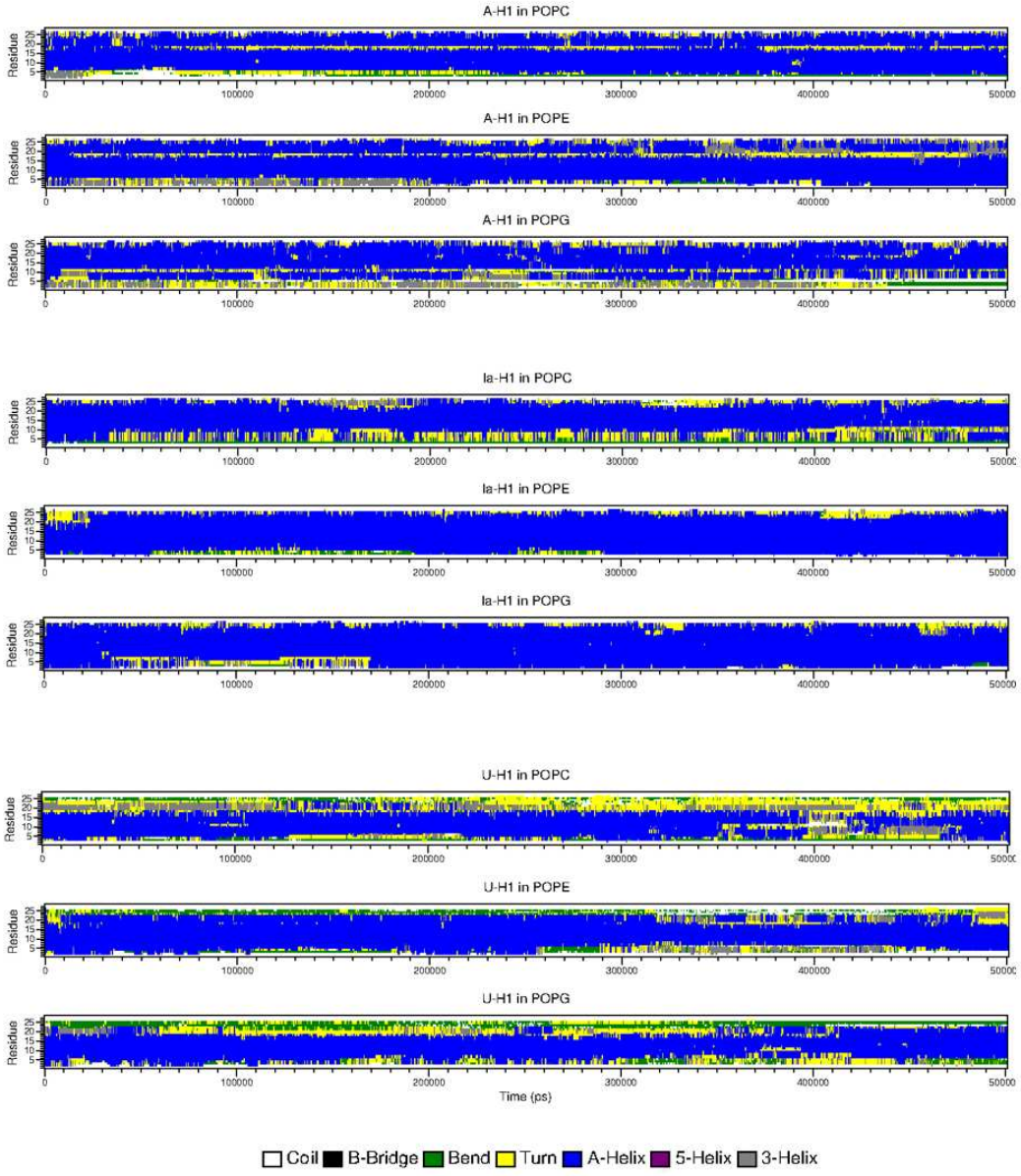

Fig. S4. Secondary structure of H1 helices (obtained using DSSP method implemented in the Gromacs tools).

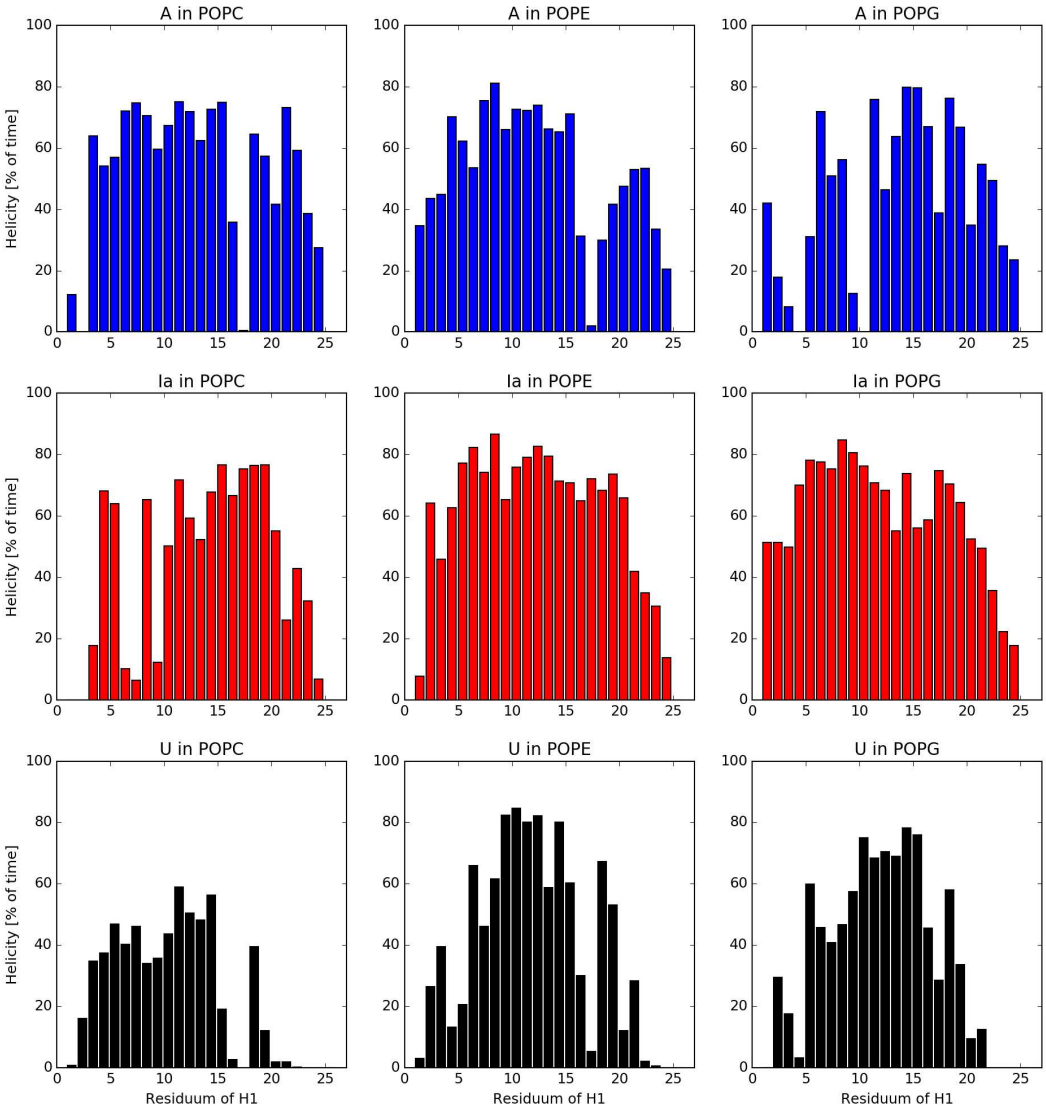

Fig. S5. Helicity of H1 helices of the considered colicins.

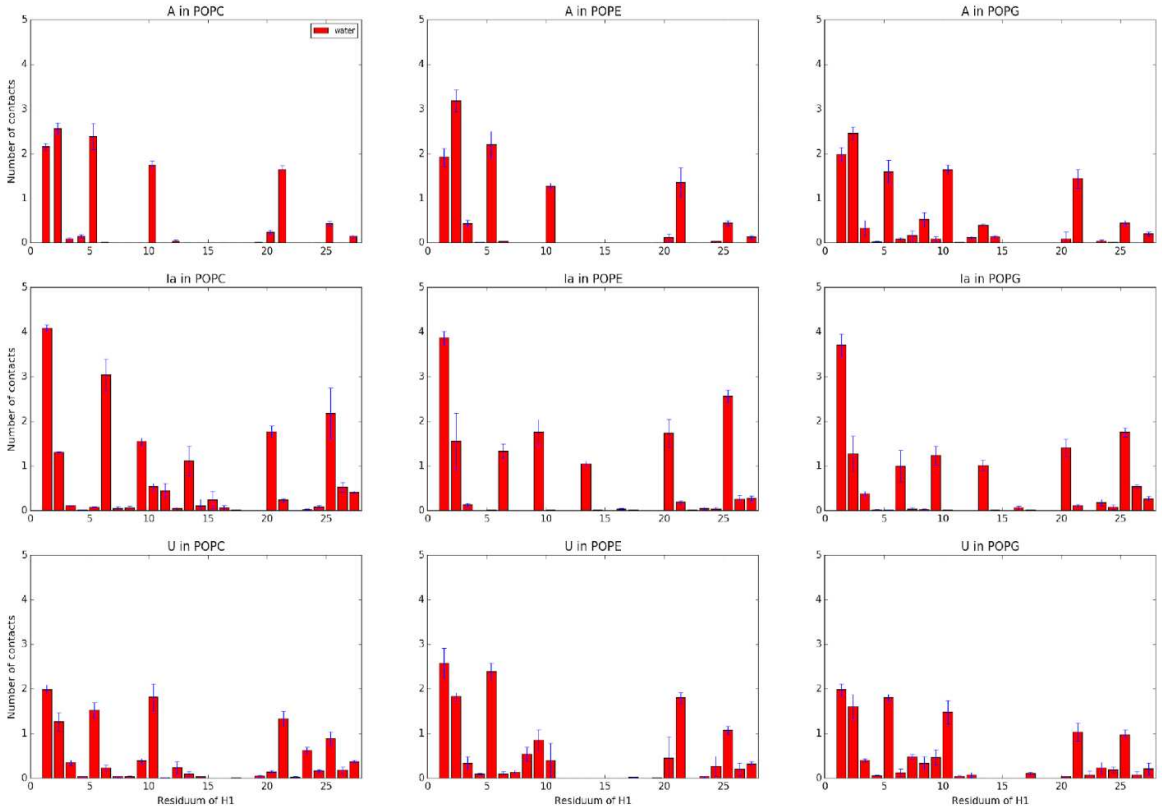

Fig. S6. Contacts with water for the considered helices.

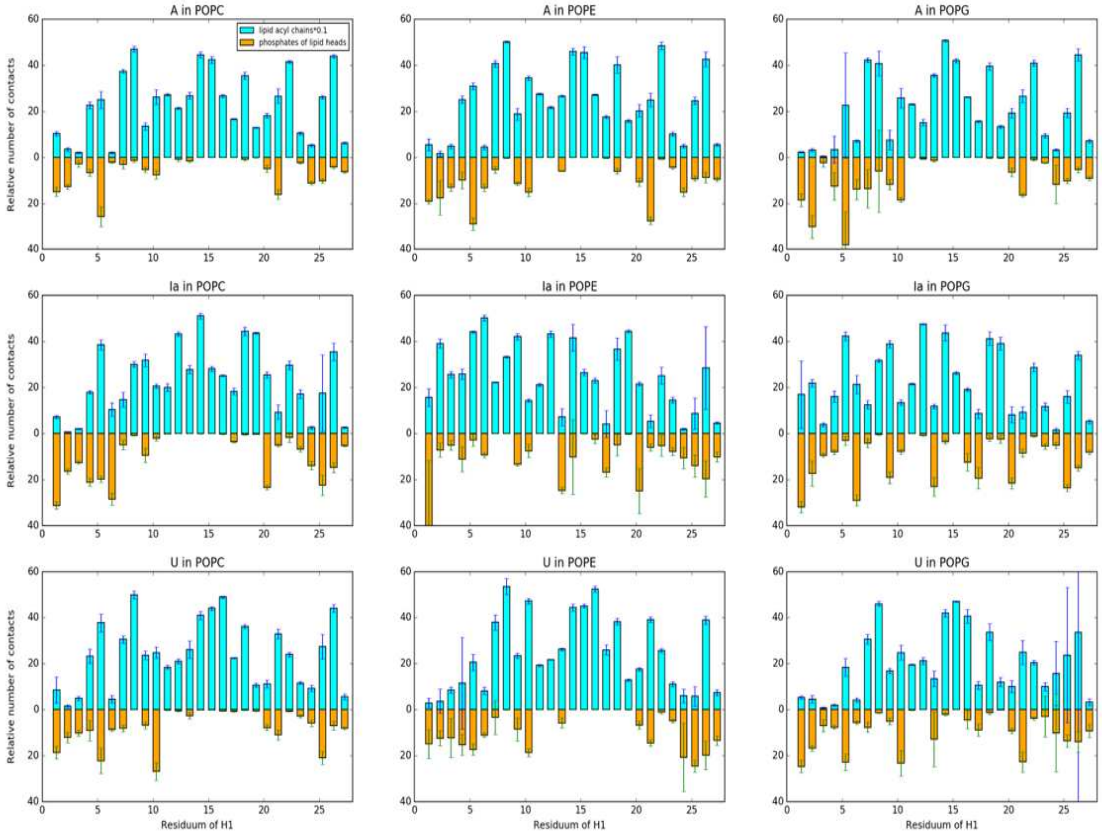

Fig. S7. Contacts with lipid headgroups and tails for the considered helices.